

AD-A179 436 RELIABILITY STUDIES OF CERAMIC CAPACITORS(U) MISSOURI
UNIV-ROLLA H U ANDERSON MAR 87 N00014-82-K-0294

AD-A179 436 RELIABILITY STUDIES OF CERAMIC CAPACITORS(U) MISSOURI
UNIV-ROLLA H U ANDERSON MAR 87 N00014-82-K-0294

1/2

UNCLASSIFIED

F/G 9/1

ML.

AD-A179 436

DTIC FILE COPY

2

RELIABILITY STUDIES OF CERAMIC CAPACITORS

Progress Report
for period of
October 1, 1984 - December 31, 1986

H. U. Anderson
University of Missouri-Rolla

March 1987

Prepared for the
Office of Naval Research
Contract No. N00014-82-K-0294

DTIC
ELECTE
APR 22 1987
S D

DISTRIBUTION STATEMENT A

Approved for public release
Distribution Unlimited

87 4 21 180

DISCLAIMER NOTICE

**THIS DOCUMENT IS BEST QUALITY
PRACTICABLE. THE COPY FURNISHED
TO DTIC CONTAINED A SIGNIFICANT
NUMBER OF PAGES WHICH DO NOT
REPRODUCE LEGIBLY.**

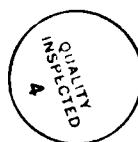
ADA 179436

REPORT DOCUMENTATION PAGE

1a REPORT SECURITY CLASSIFICATION Unclassified			1b RESTRICTIVE MARKINGS		
2a SECURITY CLASSIFICATION AUTHORITY			1 DISTRIBUTION/AVAILABILITY OF REPORT Approved for Public Release Distribution Unlimited		
2b DECLASSIFICATION/DOWNGRADING SCHEDULE					
4 PERFORMING ORGANIZATION REPORT NUMBER(S)			5 MONITORING ORGANIZATION REPORT NUMBER(S)		
6a NAME OF PERFORMING ORGANIZATION Department of Ceramic Engr. University of Missouri-Rolla		6b OFFICE SYMBOL (If applicable)	7a NAME OF MONITORING ORGANIZATION		
6c ADDRESS (City, State and ZIP Code) 120 Fulton Hall Rolla, MO 65401			7b ADDRESS (City, State and ZIP Code)		
8a NAME OF FUNDING/SPONSORING ORGANIZATION Office of Naval Research		8b OFFICE SYMBOL (If applicable)	9. PROCUREMENT INSTRUMENT IDENTIFICATION NUMBER N00014-82-K-0294		
8c ADDRESS (City, State and ZIP Code) Division of Materials Research Arlington, VA 22217			10. SOURCE OF FUNDING NOS.		
11 TITLE (Include Security Classification) Reliability Studies of Ceramic Capacitors			PROGRAM ELEMENT NO.	PROJECT NO.	TASK NO.
			WORK UNIT NO.		
12. PERSONAL AUTHOR(S) H. U. Anderson					
13a. TYPE OF REPORT Annual		13b. TIME COVERED FROM 10/01/84 to 12/31/86		14 DATE OF REPORT (Yr., Mo., Day) March 1987	
				15. PAGE COUNT 155	
16. SUPPLEMENTARY NOTATION					
17 COSATI CODES			18 SUBJECT TERMS (Continue on reverse if necessary and identify by block number)		
FIELD	GROUP	SUB GR	→ Degradation, Heat Conductivity, Effects of Humidity, Relaxors		
19 ABSTRACT (Continue on reverse if necessary and identify by block number) Barium Titanate This report covers the last year of a contract which studied low voltage degradation, the TSPC/DC spectra of BaTiO₃ , and the dielectric and electrical properties of BaTiO₃ composites (polymer and air) and the first one and one half years of a project which focussed on 1) measurements on commercially available relaxor type dielectrics, and 2) organometallic processed relaxor dielectrics synthesis, fabrication and measurement. The measurements to be made are electrical conductivity, dielectric properties, and current-time voltage behavior as a function of chemical composition, temperature, and humidity. Key words:					
20 DISTRIBUTION/AVAILABILITY OF ABSTRACT UNCLASSIFIED UNLIMITED <input type="checkbox"/> SAME AS RPT <input type="checkbox"/> DTIC USERS <input type="checkbox"/>			21 ABSTRACT SECURITY CLASSIFICATION		
22a NAME OF RESPONSIBLE INDIVIDUAL			22b TELEPHONE NUMBER (Include Area Code)		22c OFFICE SYMBOL

Contents

	Page
Recent Results and Accomplishments.	4
Status of Individual Projects	12
TSPC/DC Measurements	12
Dielectric Composites.	12
Low Voltage Degradation Studies.	13
Relaxor Degradation Studies.	13
Relaxor Preparation.	13
Resulting Publications.	14
Papers in Preparation	15
Appendices:	
A. Thermally-Stimulated Current and Dielectric Properties of Doped and Undoped Barium Titanate, Ph.D. Thesis, W. Huebner. A1	
B. TSPC/DC Measurements on Barium Titanate.	B1
C. Dielectric and Electrical Properties of BaTiO ₃ Composites. .	C1
D. An Investigation of the Low Voltage Failure Mechanism in Multilayer Ceramic Capacitors.	D1
E. Contribution to the Electrical and Mechanical Phase Diagram of La-Doped Lead Zirconate Titanate.	E1
F. Polymeric Synthesis of Lead Magnesium Niobate Dielectrics. .	F1
G. Reactions in the System PbO-MgO-Nb ₂ O ₅	G1
H. Preparation of Perovskite Pb(Mg _{1/3} Nb _{2/3})O ₃ Using Pb ₃ Nb ₂ O ₈ and MgO.	H1



Distribution/	
Availability Codes	
Dist	Avail and/or Special
A-1	23

Contents (cont.)

	Page
I. Microstructural Inhomogeneity in Sintered Pb(Mg _{1/3} Nb _{2/3})O ₃ -PbTiO ₃ Based Dielectrics.	I1
J. Effects of Additions on the Physical and Dielectric Properties of Lead Magnesium Niobate	J1
K. The Effect of Excess Lead Oxide on the Sintering Characteristics and Dielectric Properties of Lead Magnesium Niobate Ceramics	K1

Abstract

This report covers the last year of a contract which studied low voltage degradation, the TSPC/DC spectra of BaTiO_3 , and the dielectric and electrical properties of BaTiO_3 composites (polymer and air) and the first one and one half years of a project which focussed on 1) measurements on commercially available relaxor type dielectrics, and 2) organometallic processed relaxor dielectrics synthesis, fabrication and measurement. The measurements to be made are electrical conductivity, dielectric properties, and current-time voltage behavior as a function of chemical composition, temperature, and humidity.

Recent Results and Achievements

Our program has progressed to the point where a number of our initial goals have been achieved. The most significant accomplishments are described below.

High Voltage Degradation of High Purity BaTiO_3

1. The stoichiometric composition exhibits the lowest current levels in all fields and at all firing temperatures. This leads one to suspect that the second phase, present from the excess barium titanate, contributes to the degradation.
2. Compositions with barium/titanium ratios of greater than one exhibit higher current levels and enhanced degradation compared to the excess titanium compositions. This is contrary to some of our previous results but is probably due to the hydration of the Ba_2TiO_4 phase, which is present, because barium is essentially insoluble in BaTiO_3 .

3. Compositions with barium/titanium ratios less than one exhibit higher current levels and enhanced degradation compared to the stoichiometric composition.
4. Decreasing the density or increasing the porosity results in lower current levels and improved degradation resistance. The specimens with the highest porosities are the best. These do not degrade even with fields as high as 20 kV/cm at which breakdown occurs. From these results, we conclude that surface conduction with the presence of water leads to higher leakage current in porous capacitors, and if water is excluded, no increases in leakage current are observed.
5. Increasing the applied field increases the initial degradation rate. In many instances, a shift from ohmic to nonlinear voltage dependence is observed as the field is increased.

High Voltage Degradation Studies

1. The current-voltage behavior ranges from ohmic to voltage dependences greater than that predicted by the space charge limited current. There does not appear to be any distinctive power law that depicts current-voltage behavior. The only trend that we have observed is that the capacitors, which are most reliable, are those closest to ohmic behavior.
2. The temperature dependence of stable capacitors yields an activation energy greater than 1 eV, whereas capacitors which degrade, have an activation energy less than 1 eV. In general, as the field increases, the activation energy decreases as the degradation rate increases.
3. In order to obtain reproducible results, capacitors need to be reequilibrated between I-time runs, particularly those that degrade. We found that equilibration at 1000°C for eight hours is required to achieve reproducibility. If this is not done, when the voltage is increased, the

current starts at about the same level that it finished with the previous measurement. The implication that we get from this result is that life-testing our parts at high voltages to qualify them may start them on the road to failure. Perhaps, we should try to make the MLC's good enough so that the "burn-in" step can be eliminated. This in turn would eliminate the suspected premature accelerated failure resulting from testing.

Low-Voltage Degradation Studies

1. None of the 1400 encapsulated and 600 chip commercial capacitors tested failed the methanol test. We detected failures in some chip capacitors, which we knew had gross flaws that were in the form of delams and thermally created cracks. We conclude that the methanol test is only sensitive to physical flaws, which allow the methanol to penetrate to an active region of the capacitor. We suspect that this test is not very sensitive and should be used with caution. Perhaps soaking in a salt solution would be a better screening method.
2. None of the 1100 capacitors tested with an 85/85/1.5 VDC developed the classic low voltage shorts, and 3.6% of the capacitors decreased in resistance by two orders of magnitude or greater during the life tests. It was evident that gradual degradation of the dielectrics was occurring during the tests. These capacitors, when subjected to the thermally stimulated current test, behaved as conductors rather than capacitors.
3. MLC's exhibit non-ohmic I-V behavior. The current levels for all of the MLC's were non-ohmic. It appears that this may be related to their high voltage degradation.
4. a) The methanol test is only sensitive to physical flaws which penetrate from the surface to an active region of a capacitor.

b) Low voltage failure was induced into multilayer ceramic capacitors by the introduction of micro-cracks reaching from the surface through the electrode layers by means of thermal shock and then exposing the capacitors to a low voltage bias and a humid atmosphere. Results indicated a simple electrolytic solution mechanism may be the conduction mechanism, and that the proposed dendritic growth mechanisms may be more complex than necessary.

One of the most significant observations was that in the presence of moisture the leakage current followed a "saw tooth" pattern very similar to that observed for porous BaTiO_3 suggesting that continuous surfaces between anode and cathode are necessary for the appearance of the low voltage failure mechanism.

The cracked capacitors in this study showed the "classical" low voltage failure characteristics, i.e. the presence of structural defects and the tendency to clear under high bias.

In several notable instances, a "sawtooth" pattern of failure was seen to occur. This "sawtooth" pattern is unique to this study, and has a period of approximately 30 minutes.

No excess electrode material was found anywhere in any of the cracks examined.

Any time the moisture was removed from the capacitor, either by manipulation of the atmosphere or by heating the capacitor, failure immediately ceased.

The electrode material, Pd, is practically insoluble in water.

Low voltage did not occur at 0.5 VDC bias, but did occur at 1.0 VDC bias, establishing a failure threshold between these two voltages.

The results indicate that dendritic growth is not the cause of low-voltage failure. The period of the "sawtooth" is 30 minutes, too short

a time for Pd dendrites to grow. Dendritic growth also requires a supersaturation of electrode material in solution and low temperatures, both of which were unavailable conditions. Furthermore, failure ceased to occur immediately after the moisture was removed from the atmosphere. If dendrites were providing conduction paths, removing their growth mechanism shouldn't remove already existing dendrites.

It is much more likely that failure occurred due to an electrolytic conduction mechanism. Any soluble impurity ions present could conceivably contribute to breakdown. Also, water electrolysis at 0.87 VDC, which agrees with our threshold location between 0.5 and 1.0 VDC. At higher voltages the increased currents could generate enough localized heat to evaporate the aqueous conducting medium. This also explains the "sawtooth" effect observed.

TSPC/TSDC Measurements

1. TSPC/DC can distinguish between "good" and "failed" units.
2. TSPC/DC can detect tendencies towards failure and if the unit is already degrading.
3. TSPC/DC can detect variations in chemical composition which lead to nonuniform Curie temperatures. This technique is also sensitive to phase transformations.
4. This technique is an excellent indicator of stoichiometry of BaTiO_3 . This is because the microstructure is very Ba:Ti ratio sensitive, and the TSPC/DC technique is sensitive to lattice strain and domain clamping.
5. Thermally stimulated current measurements by themselves cannot consistently predict failure. This technique does offer information on failure but would not serve as a primary screen.

6. Thermally stimulated current measurements cannot detect internal flaws, such as cracks, delams, and pores. It appears that the polarization mechanisms in the high K materials are so large that the charge absorption and desorption from them masks any charging or discharging activity that a physical flaw might exhibit.

7. Thermally-stimulated polarization/depolarization current (TSPC/DC) measurements were made on high-purity doped and undoped BaTiO_3 as a function of applied field, heating rate, dopant level, and Ba:Ti ratio. The form of the TSPC/DC curves is dependent upon both the resistive and ferroelectric properties of BaTiO_3 . For TSPC spectra, current peaks are exhibited due to the spontaneous polarization with changing crystal structure. In particular, whether the phase transition is first or second order influences the existence and magnitude of the current peaks.

TSDC measurements are essentially dynamic pyroelectric measurements and as such are useful in determining the pyroelectric coefficient and the magnitude of the spontaneous polarization. The TSDC current did not approach zero in the paraelectric region for some of the specimens, indicative of an anomalous polarization present due to the migration of charged oxygen vacancies. This information is useful for analyzing DC electrical degradation.

Variation in the Ba:Ti ratio affects the grain size distribution, and hence, the ease of domain switching. This directly affects the presence and magnitude of current peaks. The Ba:Ti ratio also affects the activation energy of conduction, resistivity, and degradation behavior, all of which are reflected by the magnitude of the TSPC/DC current in the paraelectric region.

BaTiO₃ Composites

In this investigation composites of unconsolidated BaTiO₃ powder (>99.9% purity, <0.1μm crystalline size) or partially-sintered BaTiO₃ with either air or polymer were studied. The purpose of this study was to measure the dielectric and electrical properties of the composites, and to determine how well these properties fit existing theories concerning fine-grained permittivity and dielectric mixing rules.

The microstructures of the composites were characterized by scanning electron microscopy and density measurement. A stress-structure model with both the Niesel-Bruggeman and Bottcher mixing rules is proposed to explain the observed dielectric behavior of the composites in terms of the microstructure. The results showed the enhanced dielectric constants of the composites were obtained by the stress enhancement.

Relaxor Behavior of La-Doped Lead Zirconate Titanate

An extension of the electrical and mechanical phase diagram of La-doped PbZrO₃/PbTiO₃ (PLZT) has been made using samples of 8 at.% La (PLZT-8), 10 at.% La (PLZT-10), and 12 at.% La (PLZT-12). Magnetically driven mechanical resonance curves for thin reed samples were recorded as a function of temperature and La concentration. The resonance curves were analyzed using an empirical expansion to the third order spring constant to accomodate the strongly nonlinear response. The results indicated that the elastic softening anomaly in PLZT-8 fell significantly below the maximum in the dielectric constant, but coincident in temperature with an observed "bump" in the dissipation factor. The elastic anomaly in PLZT-10 and PLZT-12 fell near the maximum in the 100 KHz dielectric constant, and no "bump" was observed in the dissipation factor. The results of thermally

stimulated current measurements showed that under an electric field of 500 V/cm depolarization occurred almost linearly from the poled ferroelectric state to the paraelectric state. The polarization goes abruptly to zero near 410°K for all compositions with the field applied. The field free depolarization curves for all compositions extended beyond 410°K. The endpoint was not observed. (Appendix E)

Preparation of Relaxor Dielectrics

1) Polymeric Synthesis of $\text{Pb}_3\text{MgNb}_2\text{O}_9$

The results show that single phase powders of about 50 nm crystallite size can be prepared at temperatures as low as 500°C. This preparation technique is based upon having the individual cations complexed in separate weak organic acid solutions. The individual solutions are gravimetrically analyzed for the respective cation concentration to a precision of 10-100 ppm. In this way it is possible to precisely control all of the cation concentrations, and to mix the ions on an atomic scale in the liquid state. There is no precipitation in the mixed solution as it is evaporated to the rigid polymeric states in the form of a uniformly colored transparent glass. This glass is calcined to yield powders which are both homogeneous and single phase with well controlled cation stoichiometry. The synthesis process is described in Appendix F and some resulting electrical, microstructural and crystallographic characteristics were obtained for sintered capacitors made with powders derived from this synthesis.

2) Solid State Synthesis of $\text{Pb}_3\text{MgNb}_2\text{O}_9$

The sintering behavior and microstructural development of dielectric ceramics based on $\text{Pb}(\text{Mg}_{1/2}\text{Nb}_{2/3})\text{O}_3$ - PbTiO_3 solid solutions are greatly affected by the formation of a liquid phase at $\approx 1290^\circ\text{C}$. Prolonged sintering at and above this temperature gives rise to an excessive PbO loss

and the resultant variation in composition leads to an inhomogeneous microstructure. The inhomogeneity is characterized by the formation of a dense, localized region containing a PbO-rich liquid near the surface with a porous interior region in the bulk of the sample.

The synthesis of perovskite $\text{Pb}(\text{Mg}_{1/3}\text{Nb}_{2/3})\text{O}_3$ from an equimolar mixture of $\text{Pb}_3\text{Nb}_2\text{O}_8$ and MgO was studied by solid-state reaction techniques. An addition of 1 wt.% excess MgO to the stoichiometric composition enhances the formation of the cubic perovskite phase. The absence of free PbO in the initial starting materials minimizes the volatilization loss during firing, thereby reducing the possibility of any compositional change and resulting in a substantial improvement of the perovskite phase purity over the conventional mixed-oxide processing.

Status of Individual Projects

TSPC/DC Measurements

These measurements were originally undertaken to see if this technique could yield information on the degradation process in ceramic capacitors. The results have shown that the polarization mechanisms in the high K materials are so large that any contribution that degradation can make is not detectable. Therefore, these measurements have been suspended.

(Appendices A and B)

Dielectric Composite Studies

These studies were undertaken in order to evaluate the relationship of porosity to dielectric properties. These studies were completed in early 1986 so no further work is being done. (Appendix C)

Low Voltage Degradation Studies

This work was completed in late 1986 when we were able to show that low voltage failure was related to physical defects such as cracks and porosity and the presence of water. No further work is planned in this area. (Appendix D)

Relaxor Degradation Studies

These studies are in progress using commercial materials from TAM Ceramics on DuPont and laboratory prepared materials.

The long term stability of ceramic capacitors is of a great importance to the electronics industry. Presently, two mechanisms of degradation failure have been identified. One is associated with an intrinsic mechanism and the other an extrinsic mechanism. This research program is directed at developing an understanding of the two failure mechanisms in both BaTiO_3 and relaxor based dielectrics. To facilitate this research we have been making extensive electrical measurements and microstructural evaluations on both commercial and laboratory-prepared specimens. The measurements being performed include:

- 1) Current as a function of time, temperature, and applied field to evaluate both low and high voltage degradation.
- 2) Destructive microstructural evaluations.
- 3) Thermally stimulated polarization/depolarization current (TSPC/DC) measurements.

Relaxor Preparation

These studies are in progress and involve both polymeric precursor and mix oxide preparation techniques. The most important results are contained in Appendices F through K.

The polymeric precursor preparation technique is very promising since it offers the opportunity of making capacitors at temperature below 950°C and allows the preparation of film capacitors from organic films obtained by spinning the polymer precursor onto substrates such as silicon. This work is therefore being expanded with the intent of gaining an understanding of the polymer precursor process.

Publications Resulting from ONR Program 1/85 - 1/87

Degrees

D. Viehland, "Contributions to the Electrical and Mechanical Phase Diagram of La-Doped Lead Zirconate Titanate," M.S. Thesis, 1986.

F.C. Jang, "Dielectric and Electrical Properties of BaTiO_3 Composites," M.S. Thesis, 1985.

C.J. Brannon, "An Investigation of the Low Voltage Failure Mechanism in Multilayer Ceramic Capacitors," M.S. Thesis, 1986.

W. Huebner, "TSPC/DC Studies on BaTiO_3 Dielectrics," Ph.D. Thesis, 1987.

D. Hong, "The Effect of Excess Lead Oxide on the Sintering Characteristics and Dielectric Properties of Lead Magnesium Niobate Ceramics," M.S. Thesis, 1987.

D. Beck, "Effects of Additions to the Physical and Dielectric Properties of Lead Magnesium Niobate," M.S. Thesis, 1986.

Publications and Presentations

W. Huebner and H.U. Anderson, "TSPC/DC Measurements on Barium Titanate,"

(Appendix B)

W. Huebner, F.C. Jang, and H.U. Anderson, "Dielectric and Electrical

Properties of BaTiO_3 Composites," (Appendix C)

C.J. Brannon and H.U. Anderson, "An Investigation of the Low Voltage

Failure Mechanism in Multilayer Ceramic Capacitors," 3rd U.S./Japan

Seminar on Dielectrics and Piezoelectrics, Toyama, Japan, Nov. 9-12,

1986. (Appendix D)

H.U. Anderson, M.J. Pennell, and J.P. Guha, "Polymeric Synthesis of Lead

Magnesium Niobate," (Appendix F)

J.P. Guha and H.U. Anderson, "Preparation of Perovskite $\text{Pb}(\text{Mg}_{1/3}\text{Nb}_{2/3})\text{O}_3$

Using $\text{Pb}_3\text{Nb}_2\text{O}_8$ and MgO ," J. Am. Cer. Soc., 69 C287 (1986). (Appendix

H)

J.P. Guha and H.U. Anderson, "Microstructural Inhomogeneity in Sintered

$\text{Pb}(\text{Mg}_{1/3}\text{Nb}_{2/3})\text{O}_3$ - PbTiO_3 Based Dielectrics," J. Am. Cer. Soc., 70, March

1987. (Appendix I)

C.J. Brannon and H.U. Anderson, "Low Voltage Degradation of Capacitors,"

39th Pacific Coast Regional Meeting, Am. Cer. Soc., Oct. 22-24, 1986,

Seattle, Wa.

APPENDIX A

TSPC/DC Studies on BaTiO_3

Summary - Ph.D. Thesis, W. Huebner

ABSTRACT

A new method of studying ferroelectric materials has been characterized through measurements on BaTiO_3 : Thermally-Stimulated Polarization/Depolarization Current (TSPC/DC) measurements. TSPC/DC spectra yield information concerning the temperature and order of phase transitions, the degree of domain reorientation during heating and poling, the pyroelectric coefficient, DC electrical degradation, resistivity, and the activation energy of conduction, as well as the influence of nonstoichiometry and impurities on these properties. Measurements were performed on nonstoichiometric, Sr-shifted, Zr-shifted, donor-doped, and acceptor-doped BaTiO_3 , as well as several commercial capacitors.

The form of TSPC/DC spectra in terms of current magnitude, the presence of peaks, and current reversal is dependent upon the resistivity, and change in the polarization during heating. Current peaks are observed at the phase transitions, the magnitude and sign of which are dependent on the difference in the spontaneous polarization of the two phases, and the order of the phase transition.

TSC results showed the ferroelectric-paraelectric phase transition in Ba_xTiO_3 is first order only for $x \leq 1.000$, if grain sizes are greater than several microns. Increasing the field increases the rhombohedral-orthorhombic phase transition temperature by $3.4 \times 10^{-3} \text{ K}\cdot\text{cm/V}$, decreases the orthorhombic-tetragonal phase transition temperature by $4.8 \times 10^{-3} \text{ K}\cdot\text{cm/V}$, and increases the tetragonal-cubic phase transition temperature by $1.3 \times 10^{-3} \text{ K}\cdot\text{cm/V}$. Phase transition temperatures are also affected by the grain size; fine-grained

materials shift the phase transition temperatures an amount predicted from the magnitude of the internal stress and Devonshire theory.

Diffuse phase transitions observed in Zr-shifted and Nb-doped BaTiO_3 , and the temperature-independent dielectric constant of commercial capacitors are due to compositional inhomogeneities, as evidenced by the small fluctuations in current during depolarization.

TSPC-1 and TSPC-2 spectra showed nonstoichiometry and larger grain sizes increases the conductivity, decreases the activation energy of conduction, and results in enhanced degradation. Those specimens which degrade exhibit greater current levels in the TSPC-2 spectra, and a non-zero pyroelectric signal in the paraelectric state, indicative of an anomalous polarization due to the migration of $V_O^{\bullet\bullet}$.

$\text{Ba}_{1-x}\text{Sr}_x\text{TiO}_3$ compositions for $x = 0.25, 0.30$, and 0.35 exhibit anomalously high dielectric constants at the Curie point, the maximum being 29,000 for the $x = 0.25$ specimen. This behavior is attributed to a "pure" second order transition for which the permittivity approaches infinity on a theoretical basis. Slight nonstoichiometry drastically reduced the K to "normal" levels.

Donor and acceptor doping had a marked effect on the ferroelectric behavior in terms of altering the phase transition temperatures and the resistivity, both of which are clearly resolved by the TSC spectra.

APPENDIX B

TSPC/DC Measurements on Barium Titanate

W. Huebner and H. Anderson

Applications of Ferroelectrics

June 5-11, 1986

TSPC/DC MEASUREMENTS ON BARIUM TITANATE

Wayne Huebner
Materials Research Laboratory
Pennsylvania State University
University Park, PA 16802

Harlan U. Anderson
Ceramic Engineering Department
University of Missouri-Rolla
Rolla, MO 65401

Abstract

Thermally-stimulated polarization/depolarization current (TSPC/DC) measurements were made on high-purity doped and undoped BaTiO₃ as a function of applied field, heating rate, dopant level, and Ba:Ti ratio. The form of the TSPC/DC curves is dependent upon both the resistive and ferroelectric properties of BaTiO₃. For TSPC spectra, current peaks are exhibited due to the change in in magnitude and direction of the spontaneous polarization with changing crystal structure. In particular, whether the phase transition is first or second order influences the existence and magnitude of the current peaks.

TSDC measurements are essentially dynamic pyroelectric measurements and as such are useful in determining the pyroelectric coefficient and the magnitude of the spontaneous polarization. The TSDC current did not approach zero in the paraelectric region for some of the specimens, indicative of an anomalous polarization present due to the migration of charged oxygen vacancies. This information is useful for analyzing DC electrical degradation.

Variation in the Ba:Ti ratio affects the grain size distribution, and hence, the ease of domain switching. This directly affects the presence and magnitude of current peaks. The Ba:Ti ratio also affects the activation energy of conduction, resistivity, and degradation behavior, all of which are reflected by the magnitude of the TSPC/DC current in the paraelectric region.

Introduction

In thermally-stimulated processes, a particular property of a material is measured as a function of temperature, usually from a "low" temperature which freezes in processes of interest. The system of interest usually exists in a non-equilibrium state (i.e. poled), which is achieved by excitation at the low temperature or during cooling. Specifically, TSC measurements involve monitoring the current passing through a material subjected to a DC stress during heating.

TSPC/DC measurements have been extensively used for studying charge transport in insulators.¹⁻⁶ Alkali motion and dipolar relaxation times in glasses¹, vacancy dipole reorientation in halides², point defect energy levels in insulators³, and energy levels of trapping and recombination centers in semiconductors⁴ have all been characterized by TSPC/DC techniques. Chen⁵ and Braunlich⁶ provide complete reviews of past uses of TSC measurements. The purpose of this study was to determine if TSPC/DC measurements would be useful in the study of ferroelectric materials.

Experimental Procedure

The BaTiO₃ powders utilized in this study were prepared by an organometallic technique⁷. Disc specimens were pressed and subsequently sintered in air at various temperatures and times in order to precisely control the microstructure. All discs were electroded using an unfritted platinum paste.

The apparatus used for the TSPC/DC and dielectric measurements is shown in Figure 1. It consists of an atmosphere-controlled, stainless steel chamber which houses a removable inner core assembly. Heating tape wrapped around the bottom of the tube and connected to a Eurotherm 211 controller allows precise control of the heating rate. A computer-controlled HP 4140 picoammeter/DC voltage source was used for current monitoring. Current sensitivity for the system was 10⁻¹⁴ amps. Capacitance and dissipation factor data were collected at 1 kHz using a General Radio 1689 RLC digi-bridge.

Figure 2 illustrates the sequence used for the TSC measurements, and is described as follows:

1. 1st Polarization: After a vacuum bake-out at 165°C and cooling to -100°C, a voltage was applied to the specimen, and the current monitored during heating at a constant rate. Monitored temperature range was from -100 to 165°C. This current spectra is denoted TSPC-1.
2. 2nd Polarization: After the first polarization, the specimen was immediately

quenched to -100°C with the field applied. The now poled specimen was then heated and the current monitored as in TSPC-1. This current spectra was denoted TSPC-2.

3. **Depolarization:** Following TSPC-2, the specimen was quenched to -100°C with the field applied. At this point the field was removed, and the current monitored during heating as before. This current spectra was denoted TSDC.

Heating rates varied from 2.0 to $8.0^{\circ}\text{K/minute}$, and applied fields ranged from 250-2000 V/cm.

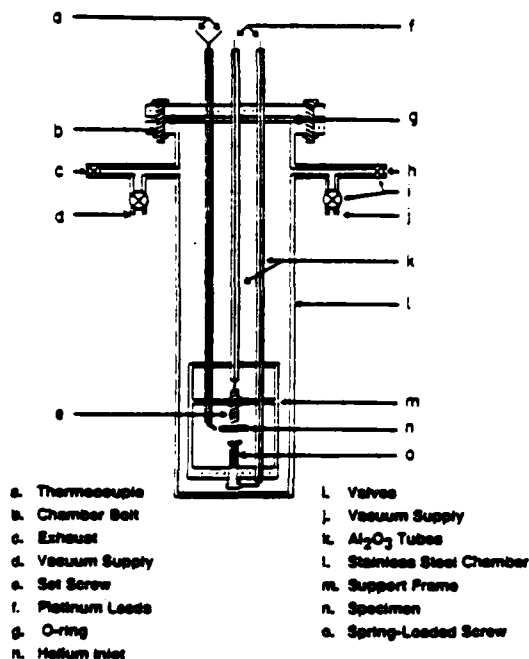


Figure 1. TSPC/DC measurement apparatus.

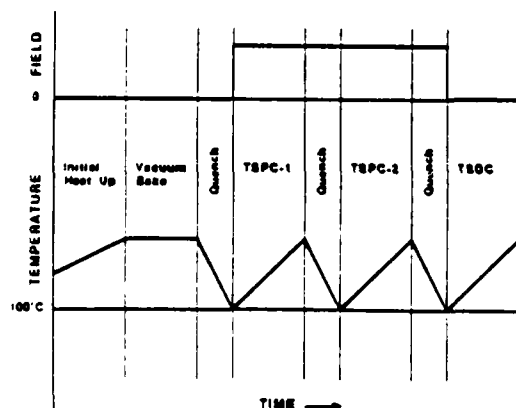


Figure 2. TSPC/DC measurement sequence

Results and Discussion

The TSPC/DC behavior is plotted as $\pm \log$ current density versus temperature. Positive current corresponds to resistive current, i.e. electron flow towards the anode. Negative current corresponds to electron flow in the opposite direction, indicative of the charging or displacement current which flows during polarization of the ferroelectric. In a TSPC experiment then, the total current flowing at any time is:

$$J_T(T) = J_D(T) + J_R(T) \quad (1)$$

where $J_T(T)$, $J_D(T)$, and $J_R(T)$ are the total, displacement, and resistive current densities respectively. During a TSDC experiment, no field is applied and the current density becomes:

$$J_D = \frac{dP_S}{dt} = \frac{dP_S}{dT} \frac{dT}{dt} \quad (2)$$

where dP_S/dT is the change in spontaneous polarization with temperature (the pyroelectric coefficient), and dT/dt is the heating rate. From a TSDC measurement the spontaneous polarization is determined from:

$$P_S = \int J_D(T) \frac{dT}{dt} \quad (3)$$

Figures 3 and 4 contain the dielectric and TSPC/DC behavior for a stoichiometric BaTiO_3 specimen with a grain size of 10 microns and 96% theoretical density. The dielectric constant exhibits typical behavior, with maxima at the three phase transitions. TSPC-1 initially exhibits positive current in the rhombohedral region; the dipoles are "frozen-in" and unable to align with the field. As the specimen undergoes a phase transition to orthorhombic symmetry a peak is observed, the magnitude of which is proportional to the change in spontaneous polarization and the degree of poling which occurs for a poling field of 1000 V/cm. A transition to positive current occurs as the resistive component of the current again dominates, with a similar current reversal and peak at the orthorhombic-tetragonal phase transition.

The behavior of the TSPC curve is of particular interest at the Curie temperature. Specimens with first order ferroelectric-paraelectric transitions exhibit a large negative peak as the spontaneous polarization changes discontinuously to zero. A specimen undergoing a second order transition does not exhibit a peak, as the $\text{Ba}_{0.99}\text{Ti}_{1.005}\text{O}_3$ specimen in Figure 5; the spontaneous polarization changes

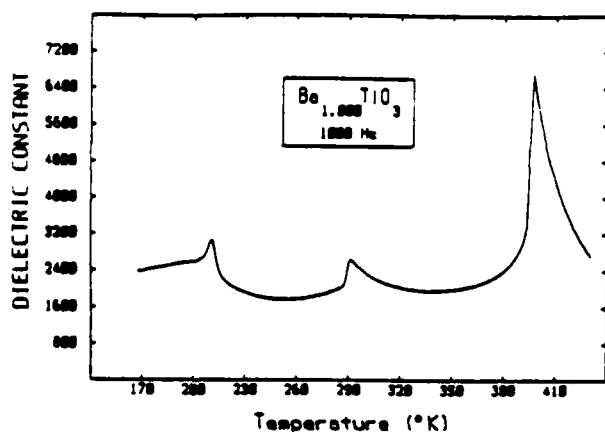


Figure 3 Dielectric constant of stoichiometric BaTiO₃.

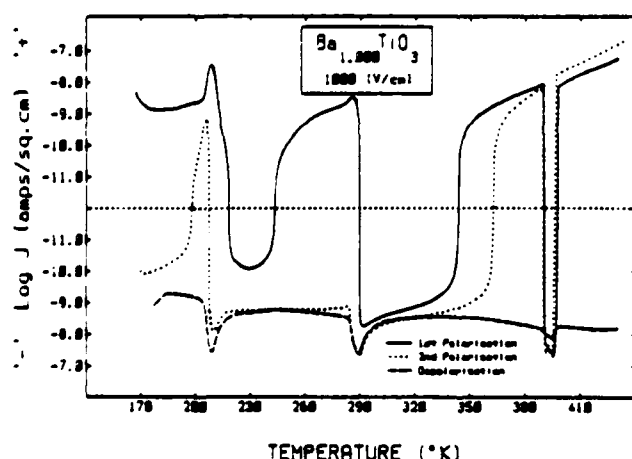


Figure 4 TSPC/DC spectra of stoichiometric BaTiO₃.

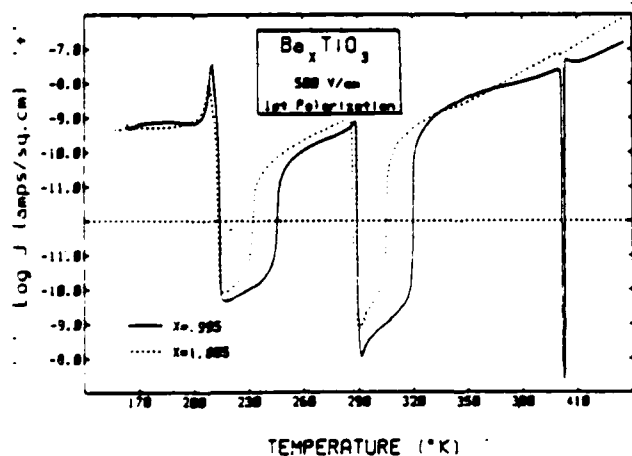


Figure 5 Comparison of TSPC-1 spectra for Ba Ti = 995 and 1.005

continuously to zero. Figure 6 summarizes this behavior.

The magnitude of TSPC-1 in the paraelectric region is proportional to the resistivity of the material, $\rho(T)$, which is found by dividing the applied field by the current density. The change in current density with temperature is exponentially proportional to the activation energy of conduction, which can be calculated assuming Arrhenius behavior. The activation energy for the BaTiO₃ specimen of Figure 4 is 1.0 eV, which agrees well with published data. This activation energy is composed of both the carrier concentration and mobility terms.

The TSPC-2 of Figure 4 is similar to that of TSPC-1, but reflects the fact that the specimen is already in a poled state prior to heating.

The TSDC spectra contained in Figures 4, 7 and 8 simply reflect the pyroelectric nature of BaTiO₃. Dividing the current density by the heating rate yields the pyroelectric coefficient. These results agree well with those published earlier by Perlis et al.⁷ for polycrystalline BaTiO₃. Figure 8 exhibits the degree of poling achieved for fields from 250-2000 V/cm. Increasing the poling field not only increases the discharge current during depolarization, but also decreases the temperature at which the orthorhombic-tetragonal phase transition occurs (Figure 9).

Figure 10 contains the TSDC spectra of excess barium compositions which exhibit DC electrical degradation at 500 V/cm⁸. Increasing the amount of excess barium increases the degradation rate, which is believed to be due to charged oxygen vacancy migration. The accumulation of oxygen vacancies at the cathode results in a quasi-space charge accumulation referred to as an anomalous polarization. This

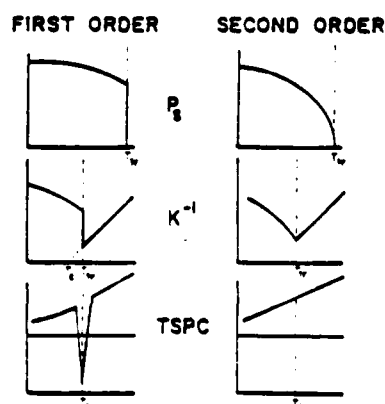


Figure 6 Variation of the spontaneous polarization and its affect on TSPC and inverse susceptibility

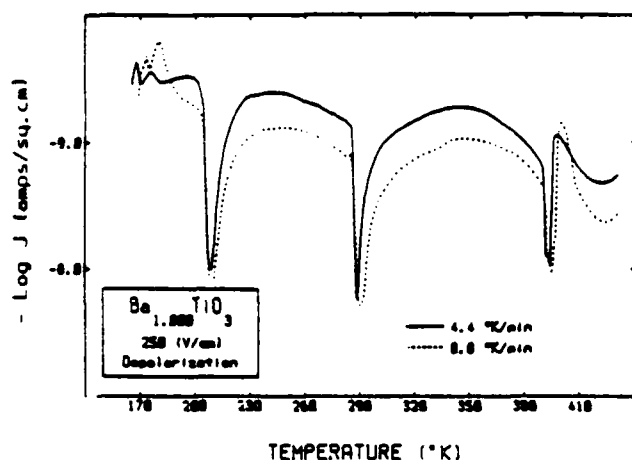


Figure 7 TSDC behavior of BaTiO₃ as a function of heating rate.

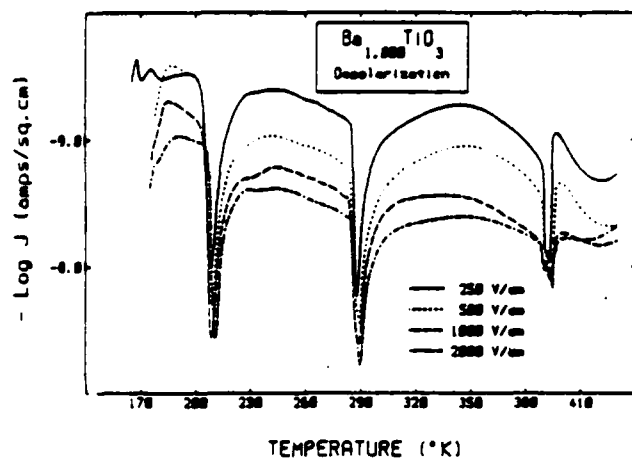


Figure 8 TSDC behavior of BaTiO₃ as a function of applied poling field.

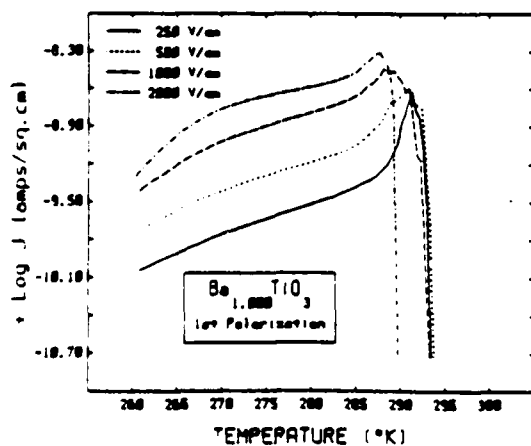


Figure 9 TSPC behavior at the orthorhombic-tetragonal phase transition as a function of applied field

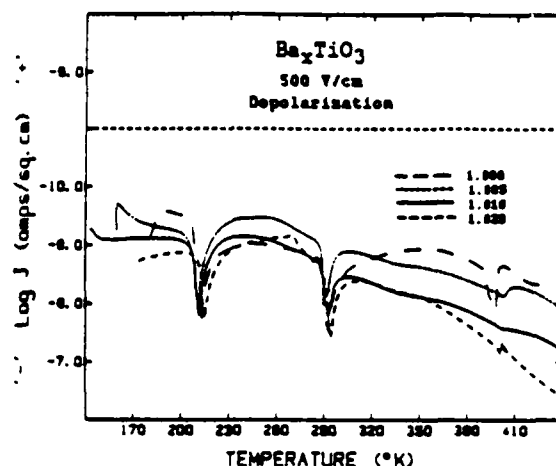


Figure 10: TSDC behavior of excess barium compositions.

effect is clearly illustrated in Figure 10, the pyroelectric current does not approach zero as expected in the paraelectric region. Instead the current continues to increase, the effect being larger in those specimens more prone to degradation.

Conclusions

TSPC/DC measurements are useful in characterizing the properties of ferroelectric materials. Pyroelectric coefficients and the spontaneous polarization are easily obtained from the TSDC spectra, while the TSPC spectra are useful in the analysis of phase transitions and domain switching. The purpose of this paper was to present the characteristic results one obtains in TSPC/DC measurements, and is by no means complete in terms of quantitative analysis. A full treatment of the mathematical aspects and background may be found elsewhere⁹

References

1. C.M. Hong and D.E. Day, "Thermally Stimulated Currents in Sodium Silicate Glasses," *J. Amer. Cer. Soc.*, **64**:61-68 (1981).
2. C. Bucci, "Ionic Thermocurrents in Alkali Halide Crystals Containing Substitutional Beryllium Ions," *Phys. Rev.*, **164**:1200-06 (1967).
3. J.G. Simmons and G.W. Taylor, "High Field Isothermal Currents and TSC in Insulators Having Discrete Trapping Levels," *Phys. Rev. B*, **5**:1619-29 (1972).
4. J.G. Simmons et al., "TSC in Semiconductors and Insulators Having Arbitrary Trap Distributions," *Phys. Rev. B*, **7**:3714-19 (1973).
5. R. Chen, "Review of Methods for Kinetic Analysis of Thermally Stimulated Processes," *J. Mater. Sci.*, **11**:1521-41 (1976).
6. P. Bannett, *Thermally Stimulated Relaxation in Solids*, Topics in Applied Physics, Springer-Verlag, Berlin, 1979.
7. T.A. Peris, "Primary Pyroelectricity in Barium Titanate Ceramics," *J. Appl. Phys.*, **29**:1297-1302 (1958).
8. W. Hoebner et al., "Reliability Studies of Ceramic Capacitors," ONR Progress Report #N00014-82-K-0294 (1984).
9. W. Hoebner, *Thermally Stimulated Current and Dielectric Properties of Barium Titanate*, Ph.D. Dissertation, University of MO - Rolla, 1986.

APPENDIX C

Dielectric and Electrical Properties of BaTiO_3 Composites

W. Huebner, F. Jang and H. Anderson

1
Multiphase and Composite Ceramics
21st Univ Conf on Ceramic Science
held at PSU, Univ Park Pa
July 17-19, 1985

To be publ
by Plenum Publ

DIELECTRIC AND ELECTRICAL PROPERTIES OF BaTiO₃ COMPOSITES

W. Huebner, F.C. Jang, and H.U. Anderson

Department of Ceramic Engineering
University of Missouri - Rolla
Rolla, MO 65401

ABSTRACT

In this investigation composites of unconsolidated BaTiO₃ powder ($\geq 99.9\%$ purity, $\leq 0.1 \mu\text{m}$ crystallite size) or partially-sintered BaTiO₃ with either air or polymer were studied. The purpose of this study was to measure the dielectric and electrical properties of the composites, and to determine how well these properties fit existing theories concerning fine-grained permittivity and dielectric mixing rules.

INTRODUCTION

Recent investigations^{1,2} on high-purity BaTiO₃ have shown that partially-sintered specimens with sub-micron grain size and high porosity showed good resistance to dry atmosphere electrical degradation. However, porous specimens exhibit low dielectric constants, low breakdown strengths, and high water permeability. It is expected that filling the porosity with a polymer would improve the breakdown strength and water impermeability. The purpose of this investigation was to measure the dielectric and electrical properties of composites made from BaTiO₃ and either polymer or air, and to determine how well these properties fit existing theories concerning fine-grained permittivity and dielectric mixing rules.

Numerous rules appear in the literature which predict the dielectric constant of mixtures depending upon the relative volumes and permittivities of the constituents, as well as their shape and continuity. Articles by Reynolds and Hough³, Meredith and Tobias⁴, and Van Beek⁵ review the application and validity of most of these rules.

Niesel-Bruggeman⁶ found composites to obey:

$$K_c = \frac{1}{2} ((2E_p - E'_p) + ((E'_p - 2E_p)^2 + 8K_1K_2)^{\frac{1}{2}}) \quad (1)$$

where: K_c = composite dielectric constant
 K_1 = dielectric constant of phase 1
 K_2 = dielectric constant of phase 2
 V_1 = volume fraction of phase 1
 V_2 = volume fraction of phase 2

$$E_p = V_1K_1 + V_2K_2$$

$$E'_p = V_1K_2 + V_2K_1$$

Bottcher's⁷ equation has been found to apply to non-dilute systems and is given by:

$$\frac{K_c - K_1}{3K_c} = V_2 \frac{K_2 - K_1}{2K_c - K_2} \quad (2)$$

These particular mixing rules are of interest due to their applicability to the current experimental data.

Partially-sintered BaTiO₃ and unsintered BaTiO₃ powder exhibit unusual dielectric properties believed to be due to a surface layer effect. Anliker et al.⁸, while studying depolarization effects in very fine particle size BaTiO₃, observed a broad Curie transition which they attributed to a 100Å thick tetragonal surface layer which persisted well above the Curie temperature. Both Chynoweth's⁹ observation of assymetric pyroelectric effects and Triebwasser's¹⁰ observation of birefringence of BaTiO₃ single crystal surfaces have been explained by space charge layers. Numerous studies¹¹⁻¹⁷ of the switching time and dielectric constant of single crystals as a function of thickness indicate a nonferroelectric surface exists. English¹⁸, using electron-mirror microscopy, found the surface of BaTiO₃ to be ferroelectric. Goswami¹⁹ explained the absence of ferroelectric behavior in unsintered BaTiO₃ by a nonferroelectric surface layer. Thus there appears to be agreement concerning the existence of a surface layer, but its exact nature is not clearly understood.

Based solely on the existence of a low dielectric constant surface layer one would expect decreasing the grain size of polycrystalline BaTiO₃ would decrease the overall dielectric constant. However it is well known that a high dielectric constant can be obtained for sintered, dense, approximately 1µm grain size BaTiO₃. Numerous studies²⁰⁻²³ have shown room temperature permittivities can range from approximately 3500 - 6000. For single crystal BaTiO₃ the room temperature permittivities are 4000 and 170 along the a and c axes respectively. Buessem et al.²⁴ have proposed that the high permittivity in fine-grained BaTiO₃ arises from the absence of 90° twinning which gives rise to high internal stresses. This pertains only to sintered, polycrystalline specimens in which grains are constrained by the surrounding matrix. Goswami²⁵ has shown that unsintered powder of comparable density to sintered specimens does not show the anomalously high permittivity. Goswami^{19,25} also observed that progressive heat treatment of BaTiO₃ results in a gradual increase in permittivity and appearance of ferroelectricity. He ascribed this to the annealing out of lattice defects which removed the influence of a low dielectric constant, nonferroelectric surface.

It is not clear from the literature if sub-micron grain size BaTiO₃ can exhibit a similiar high permittivity at room temperature. Graham et al.²⁶ observed hot-pressed, sub-micron grain size BaTiO₃ exhibited a dielectric constant of 3000, but were unsuccessful in sintering specimens with sub-micron grain sizes. One of the goals of the present work is to partially-sinter high purity (> 99.9%), fine-grained (< 0.1µm) BaTiO₃ to study the dielectric properties of sub-micron BaTiO₃.

EXPERIMENTAL PROCEDURE

BaTiO₃ powders utilized in this study were prepared by an organometallic technique first described by Pechini²⁷. Resulting powders are chemically homogeneous, uniformly-sized, and approximately 0.1µm in diameter. X-ray powder diffraction patterns showed line-broadening effects but revealed the powder to have tetragonal symmetry.

Specimens for measurement on unsintered BaTiO₃ compacts were pressed in

a $\frac{1}{2}$ inch diameter stainless steel die at various pressures up to 75000 psi without the addition of a binder. Those specimens used for the sintering study were pressed at 50000 psi with the addition of 8 weight % binder. Green densities were approximately 62% theoretical.

Porous specimens were prepared by partial-sintering at temperatures from 500 - 1000°C, for times of 1 - 4 hours in a SiC muffle tube furnace. Typical density and shrinkage curves are contained in Figures 1 and 2. Figures 3a-b contain the corresponding SEM micrographs. The process of preparing polymer composites from these specimens is as follows: 1) Disks are initially dried for 24 hours under vacuum at 200°C to minimize water vapor. 2) After cooling, disks are then immersed in a styrene monomer-initiator (0.1 weight % AIBN) solution under vacuum. 3) Initial polymerization is then accomplished by slowly raising the temperature from 30-60°C over a period of 120 hours. 4) The polymerization is completed by annealing the disks at 60°C for 48 hours under atmospheric pressure.

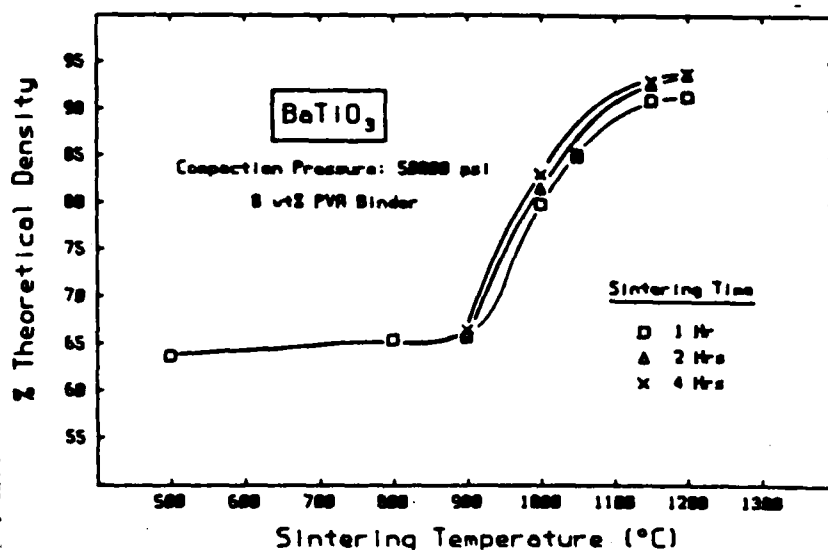


Fig. 1. Theoretical density of specimens sintered at various temperatures and times..

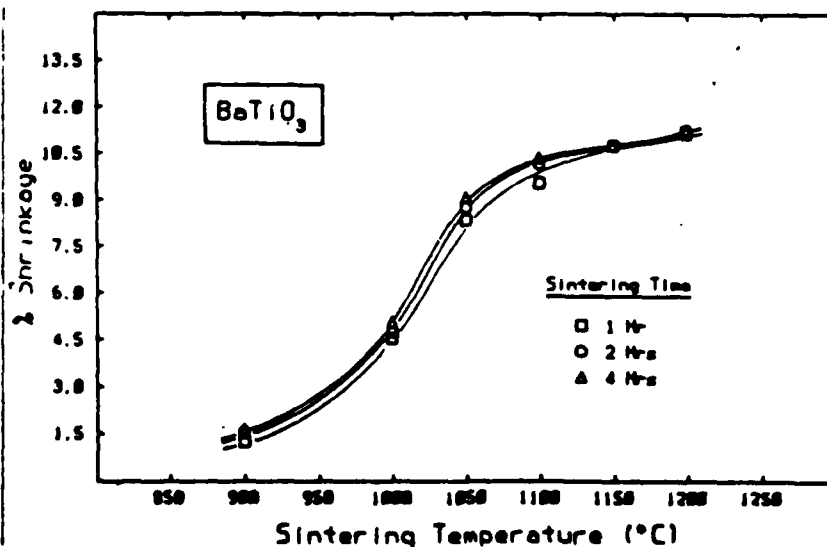
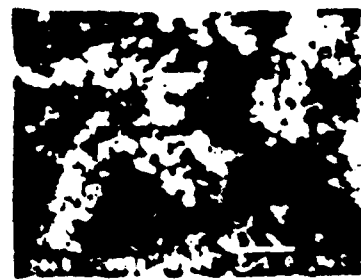


Fig. 2. Shrinkage of specimens sintered at various temperatures and times.

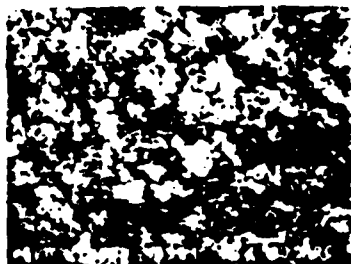


500°C-1hr

FRACTURE SURFACES
OF
PARTIALLY - SINTERED
 BaTiO_3



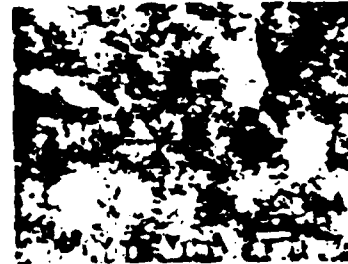
800°C-1hr



900°C-1hr



900°C-2hrs



900°C-4hrs

Fig. 3a. Scanning electron micrographs of BaTiO_3 specimens partially-sintered at 500, 800, and 900°C.



900°C-8hrs

FRACTURE SURFACES
OF
PARTIALLY - SINTERED
 BaTiO_3



900°C-24 hrs



1000°C-1hr



1000°C-2hrs



1000°C-4hrs

Fig. 3b. Scanning electron micrographs of BaTiO_3 specimens partially-sintered at 900 and 1000°C.

The filling efficiency of the polymer into the open porosity was determined by scanning electron microscopy and density measurements using:

$$\rho_c = \rho_a V_a + \rho_b V_b \quad (3)$$

where: ρ_c = composite density

ρ_a, ρ_b = BaTiO_3 , polymer density

V_a, V_b = BaTiO_3 , polymer volume fraction

For all of the specimens studied the polymer filled greater than 95 percent of the total open porosity.

Thin films of polymer with up to 32 volume percent BaTiO_3 filler were prepared by dispersing unsintered BaTiO_3 powder into a liquid formed by dissolving polystyrene in dioxane. The mixture was cast onto a glass plate, the solvent allowed to partially evaporate from 20 - 60°C, and then the film was heat-cured at 60°C under vacuum. Films from this simple process are approximately 0.010 inches thick.

Air-drying silver paint was used as the electrode material for all the specimens. Capacitance and dissipation factor were measured up to 100 kHz as a function of temperature using a computer-controlled General Radio 1689 RLC bridge. Resistivity measurements were made using a Hewlett Packard 4140 pA/DC voltage source. These measurements were made in a dry atmosphere. DC breakdown strengths were measured in silicon oil at room temperature.

RESULTS AND DISCUSSION

The 1 kHz dielectric constant of a 170°C, vacuum-annealed, unsintered BaTiO_3 compact (= 60% dense) is shown in Figure 4 as a function of temperature. The dissipation factor is not shown but is less than 2% over the temperature range measured. These results agree with those of Goswami¹⁹ as far as the magnitude of the dielectric constant and nonferroelectric behavior are concerned. The low dielectric constant can be explained by the existence of a nonferroelectric surface layer^{11-17,19}. Chynoweth⁹ categorized the proposed surface layers into two main groups: 1) Space charge or exhaustion layers in the range of 0.1 μm thick, which are generally ferroelectric, and 2) Chemically or mechanically disturbed layers composed of a lossy, low dielectric constant, nonferroelectric material in the range of 10 Å thick.

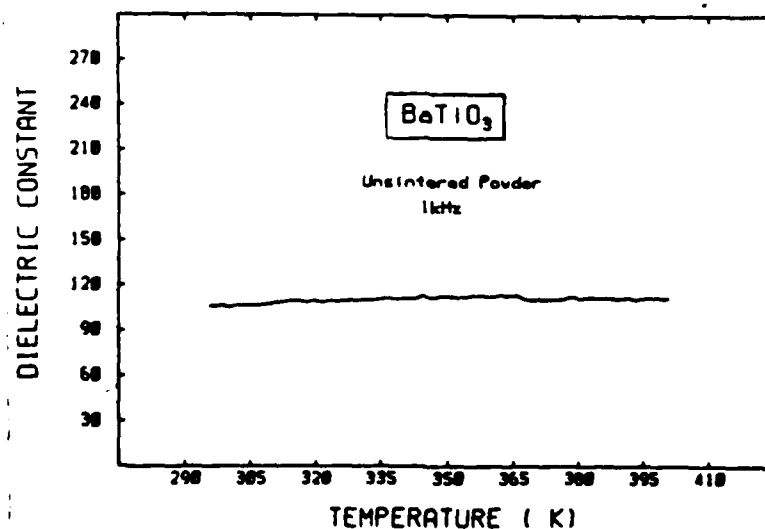


Fig. 4. Dielectric constant vs. temperature for an unsintered BaTiO_3 specimen.

The effect of increasing heat treatment on the dielectric constant is shown in Figures 5-7. The increase in dielectric constant is related to the degree of grain growth and sintering. Grain size vs. sintering temperature is shown in Figure 8; little grain growth occurs for temperatures less than 900°C. These results show that 0.1 μm grains do display broad transitions at the Curie point of 120°C and as the grain size approaches 1 μm the peak becomes sharper. As can be seen in Figure 9, in the region of constant grain size the dielectric constant increases with the percent shrinkage. Thus it appears that fine-grained behavior is strictly a function of the sintering conditions and the degree of shrinkage.

In a previous report of Buessem et al.²⁴ it was proposed that the high dielectric constant of 1-3 μm BaTiO_3 is due to the absence of 90° twinning which gives rise to internal stress below the Curie temperature. Figure 9 is nearly identical in form to the permittivity vs. stress curve derived for fine-grained BaTiO_3 by Buessem. Due to the striking similarity this suggests that internal stress in a compact is proportional to the shrinkage (ie: the degree of intergranular contact), and that the enhancement of the dielectric constant with increasing shrinkage may be understood in these terms. It appears that internal stress increases as shrinkage increases from 1 - 1.7%.

When applying mixing rule theories to BaTiO_3 composites with either air or polymer it is important to distinguish between unsintered and sintered results. Figure 10 is a plot of log K vs. volume fraction air/polymer for the BaTiO_3 specimens studied. Application of either the Niesel-Bruggeman or Bottcher mixing rules, both of which fit the data, results in zero porosity dielectric constants of 500 and 5000 for unsintered and sintered BaTiO_3 respectively. These results indicate that microstructures with less than 1 μm grains can produce enhanced dielectric constants.

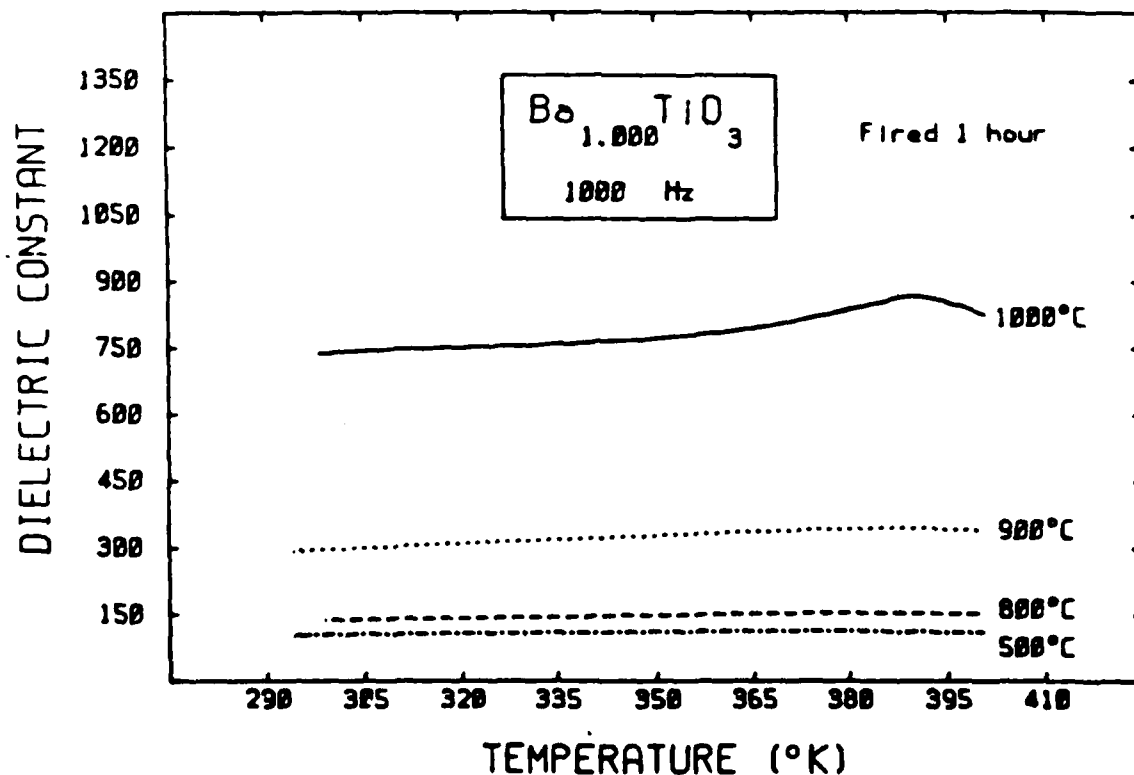


Fig 5. Dielectric constant vs. temperature for BaTiO_3 specimens sintered for 1 hour at various temperatures.

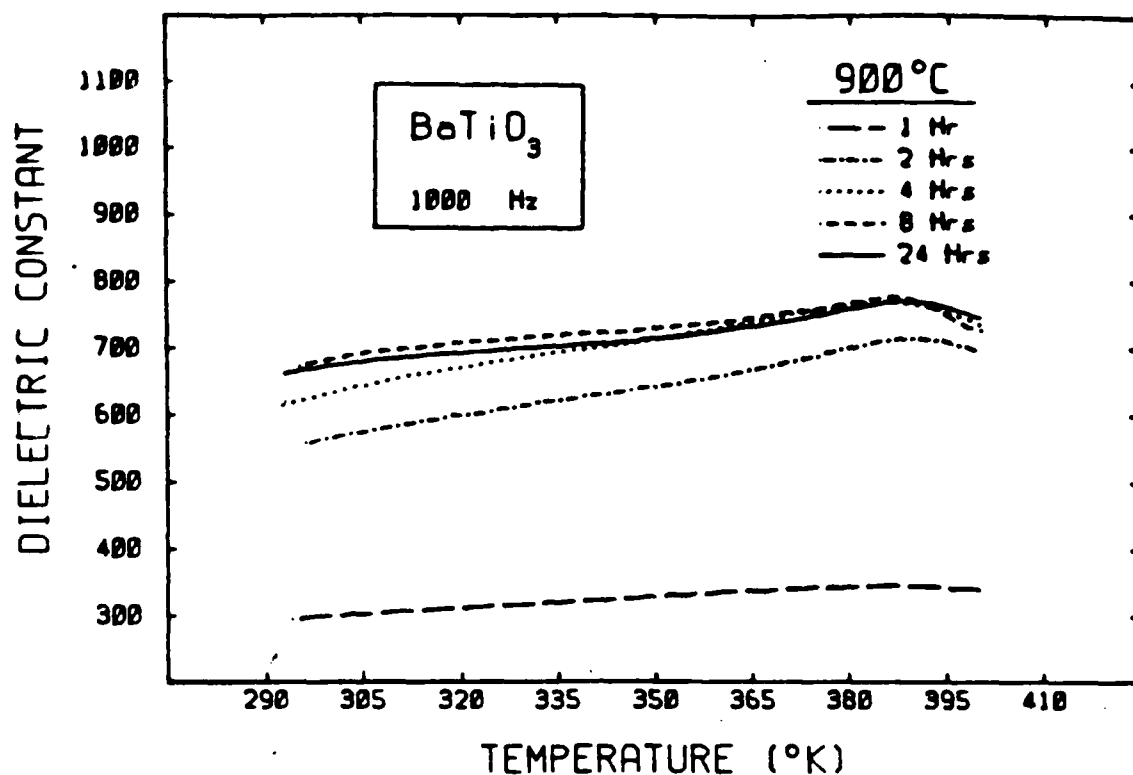


Fig. 6. Dielectric constant vs. temperature for BaTiO_3 specimens sintered at 900°C for various times.

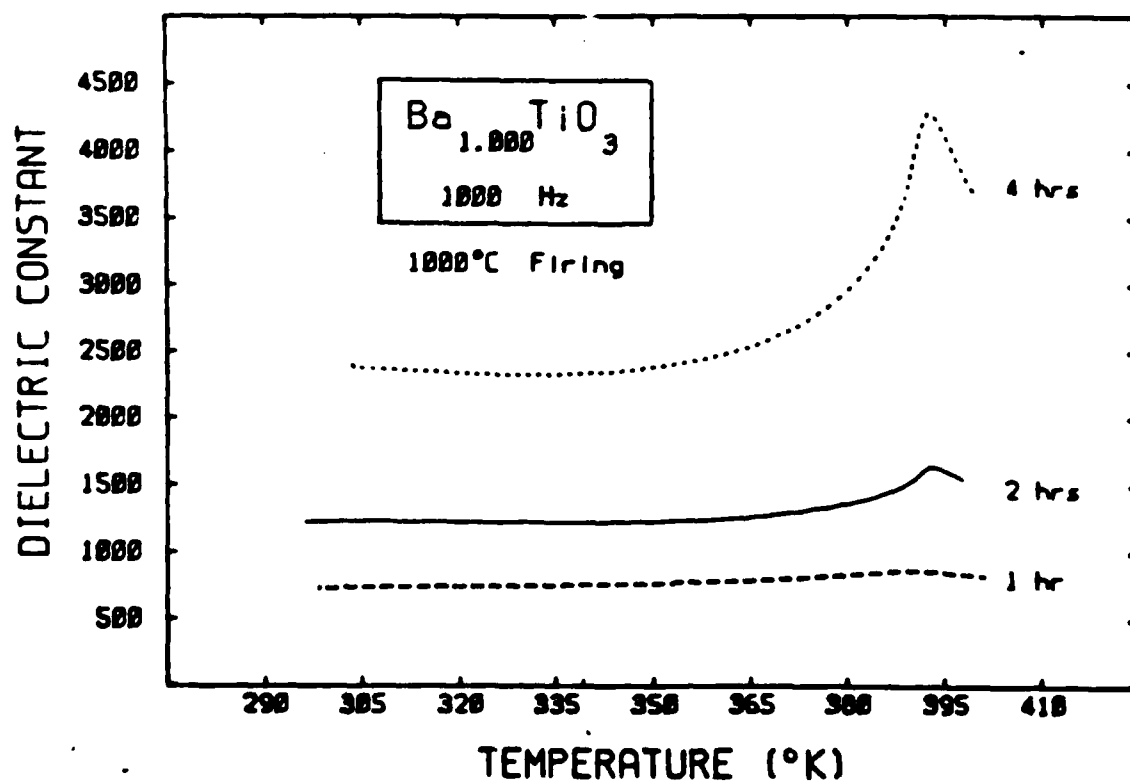


Fig. 7. Dielectric constant vs. temperature for BaTiO_3 specimens sintered at 1000°C for various times.

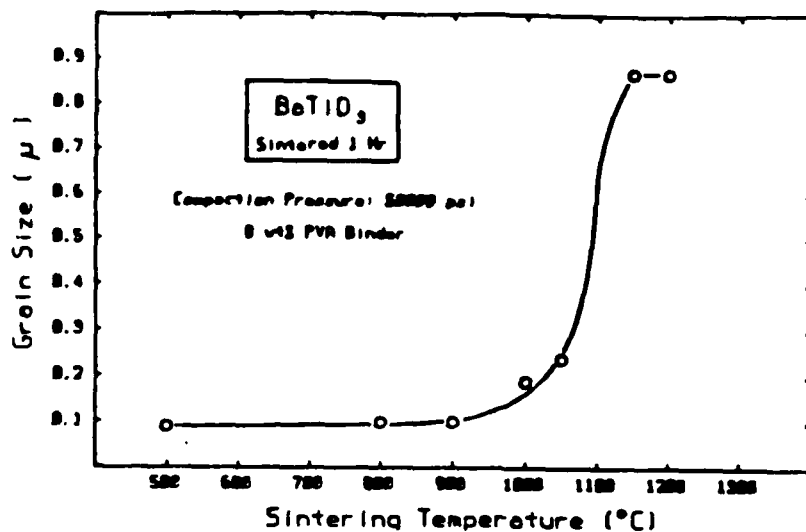


Fig. 8. Grain size vs. sintering temperature of the BaTiO₃ specimens sintered 1 hour.

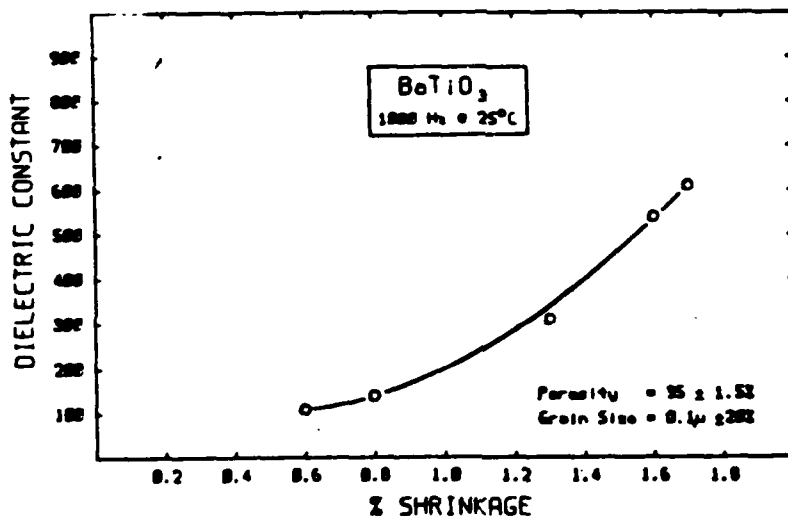


Fig. 9. Dielectric constant vs. % shrinkage for BaTiO₃ specimens with 0.1 μm grain size.

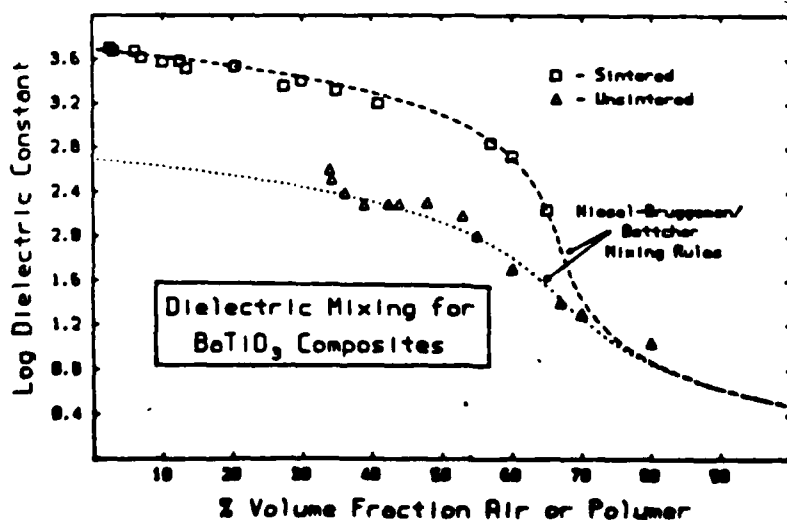


Fig. 10. Application of mixing rules to the dielectric properties of BaTiO₃ composites.

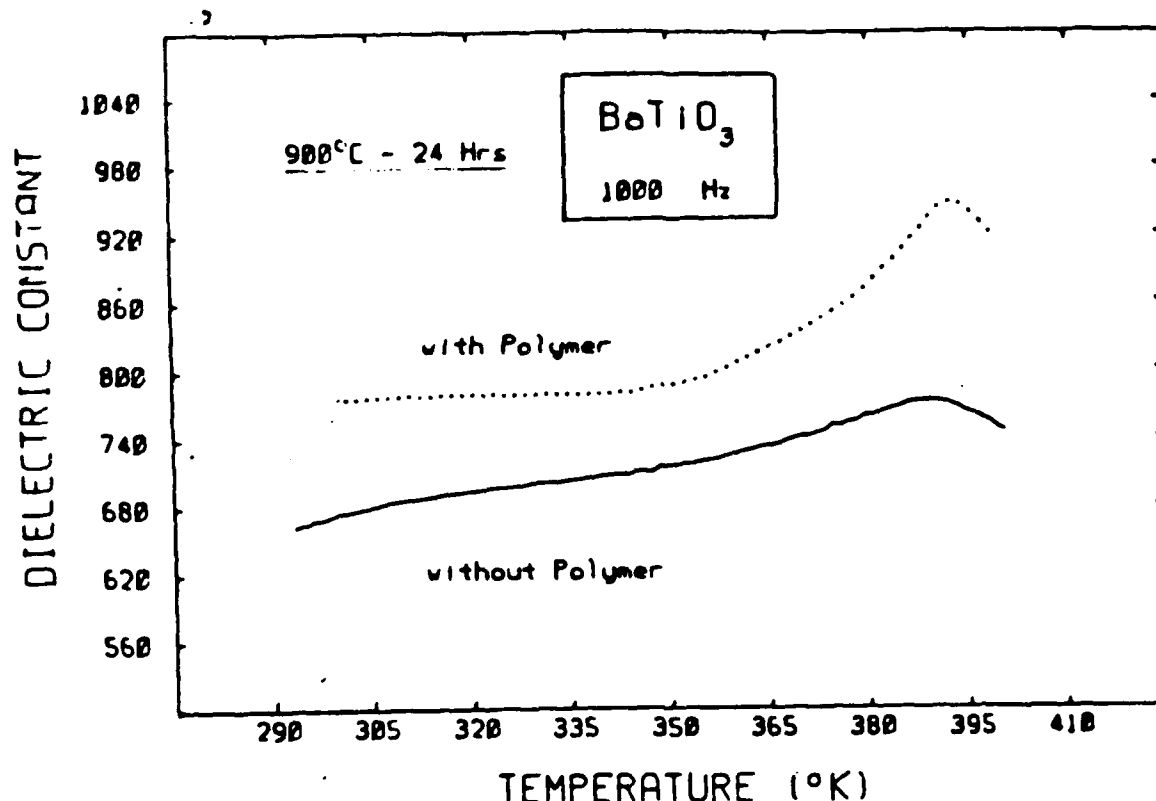


Fig. 11. Dielectric constant vs. temperature for BaTiO₃ specimens sintered at 900°C for 24 hours, with and without polymer.

As can be seen in Figure 11, addition of a polymer to porous BaTiO₃ enhances the dielectric constant and further develops the peak at the Curie point. It appears the polymer phase increases the internal stress by intergranular coupling. The restoration of ferroelectricity due to the polymer phase implies the previously-proposed nonferroelectric surface layer is not due to a high concentration of lattice defects.

Breakdown strength measurements were made on specimens which were vacuum-dried at 125°C. DC breakdown strengths for BaTiO₃-air composites averaged approximately 90 kV/cm, and BaTiO₃-polymer composites averaged 175 kV/cm. This effect can be explained by the high resistivity of the polymer phase, and the elimination of BaTiO₃ - air interfaces. In low density BaTiO₃, the "weak spots" are intergranular pores, which are assumed to be the origin of the dielectric breakdown. These potential breakdown sources are eliminated by the polymer phase, resulting in an improved breakdown strength. The high-resistivity polymer phase also inhibits electron avalanche.

The resistivity measurements made on the composite specimens showed the addition of a polymer did not effect the resistivity. Room temperature resistivities were approximately 10¹⁴ ohm-cm, and 10¹³ ohm-cm at 85°C.

Not shown figuratively, but the present study has also found the addition of a polymer to porous BaTiO₃ eliminates the detrimental effect of water vapor on the dielectric properties. Porous specimens exhibit a non-linear dielectric constant and dissipation factor in the presence of a humid atmosphere, while polymer-impregnated specimens do not.

SUMMARY

- 1) BaTiO_3 with grain size less than $1.0 \mu\text{m}$ can produce enhanced dielectric constants.
- 2) The increase in dielectric constant with increasing shrinkage is due to the increase in internal stress associated with increasing intergranular contact.
- 3) Composite dielectric constants of compacts made from unsintered powder agree well with either the Niesel-Bruggeman or Bottcher mixing rules; the zero-porosity dielectric constant extrapolates to approximately 500.
- 4) Composite dielectric constants of partially-sintered (shrinkage $\leq 5\%$, no grain growth) compacts also agree with the Niesel-Bruggeman and Bottcher mixing rules; the zero-porosity dielectric constant extrapolates to approximately 5000.
- 5) Polymer- BaTiO_3 composites exhibit higher dielectric constants, lower dissipation factors, higher breakdown strengths, and impermeability to water as compared to porous BaTiO_3 .

ACKNOWLEDGMENT

The authors would like to thank Dr. H. Yasuda for his advice concerning the polymer impregnation. This work was partially sponsored by the Office of Naval Research and Hughes Aircraft Company.

REFERENCES

1. D.A. Anderson, and W. Huebner, "Electrical Degradation of High-Purity BaTiO_3 ," Presented at the 1985 American Ceramic Society National Convention in Cincinnati, OH, May 26-30.
2. W. Huebner, H.U. Anderson, and D.E. Day, "Reliability Studies of Ceramic Capacitors," ONR Progress Report, October 1984, Contract # N00014-82-K-0294.
3. J.A. Reynolds, and J.M. Hough, "Formulae for Dielectric Constant of Mixtures," Proc. Phys. Soc. Lond., B70:769 (1957).
4. R.E. Meredith and C.W. Tobias, "Resistance to Potential Flow through a Cubical Array of Spheres," J. Appl. Phys., 31:1270 (1960).
5. L.K.H. van Beek, "Dielectric Behavior of Heterogeneous Systems," Progress in Dielectrics, 7:69-114, ed. J.B. Birks, London: Heywood Books (1967).
6. W. Niesel, "Die Dielektrizitätskonstanten heterogener Mischkörper aus isotropen und anisotropen Substanzen," Ann. d Phys., 6:336 (1952).
7. C.J.F. Böttcher, "The Dielectric Constant of Crystalline Powders," Rec. Trav. Chim. Pays-Bas, 64:47 (1945).
8. M. Anliker, H.R. Brugger, and W. Käzig, "Behavior of Colloidal Seignettelectrics: III," Helv. Phys. Acta., 27:99 (1954).
9. A.G. Chynoweth, "Surface Space-Charge Layers in Barium Titanate," Phys. Rev., 102[3]:705 (1956).
10. S. Triebwasser, "Space Charge Fields in BaTiO_3 ," Phys. Rev., 118[1]:100 (1960).
11. W.J. Merz, "Switching Time in BaTiO_3 and Its Dependence on Crystal Thickness," J. Appl. Phys., 27:938 (1956).
12. M.E. Drougard and R. Landauer, "On the Dependence of the Switching Time of BaTiO_3 Crystals on Their Thickness," J. Appl. Phys., 30:1663 (1959).
13. E. Fatuzzo and W.J. Merz, "Surface Layer in BaTiO_3 Single Crystals," J. Appl. Phys., 32[9]:1685 (1961).

14. H. Schlosser and M.E. Drougard, "Surface Layers on Barium Titanate Single Crystal Above the Curie Point," J. Appl. Phys., 32[7]:1227 (1961).
15. P. Coufova and H. Arend, Czech. J. Phys., B12:308 (1962).
16. A.V. Turik, "The Problem of the Surface Layer in BaTiO₃ Single Crystals," Sov. Phys. Sol. State, 5:1748 (1964).
17. D.R. Callaby, "Surface Layer of BaTiO₃," J. Appl. Phys., 37:2295 (1966).
18. F.L. English, "Electron-Mirror Microscopy Study of BaTiO₃ Surface Layers," J. Appl. Phys., 39[7]: 3231 (1968).
19. A.K. Goswami, "Dielectric Properties of Unsintered Barium Titanate," J. Appl. Phys., 40[2]:619 (1969).
20. H. Kniepkamp and W. Heywang, "Depolarization Effects in Polycrystalline BaTiO₃," Z. Angew. Phys., 6[9]:385 (1954).
21. G.H. Jonker and W. Noorlander, pp 255-64 in Science of Ceramics, Vol. 1 ed. G.H. Stewart, Academic Press, New York, 1962.
22. L. Egerton and S.E. Koonce, "Effect of Firing Cycle on Structure and Some Dielectric and Piezoelectric Properties of BaTiO₃ Ceramics," J. Amer. Cer. Soc., 38[11]:412 (1955).
23. A.A. Anan'eva, B.V. Strizkov, and M.A. Ugryumov, "Some Anomalous Properties of Chemically-Pure Barium Titanate," Bull. Acad. Sci., USSR, Phys. Ser. 24:1395 (1960).
24. W.R. Buessem, L.E. Cross, and A.K. Goswami, "Phenomenological Theory of High Permittivity in Fine-Grained Barium Titanate," J. Amer. Cer. Soc., 49:33 (1966).
25. A.K. Goswami, "Dielectric Properties of Explosively Compacted BaTiO₃," J. Amer. Cer. Soc., 56:100 (1973).
26. H.C. Graham, N.M. Tallan, and K.S. Mazdiasni, "Electrical Properties of High-Purity Polycrystalline Barium Titanate," J. Amer. Cer. Soc., 54:548 (1971).
27. M.P. Pechini, U.S. Patent # 3,330,697 July 11, 1967.

APPENDIX D

An Investigation of the Low Voltage Failure Mechanism
in Multilayer Ceramic Capacitors

C.J. Brannon and H.U. Anderson

AN INVESTIGATION OF THE LOW VOLTAGE FAILURE MECHANISM
IN MULTILAYER CERAMIC CAPACITORS

C. John Brannon and H. U. Anderson

Abstract

Enhanced leakage current was induced into multilayer ceramic capacitors by the introduction of micro-cracks reaching from the surface through the electrode layers by means of thermal shock and then exposing the capacitors to a low voltage bias and a humid atmosphere. Results indicated that a simple electrolytic solution mechanism may be responsible for the increased conduction and that the proposed dendritic growth mechanisms may be more complex than necessary.

Introduction

In recent years a problem has been identified which concerns the insulation resistance failure of ceramic capacitors which are biased well below their rated voltages. This is a significant problem, and a research effort has focused on determining the cause of low voltage failures as well as developing a testing procedure to effectively detect those capacitors that might be prone to low voltage failures. It is generally recognized among observers of low voltage failure that failure tends to occur only in the presence of moisture and most often in capacitors having such structural defects as voids, delaminations, or cracks extending from the surface through the electrode layers. Low voltage failure does not seem to occur as often in capacitors that are well encapsulated. Another typical characteristic of capacitors exhibiting low voltage failure is the tendency for them to recover, or regain their former high insulation resistance, when the bias is increased to the rated operating level.

The dominant theory of low voltage failure in ceramic capacitors involves the growth of a dendrite of electrode material that connects two electrode layers and thus produces a conduction path creating a short in the capacitor. According to this theory, the electrode material is dissolved in the water that condenses in the present defects which allows the dendrite to grow along the defect connecting two electrode layers.¹⁻⁶ The conducting dendrite grows either by electroconduction or by precipitation. This kind of low voltage failure may be cleared by the application of a

voltage high enough to vaporize the dendrite. The dendrite may also be destroyed by sufficient mechanical vibrations or thermal energies.

Another proposed mechanism of low voltage failure has to do with the aggravated 'aging' of a portion of the dielectric separating the electrodes. Here, crystal-phase transformations occur in the dielectric, causing it to degrade and increase in conductivity.⁷ Again, the application of a high voltage can clear the capacitor. In this case the high voltage produces a heating effect allowing the crystal-phases to retransform to their original states. This 'deaging' effect can also be accomplished by heating the sample.

Other studies⁸⁻¹² have cited a degraded portion of the dielectric as the culprit in failure, with the degradation having possibly been caused by the absorption of water into the dielectric as protons or hydroxyl ions, or possibly by the migration of oxygen vacancies. These failures, however, cannot be cleared by the application of a high voltage, nor are they exclusively low voltage failures. Failures associated with degraded dielectric layers also tend to fail gradually, whereas low-voltage failures typically exhibit an abrupt failure. Also, dielectric layer deterioration can be reversed by either simply removing the applied field or by raising the temperature of the capacitor a few hundred degrees. This suggests a different mechanism at work in low-voltage failure than in dielectric layer degradation.

Screening Tests

Assuming that low voltage failures tend to be related to the presence of water and structural defects, several tests have been developed to detect capacitors that might be prone to low voltage failure. Some methods¹³⁻¹⁶ developed to detect the presence of structural imperfections include ultrasonic scanning,¹⁷ acoustic emission,¹⁸⁻²⁰ vapor condensation,⁸ and methanol testing.⁵⁻⁶ The methanol test is especially useful since it detects cracks that extend from the surface through the electrode layers.

The other method of screening commonly used involves extended life testing. The most commonly used life test is the MIL-C-123 test, also known as the 85°C/85% RH/1.5 VDC test, or 85/85 test for short.^{3-7,9-12} This test has seen extensive usage, and appears capable of detecting lots with failure prone capacitors. There is no real convention, however, on the length of this test.

Experimental Procedure

(1) Initial Examination of Capacitors

The capacitors used in this study were produced by Presidio Components, Inc., San Diego, California. All capacitors were composed of a BaTiO₃ X7R formulation, with electrodes of 100% palladium and end terminations of gold/frit. The electrode layers were buried approximately 3 mils beneath the surface and were separated by a dielectric layers 1.125 mils thick. A cross-sectional view of the capacitor structure is shown as Figure 1.

(2) Initial Examination of Capacitors

To insure their integrity, the entire lot, 128 units, was subjected to the methanol test. The methanol test was performed as follows:

1. 10 VDC was applied to the capacitor and after 15 seconds the leakage current (I_1) was measured.
2. The capacitor was then immersed in methanol for 30 minutes allowing the methanol to penetrate into cracks and open porosity.
3. The capacitor was removed from the methanol and allowed to dry on a tissue to minimize the residual methanol left on the surface.
4. Step 1 was repeated immediately after drying and (I_2) was measured.

A capacitor was considered to fail the methanol test if I_2 was an order of magnitude greater than I_1 . Only 1 capacitor failed the methanol test at this time, and was excluded from the rest of the study.

(3) Introduction of Structural Defects

Structural defects in the form of cracks were introduced into the capacitors. After some unsuccessful attempts using an indentation method, thermal shocking was used for crack introduction. Trial and error experimentation revealed that a temperature gradient of approximately 770 K would introduce cracks extending from the surface of the capacitor through the electrode layers without otherwise damaging the properties of the capacitor. This gradient was achieved by

allowing the capacitors to equilibrate at 850 K (575°C) and then immediately quenching them in liquid nitrogen at 77 K (-196°C). This process produced surface effects, such as crazing, in addition to several deep cracks per capacitor, as illustrated in Figure 2.

A total of 42 specimens were prepared in this way. In order to insure that cracks were indeed introduced into the specimen by the thermal shocking treatment, each specimen was once again subjected to the methanol test.

(4) Variation of Bias Voltage

The capacitors were subjected to a variation of the standard 85/85 test in which the atmosphere was allowed to be either dry or to contain 85% RH, usually in a 4 hours dry, 4 hours wet, and 4 hours dry pattern. Several tests were made with voltages set at 0.5, 1.0, 1.5, 2.0, 5.0, 10.0, 20.0, and 70.0 VDC, producing fields ranging from 0.5 to 70.0 volts/cm.

The purpose of this series of tests was to examine the influence of voltage on failure. In order to produce a data base which could be used for comparison with previous work, a number of trials were made using the standard bias of 1.5 VDC.

Figure 3 shows a schematic circuit diagram for the low voltage capacitor measurement system. The test apparatus used in this portion of the experiment consisted of a Keithley 246 High Voltage Power Supply, a Keithley 619 Electrometer/Voltmeter, a Hewlett Packard 85 computer, and a

furnace in which the atmosphere contained either dry air or air with 85% RH. The electrometer could accomodate 2 specimens at a time, which allowed a test sample to be compared to a standard uncracked specimen for each trial. The entire furnace apparatus was covered by a Faraday cage as a "noise" screen.

(5) Variation in Temperature

The capacitors were once again subjected to a variation of the standard 85/85 test. This series of tests was made using the standard 85/85 test parameters, with the only exception being that the temperature was varied from 85°C to 115°C. The tests were made with the initial atmosphere being dry for the first 4 hours, and then the atmosphere was adjusted to the 85% RH level, which remained for the rest of the test. After 4 hours with the atmosphere at 85% RH, the temperature was raised to 115°C. During this test the voltage level was held constant at 1.5 VDC.

(6) Extended Life Testing

The standard 85/85 test, with 1.5 VDC bias, was applied to 20 capacitors over a period of 20 days. Of these, 15 were thermally cracked samples and 5 were controls. The atmosphere was dry on the first and last days of the run, and was maintained at 85% RH for the remainder of the test.

The apparatus used for the extended life test consisted of a system of 9 seperate furnaces, in each of which the temperature, atmosphere, or voltage could be controlled. A

schematic of this system is given as Figure 4. The system was monitored by a Hewlett Packard HP3054 Data Logger, which is essentially a 100 channel autoranging voltmeter with temperature measuring capabilities. The capacitors were mounted on circuit boards which plugged into connectors which were sealed into the faces of the furnaces.

(7) Sectioning Studies

Capacitors found to exhibit low voltage failure were used in this part of the study. These capacitors were mounted in plastic and were abraided with 500 grit abrasive paper until the cracks were exposed. The mounted capacitors were then polished with 1 micrometer particle size diamond paste. The sectioned capacitors were then examined and photographed using optical and scanning electron microscopy. The energy dispersive X-ray spectrometer of the SEM was used to make both a qualitative and semi-quantitative examination of the crack area in an attempt to detect electrode material and/or other contaminants.

Results

(1) Pattern of Low Voltage Failure

In almost all cases in which low voltage failure occurred, a "sawtooth" pattern of failure was observed. With a dry atmosphere, current density would typically hold steady at approximately 10^{-11} amps/cm.² When 85% RH atmosphere was introduced, the leakage current would typically smoothly rise about 2 orders of magnitude and begin to level off at a

current "plateau" . The leakage current would then abruptly jump anywhere from 1 to 6 orders of magnitude and then smoothly decrease to the "plateau" level. The current level would then abruptly jump again, thus repeating the cycle until the moisture was removed from the atmosphere. The period of this cycle was usually seen to be between 20 and 45 minutes. Figure 5 shows the leakage current in both a shocked and an unshocked specimen with a 1.5 VDC applied bias in a dry atmosphere. As can be seen, the current in the cracked specimen was only slightly higher than that in the uncracked specimen. Figures 6, 7, 8, and 9 show the effects of humidity on the specimens. The effects of the moisture can be observed in Figure 6, in which the current level in the cracked specimen abruptly increases 3 orders of magnitude when moisture was introduced into the atmosphere with the "sawtooth" pattern being initiated, while the current level in the uncracked specimen remained essentially unchanged. Figure 7 illustrates the "sawtooth" behavior of a cracked specimen, with the current level rising over 6 orders of magnitude at the peak. Figures 8 and 9 illustrate the extent of the effect of the humid atmosphere on low voltage breakdown. In both of these figures periodic breakdown was seen to begin to occur immediately after moisture was introduced into the furnace atmosphere. When the moisture was removed from the atmosphere, periodic breakdown was discontinued and the leakage current quickly returned to its original level.

(2) Variations in Voltage Bias

Low voltage failure was found to be dependent upon the voltage level on the capacitor. Figure 10 illustrates the behavior of the specimen when a bias of 0.5 volts was introduced. No difference was observed between the leakage current of the cracked and the reference, uncracked specimen with changes in moisture. However, as can be seen in figure 11, at a bias of 1.0 volts, when moisture was introduced the same specimen exhibited failure with the same "sawtooth" behavior as previously observed. This low voltage failure pattern was also seen at biases of 1.5 and 2.0 volts in figures 12 and 13, respectively. Figures 14, 15, and 16 show that at biases of 5.0, 10.0, and 20.0 volts the "sawtooth" failure pattern also occurred, but here it can be seen that as the voltage level was increased, the period of the pattern lengthens and the difference in current magnitude between the reference and cracked capacitors decreased. When a bias of 70 volts was applied across the capacitors, a single spike was seen to occur when the moisture was first introduced after which the leakage current steadily decreased until it almost matched that of the reference capacitor. This effect is seen in figure 17.

(3) Extended Life Testing

Of the 15 cracked samples tested, 10 showed the characteristic "sawtooth" pattern in the presence of a humid atmosphere. The remaining 5 showed marked increases in the leakage current, but showed no discernable pattern to their

low voltage failures. The 5 reference units showed no change in the presence of a humid atmosphere. When the humidity was removed from the atmosphere, all 15 failing samples showed a slow decrease of the leakage currents until they matched the reference capacitors. Graphs typical of the life tests can be seen in figures 18-21. Figure 18 and 19 show the abrupt jump in leakage current when 85% RH was suddenly added to the atmosphere. The resulting leakage currents were cyclic, exhibiting the characteristic "sawtooth" pattern. Figures 20 and 21 show the leakage current over a 14 hour period during the 10th day of the life test. The specimens had been exposed to the humid atmosphere for 9 days and continued to exhibit the "sawtooth" leakage pattern. The pattern shown in figure 21 shows a breakdown pattern that is more regular and defined than the usual "sawtooth" associated with the low-voltage failures seen in this study. This suggests that low-voltage failure actually becomes more pronounced with time, instead of eventually "clearing" itself.

(4) Thermal Studies

The results of the thermal variation studies are seen in figure 22. In this series of tests the temperature was manipulated as the independent variable, achieving almost identical results. The leakage current was low in the dry 85°C atmosphere, and increased dramatically when the humidity was raised. When, with the humidity still at 85%, the temperature was raised to 115°C, the leakage current returned to its original, lower level and the "sawtooth" pattern could

no longer be observed. This supports the idea that water which condenses into the cracks in the capacitor plays the dominant role in low-voltage breakdown.

(5) Sectioning Studies

Optical microscopy showed visible cracks extending from the surface of the capacitors through the electrode layers. Sections were made parallel and perpendicular to the electrodes to give views of the cracks from several different perspectives. Figures 23 and 24 show photomicrographs of exposed cracks in two specimens. Figure 23 shows a section taken parallel to the electrode layers with the crack penetrating both partially exposed electrode layers. Figure 24 shows two cracks penetrating the electrode layers in a section taken perpendicular to the electrode layers. Cracks located optically were then examined with the SEM energy dispersion X-ray spectrometer for detailed study. Figure 25 was taken with the SEM and shows a close-up view of one of the cracks seen in Figure 24. No difference was found between the composition of the crack walls and the base dielectric material. In only one sample was an excess of the Pd electrode material found in the region of the crack, but the Pd was also found to be present at the same high levels throughout the rest of the dielectric. No traces of dendrites were found either optically, with the SEM, or with the energy dispersion X-ray spectrometer.

Energy dispersion X-ray spectrometry was also used in an attempt to find any possibly contaminants in the region of

the crack. The only contaminants found were traces of Nb in one sample. Of course, it is likely that any water soluble contaminants were removed during polishing by the diamond paste, which is itself water-based.

Discussion and Conclusions

The leakage current induced in the capacitors of this study exhibits the "classical" low voltage failure characteristics, i.e. the presence of structural defects in the capacitors and the ability of high voltages to "clear" shorts in the capacitors. The "sawtooth" pattern of failure is peculiar to this study, although this behavior has been seen in porous disc capacitors exposed to similar biases and humid atmospheres.²¹

The "sawtooth" behavior and the absence of excess electrode material being found anywhere in the cracks suggests that the growth of dendrites between the electrodes was not the failure mechanism at work in this case. If dendrites did form, due to the low solubility of Pd in water it is likely that they would be composed of a salt of Pd such as PdCl_2 . No evidence of PdCl_2 or any other salt was found. The fact that breakdown ceased to occur almost immediately after the moisture was removed from the atmosphere also suggests that dendrites could not be responsible. Even if dendrites require water to grow in the defects, once grown they should continue to exist after the removal of the moisture and continue to facilitate breakdown. But this is

not the case, since in all instances breakdown rapidly ceases when water is removed from the system.

The data of this study can be understood if electrolytic ionic conduction is assumed to cause the enhanced leakage current. If electrolytic impurities such as chlorine or bromine salts were present in the sample, conduction between the electrode layers could have occurred by means of ionic transport. Any soluble impurity ions could conceivably take part in such conduction. Water undergoes dissociation to H^+ and OH^- at 0.87 volts, so that above this voltage H^+ and OH^- ions could contribute to the leakage current. The fact that the onset of the "sawtooth" pattern and enhanced leakage was located between 0.5 and 1.0 VDC tends to support this mechanism. At higher voltages the increased currents could generate enough localized heat to facilitate the evaporation of the aqueous conductor. This could also account for the "sawtooth effect" with the rapid rise in current producing enough heat to effectively halt itself.

Electrolytic conduction is a much simpler breakdown mechanism than dendritic growth, and does not require as narrow a range of conditions in order to take place. Furthermore, conditions postulated to be necessary for dendritic growth, such as the presence of moisture in existing defects and the presence of Cl ions, are ideally suited for the facilitation of an electrolytic solution as the conduction mechanism.

References

1. Sato, K. et.al., "A Low-Voltage Screening of Ceramic Capacitors From Leakage Failures", Proceedings of the International Symposium for Testing and Failure Analysis, 1981.
2. Sato, K. et.al., "Mechanism of Ceramic Capacitor Leakage Failure Due to Low DC Stress", Proceedings of the 18th International Reliability Physics Symposium, 1980.
3. Ropiak, S., "Low Voltage Failure Mechanisms for Ceramic Capacitors", Proceedings of the International Society for Testing and Failure Analysis Symposium, Los Angeles, 1982.
4. Murata et.al., "Low-Voltage Failure of Monolithic Ceramic Capacitors and Their Screening Method", Proceedings of the International Symposium for Testing and Failure Analysis, 1981.
5. Chittick, R.C. Gray, E. and Alexander, J.H., "Non-Destructive Screening for Low-Voltage Failure in Multilayer Capacitors", Proceedings of the 3rd Annual Capacitor and Resistor Technology Symposium, March 1983.
6. Chittick, R.C. and Gray, E., "Improved Moisture Resistance of Multilayer Ceramic Capacitors Encapsulated by On-Line Screening", Proceedings of the 4th Annual Capacitor and Resistor Technology Symposium, March 1984.
7. Holladay, A.M., "Unstable Insulation Resistance in Ceramic Capacitors", Proceedings of the Symposium on Capacitor Technology, Applications, and Reliability, NASA Conf. Pub. 2186, 1981.

8. Herbert, J.M. Ceramic Dielectrics and Capacitors. Gordon and Breach Science Publications, 1985.
9. Ewell, G.J. and Demeo, D.A., "Electrical Parameters of Capacitors Failing the 85°C/ 85% RH/ 1.5 VDC Test", Proceedings of the 2nd Annual Capacitor and Resistor Technology Symposium, March 1982.
10. Ewell, G.J. and Demeo, D.A., "Extended Electrical Characteristics of Ceramic Capacitor Failure Under Low-Voltage Conditions", Proceedings of the International Symposium for Testing and Failure Analysis, October 1982.
11. Hughes Aircraft Co., "A Study of Unstable Insulation Resistance in Multilayer Ceramic Capacitors", Final Report on NASA Contract NAS8-34364, October 1982.
12. Streassle, R.C. and Ewell, G.J., "The 85°C-85% R.H.-1.5 VDC Bias Test: Can Ceramic Capacitors Pass This New Screen?", Proceedings of the 3rd Annual Capacitor and Resistor Technology Symposium, March 1983.
13. DerMarderosian, A., "The Detection of Cracks in Ceramic Packages by Vapor Condensation", IEEE, 1980.
14. Capitano, J.L., "Innovative Screening for Ceramic Capacitors to Remove Failure Mechanisms", Gould Inc., NavCom Systems Division, 1981.
15. Kiernan, G.F., "A Comparison of Screening Techniques for Ceramic Capacitors", Sperry Support Services, 1982.
16. Love, G.R., "Non-Destructive Testing of Monolithic Ceramic Capacitors", ISHM 1973 Hybrid Microelectronics Conference, Union Carbide Corporation, Technical Paper Reprint.

17. Bradley, F.N., "Ultrasonic Scanning of Multilayer Ceramic Chip Capacitors", Proceedings of the Symposium on Ceramic Technology, Applications, and Reliability, NASA Conf. Pub. 2186, 1981.
18. Vahaviolos, S.J., "In-Process Capacitor Flaw Determination with Acoustic Emission", Phys. Acoust. Corp. Tech. Report TR-19, 1979.
19. Kahn, S.R., and Checkaneck, R.W., "Acoustic Emission Testing of Multilayer Ceramic Capacitors", IEEE Transactions on Components, Hybrids, and Manufacturing Technology, Volume Chmt-1, 1978.
20. Vorres, C.L. et.al., "Re-evaluation of Ceramic Capacitors with the Scanning Laser Acoustic Microscope", Proceedings of the 3rd Annual Capacitor and Resistor Technology Symposium, March 1983
21. Huebner, W., Unpublished Research Conducted at the University of Missouri-Rolla, 1983.

List of Figures

Figure

1. Cross-section of a typical capacitor as supplied by Presidio, Inc.
2. Sketched cross-section of a typical capacitor after having undergone thermal shocking.
3. Schematic of the 2-unit testing apparatus.
4. Schematic of the life-testing apparatus.
5. Plot of the logarithm of the leakage current density vs. time in seconds for both a cracked and an uncracked capacitor at 85°C and 1.5 VDC in a dry atmosphere.
6. Plot of the logarithm of the leakage current density vs. time in seconds for both a cracked and an uncracked capacitor undergoing the 85/85 2.0 VDC test with varying atmosphere.
7. Plot of the logarithm of the leakage current density vs. time in seconds for a cracked capacitor undergoing the 85/85 2.0 VDC test with varying atmosphere.
8. Plot of the logarithm of the leakage current density vs. time in seconds for a cracked capacitor undergoing the 85/85 1.5 VDC test with varying atmosphere.
9. Plot of the logarithm of the leakage current density vs. time in seconds for a cracked capacitor undergoing the 85/85 1.5 VDC test with varying atmosphere.
10. Plot of the logarithm of the leakage current density vs. time in seconds for a cracked capacitor undergoing the 85/85 0.5 VDC test with varying atmosphere.

11. Plot of the logarithm of the leakage current density vs. time in seconds for a cracked capacitor undergoing the 85/85 1.0 VDC test with varying atmosphere.
12. Plot of the logarithm of the leakage current density vs. time in seconds for a cracked capacitor undergoing the 85/85 1.5 VDC test with varying atmosphere.
13. Plot of the logarithm of the leakage current density vs. time in seconds for a cracked capacitor undergoing the 85/85 2.0 VDC test with varying atmosphere.
14. Plot of the logarithm of the leakage current density vs. time in seconds for a cracked capacitor undergoing the 85/85 5.0 VDC test with varying atmosphere.
15. Plot of the logarithm of the leakage current density vs. time in seconds for a cracked capacitor undergoing the 85/85 10.0 VDC test with varying atmosphere.
16. Plot of the logarithm of the leakage current density vs. time in seconds for a cracked capacitor undergoing the 85/85 20.0 VDC test with varying atmosphere.
17. Plot of the logarithm of the leakage current density vs. time in seconds for a cracked capacitor undergoing the 85/85 70.0 VDC test with varying atmosphere.
18. Plot of the logarithm of the leakage current density vs. time in seconds for a cracked capacitor undergoing the 85/85 1.5 VDC test with varying atmosphere (exerpt from the life tests).

19. Plot of the logarithm of the leakage current density vs. time in seconds for a cracked capacitor undergoing the 85/85 1.5 VDC test with varying atmosphere (exerpt from the life tests).
20. Plot of the logarithm of the leakage current density vs. time in seconds for a cracked capacitor undergoing the 85/85 1.5 VDC test with humid atmosphere (exerpt from the life tests).
21. Plot of the logarithm of the leakage current density vs. time in seconds for a cracked capacitor undergoing the 85/85 1.5 VDC test with humid atmosphere (exerpt from the life tests).
22. Plot of the logarithm of the leakeag current density vs. time in seconds for a cracked capacitor subjected to a 1.5 VDC bias with varying atmosphere and temperature.
23. Photomicrograph of 2 cracks penetrating the surface and electrode layers of a thermally shocked capacitor that exhibited low-voltage breakdown.
24. Photomicrograph of 2 cracks penetrating the surface and electrode layers of a thermally shocked capacitor that exhibited low-voltage breakdown.
25. Photomicrograph of a crack taken using the SEM.

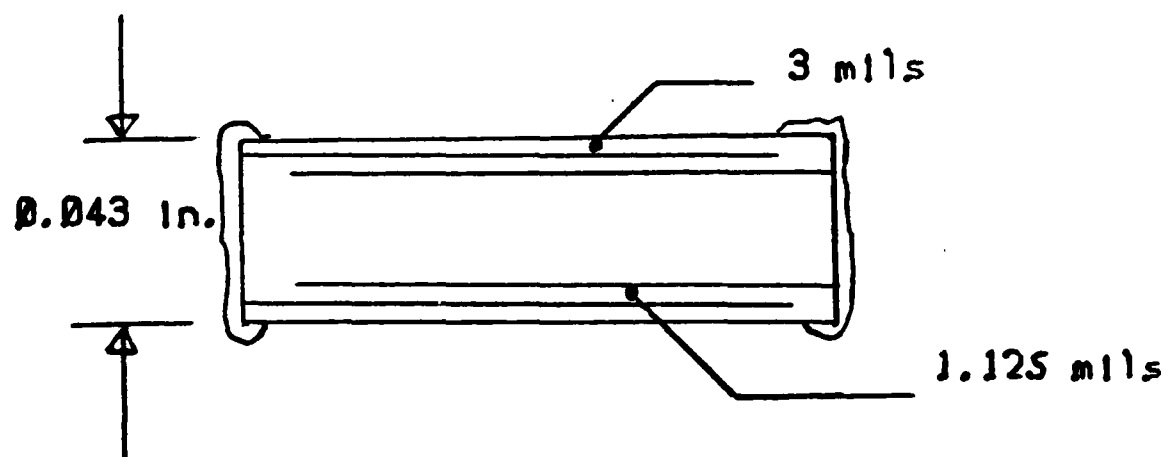


FIGURE 1

CAPACITOR AFTER THERMAL SHOCKING

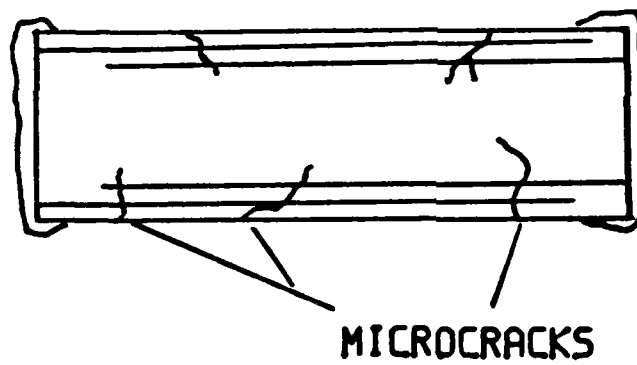


FIGURE 2

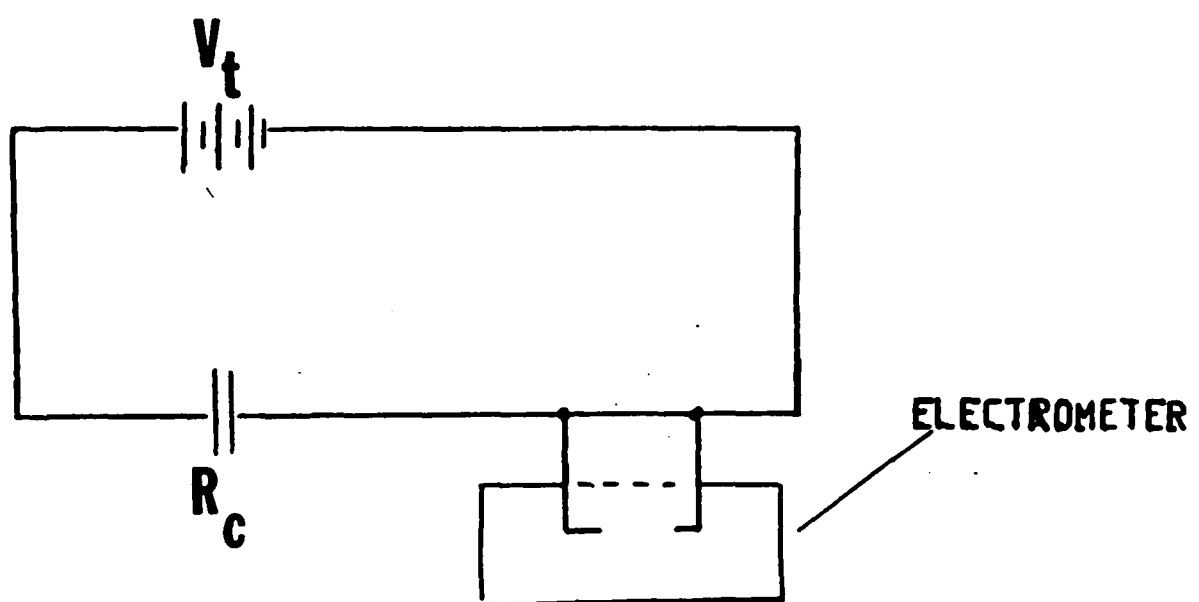
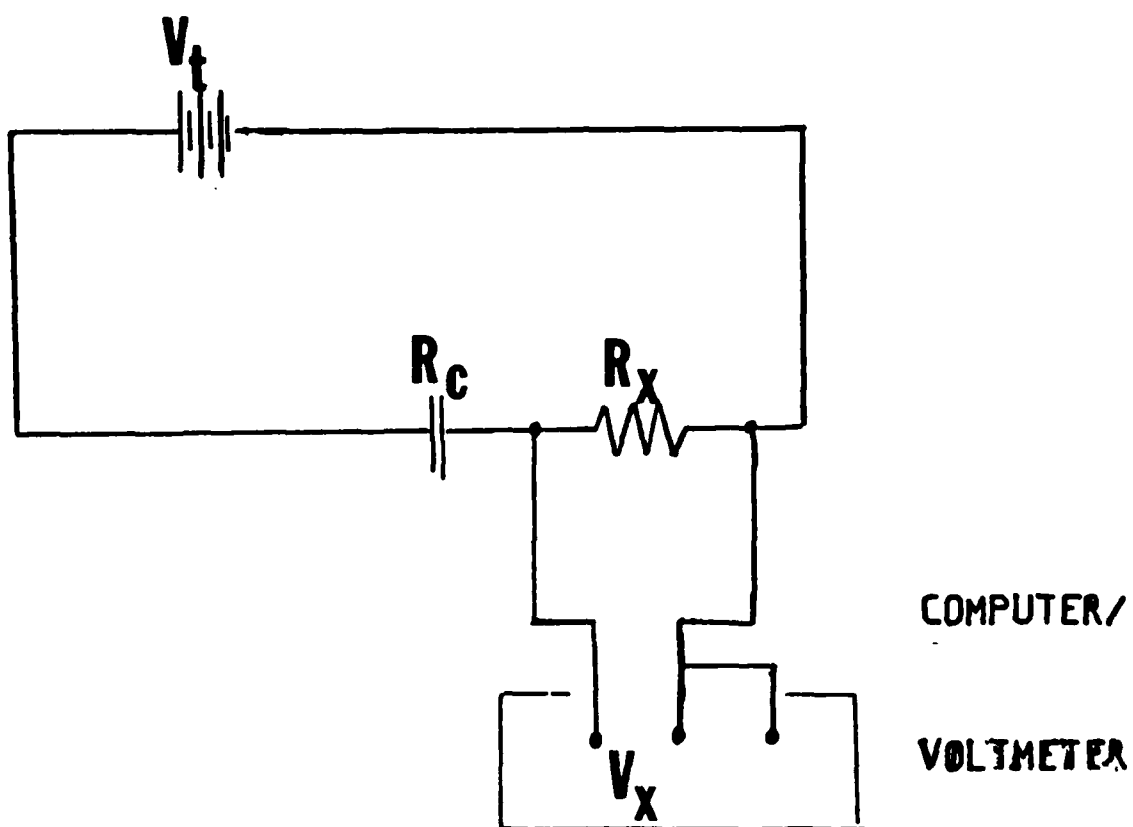


FIGURE 3



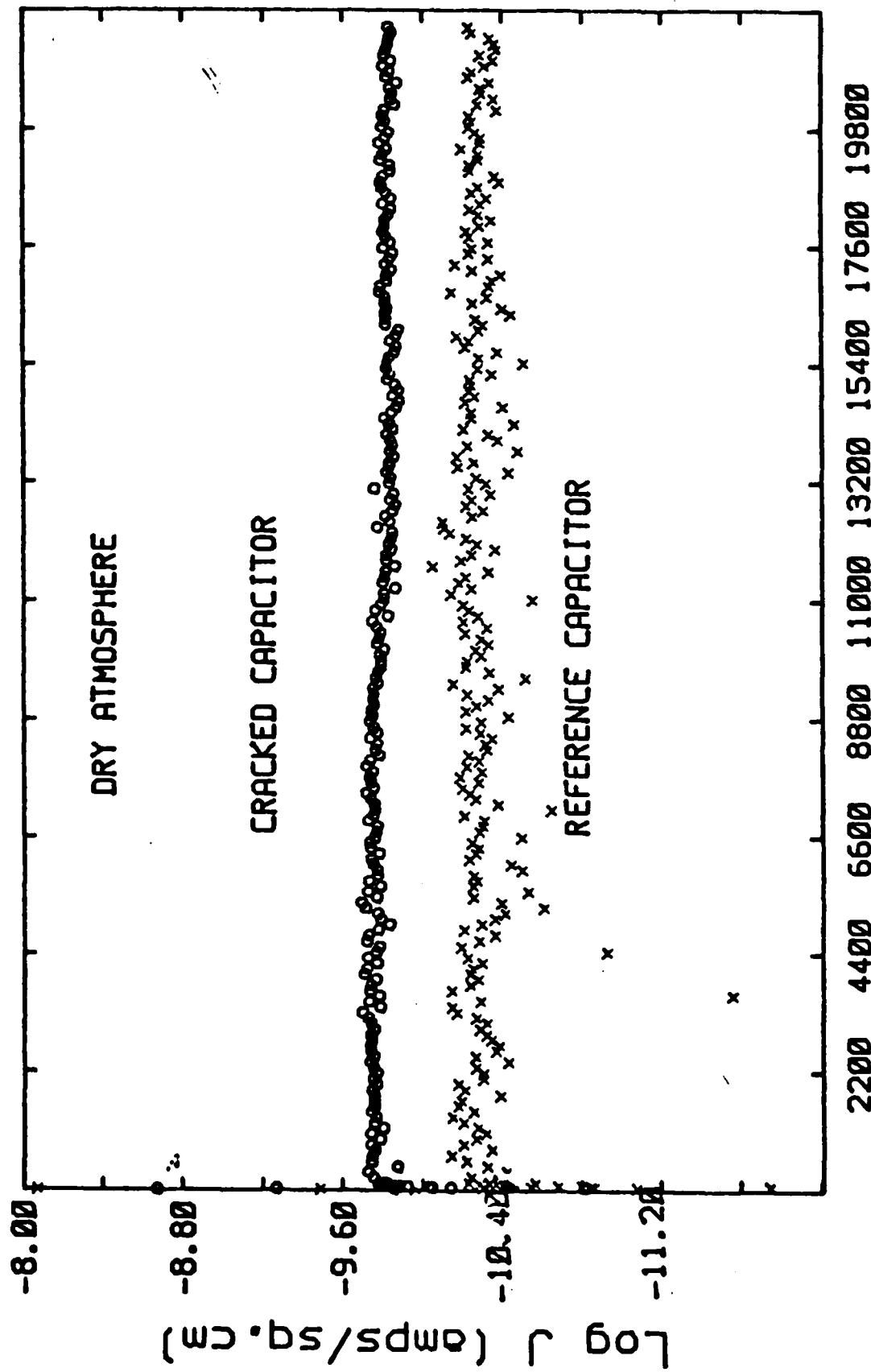
VOLTAGE READ:

$$V_x = V_t \frac{R_x}{R_c + R_x}$$

LEAKAGE CURRENT:

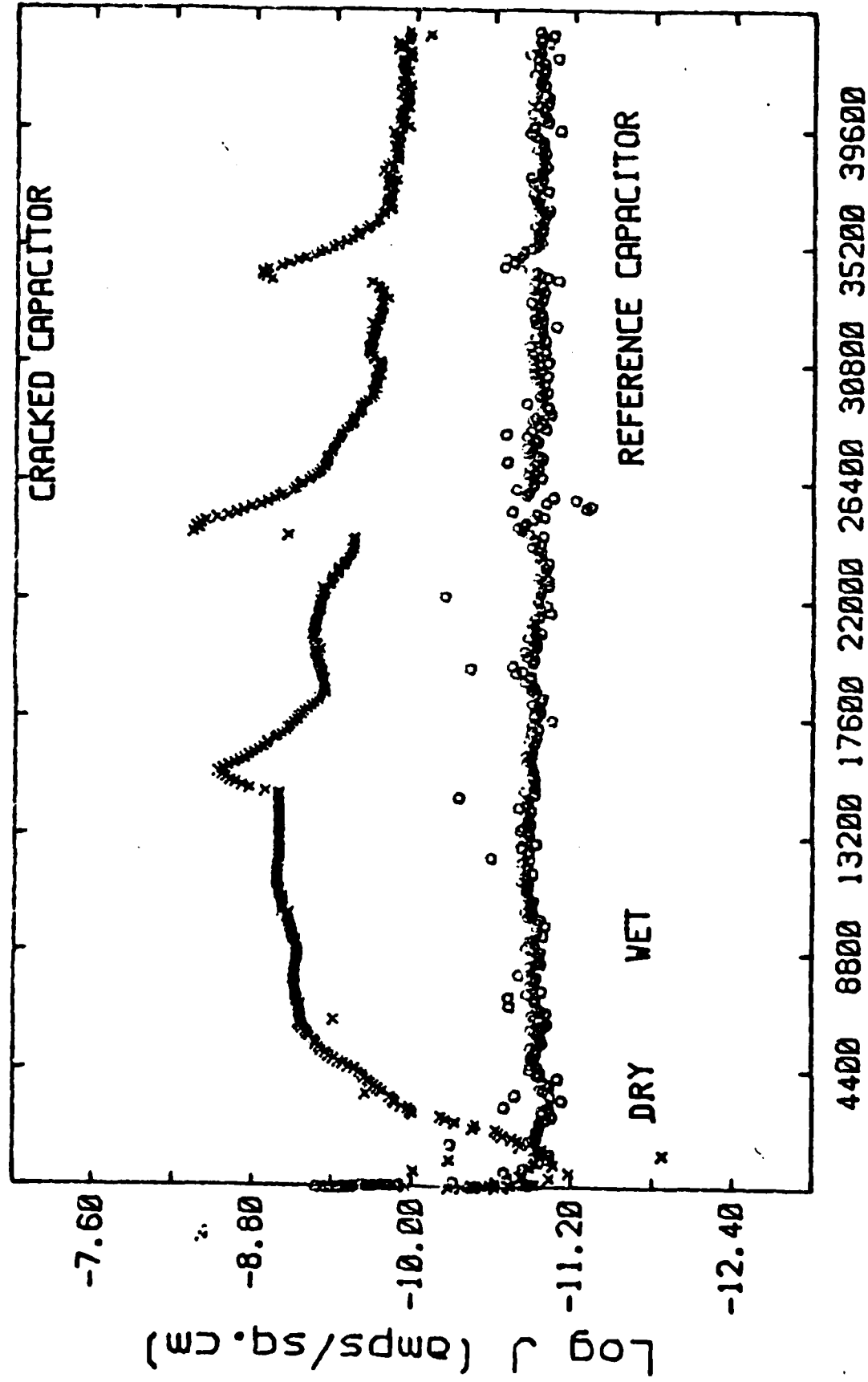
$$I_c = \frac{V_x}{R_x}$$

FIGURE 4



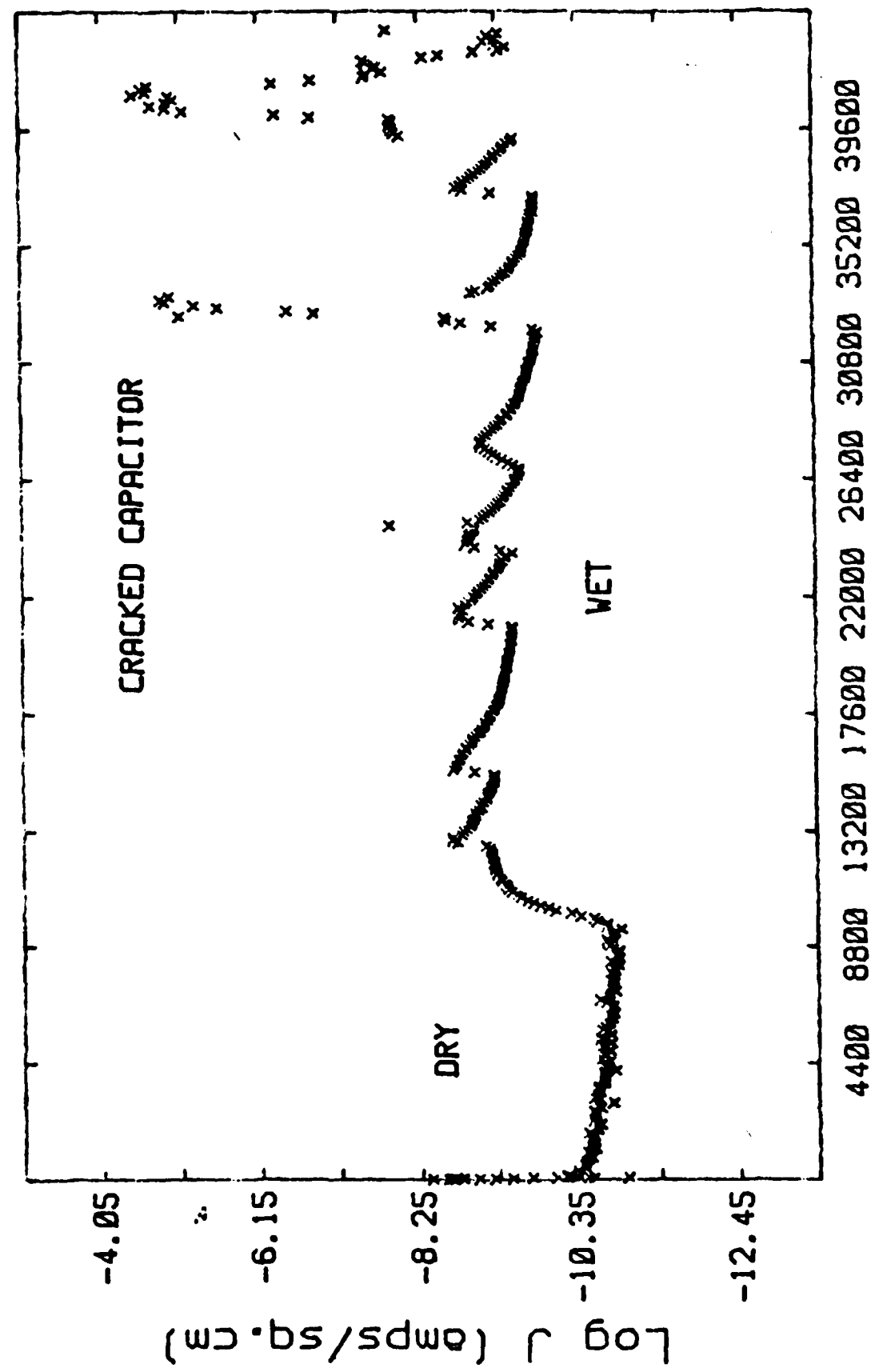
TIME (seconds)

FIGURE 5



TIME (seconds)

FIGURE 6



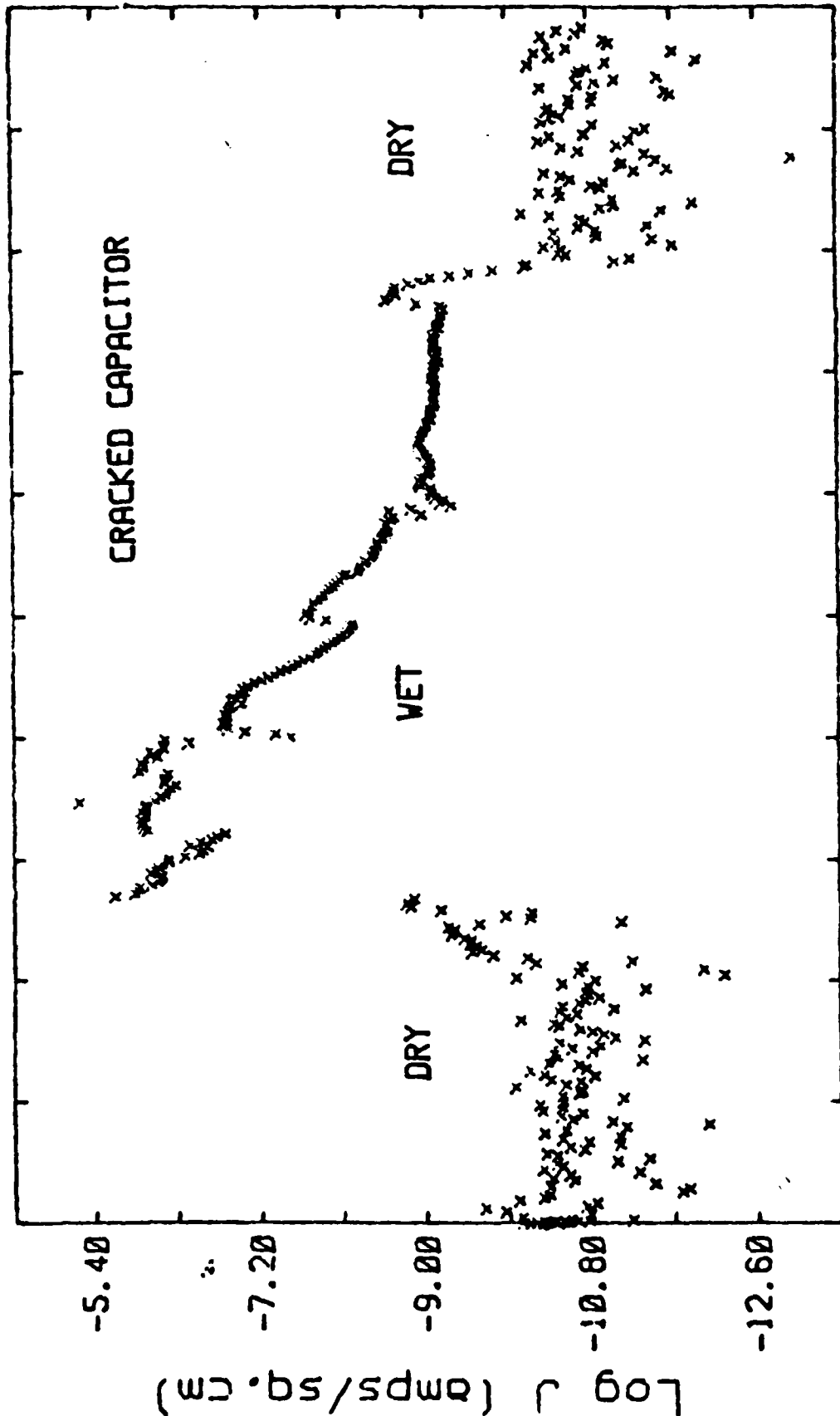


FIGURE 8

1.3 VDC

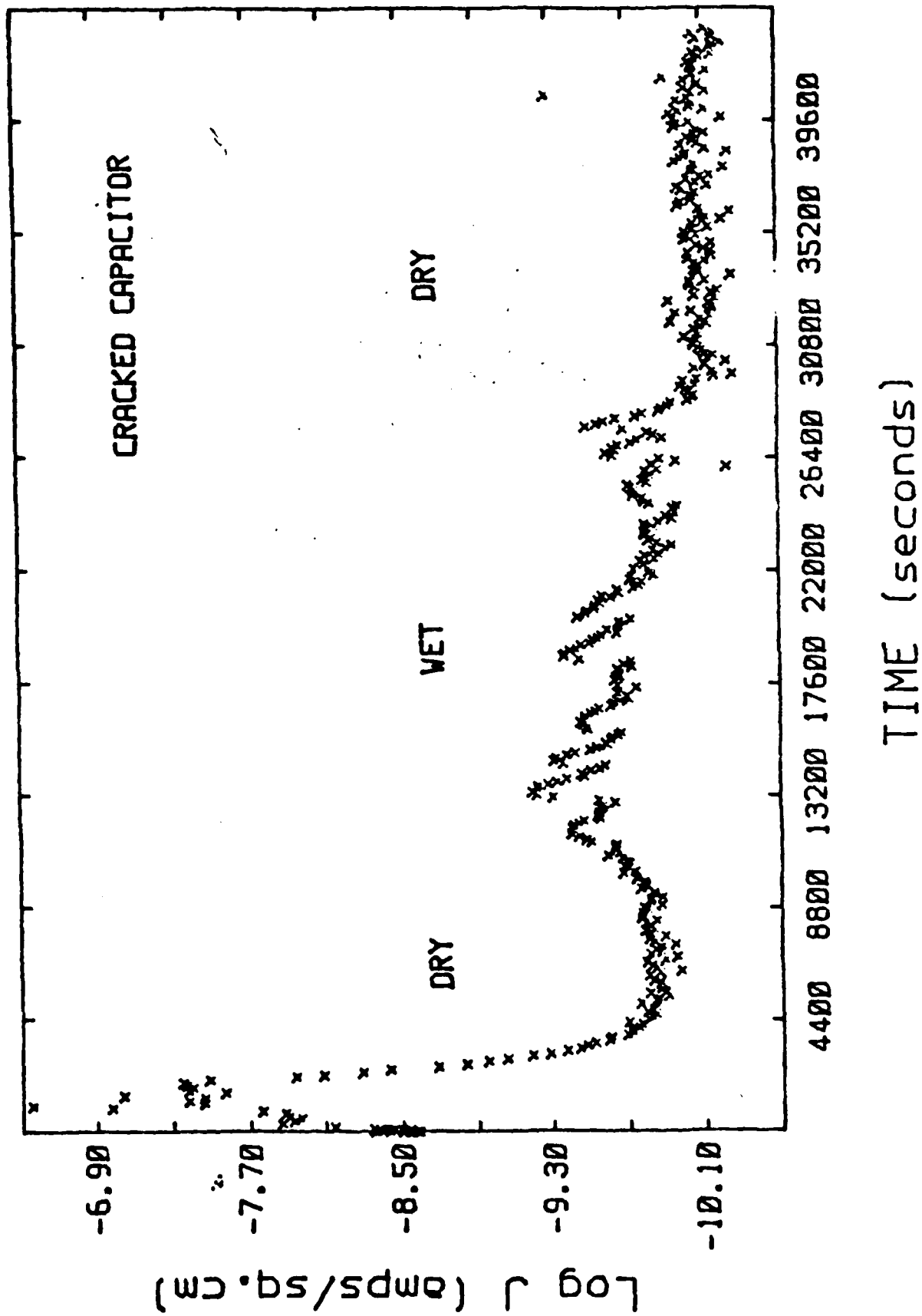


FIGURE 9

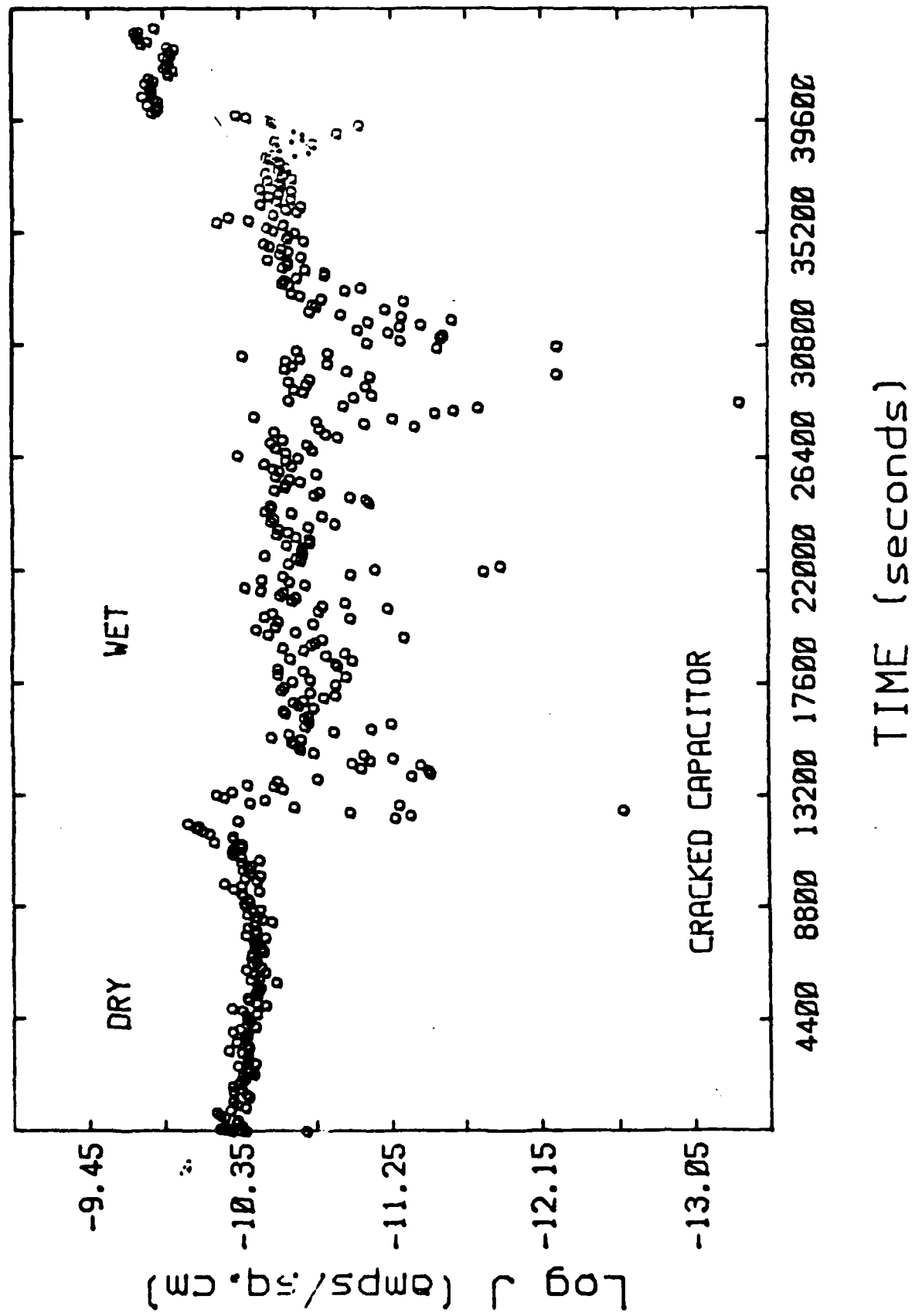
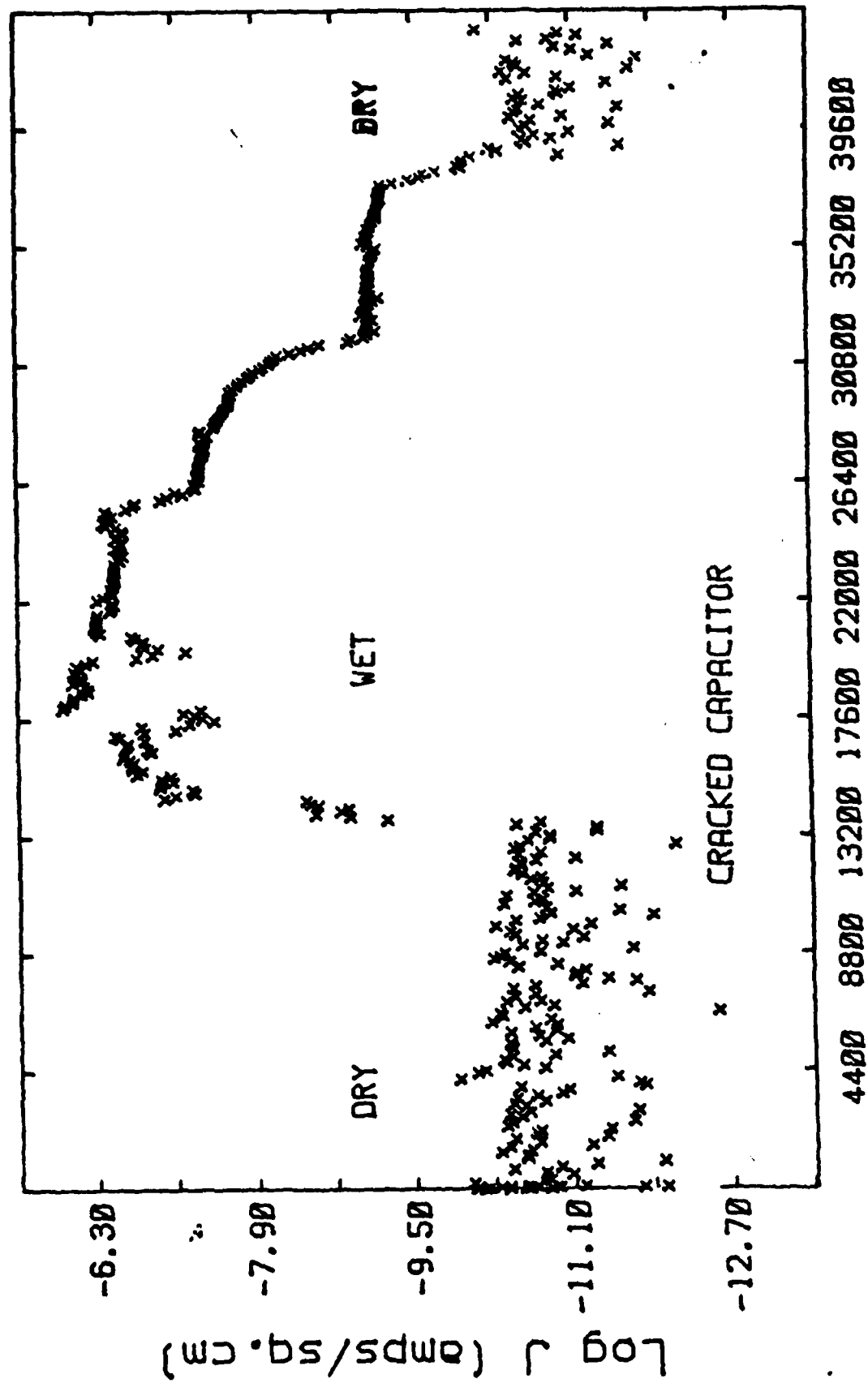


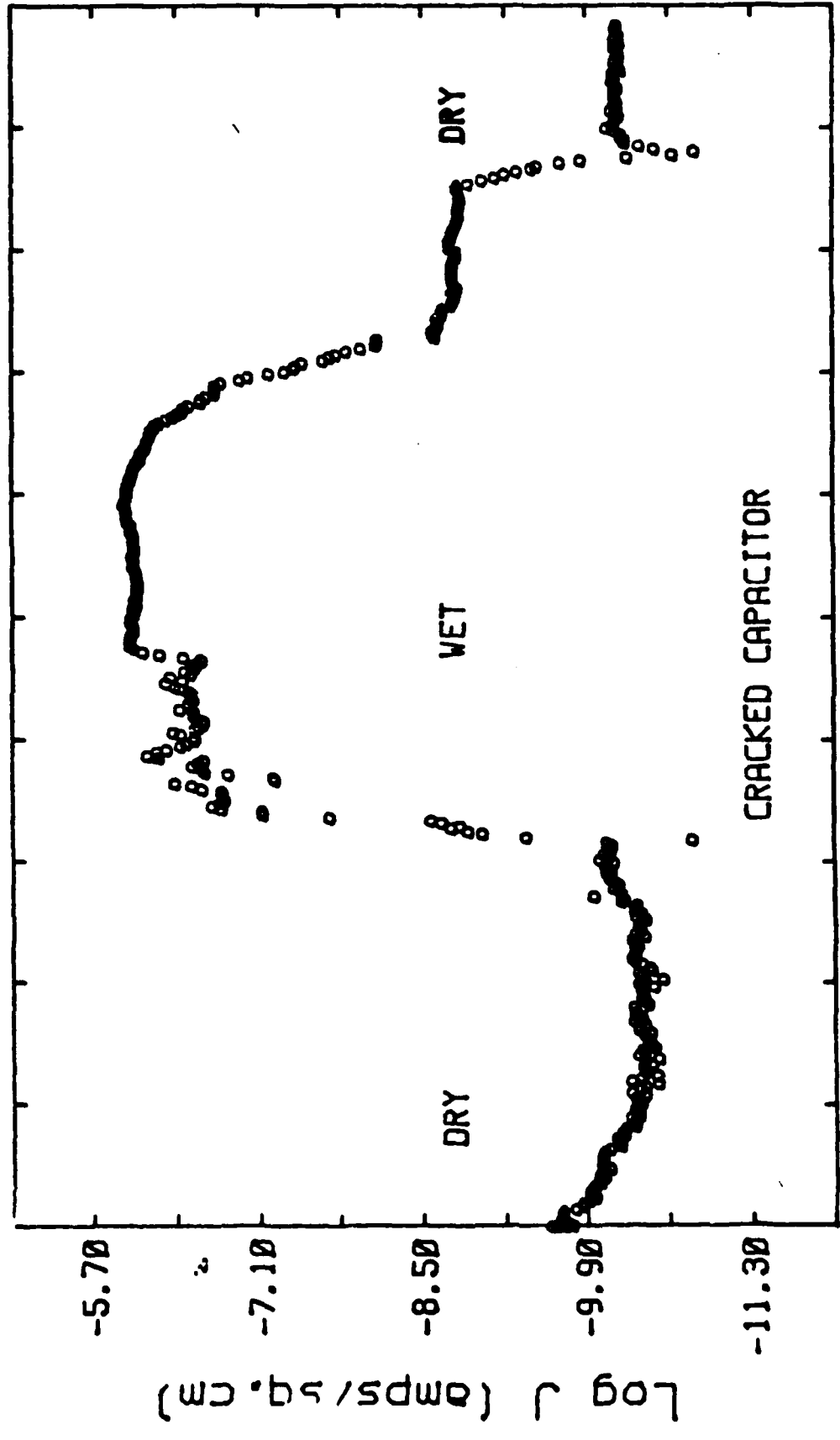
FIGURE 10



TIME (seconds)

FIGURE 11

1.5 VDC



4400 8800 13200 17600 22000 26400 30800 35200 39600

TIME (seconds)

FIGURE 12

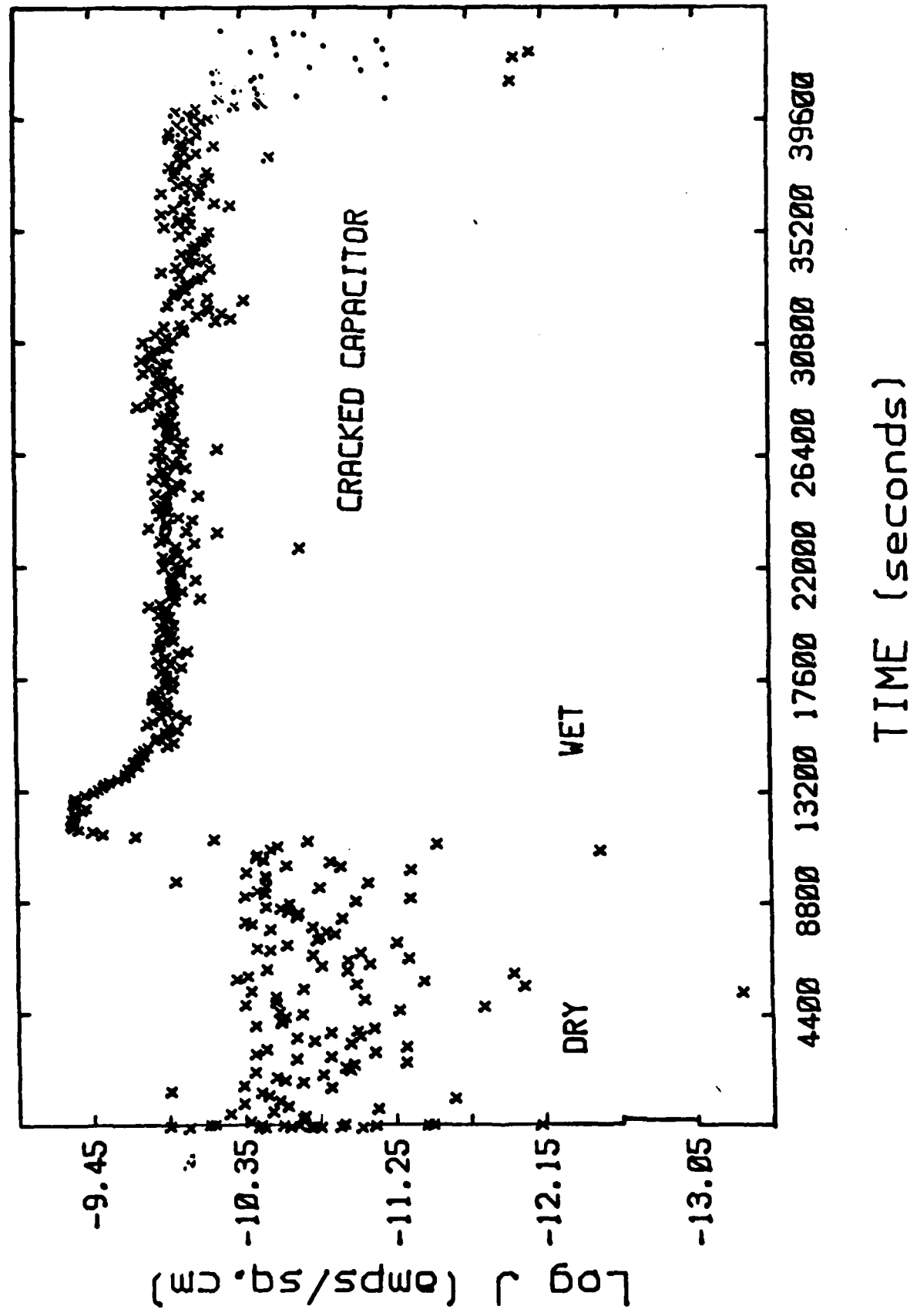


FIGURE 13

10 20 30 40 50 60 70 80 90 100 110 120 130 140 150 160 170 180 190 200 210 220 230 240 250 260 270 280 290 300 310 320 330 340 350 360 370 380 390 400 410 420 430 440 450 460 470 480 490 500 510 520 530 540 550 560 570 580 590 600 610 620 630 640 650 660 670 680 690 700 710 720 730 740 750 760 770 780 790 800 810 820 830 840 850 860 870 880 890 900 910 920 930 940 950 960 970 980 990 1000

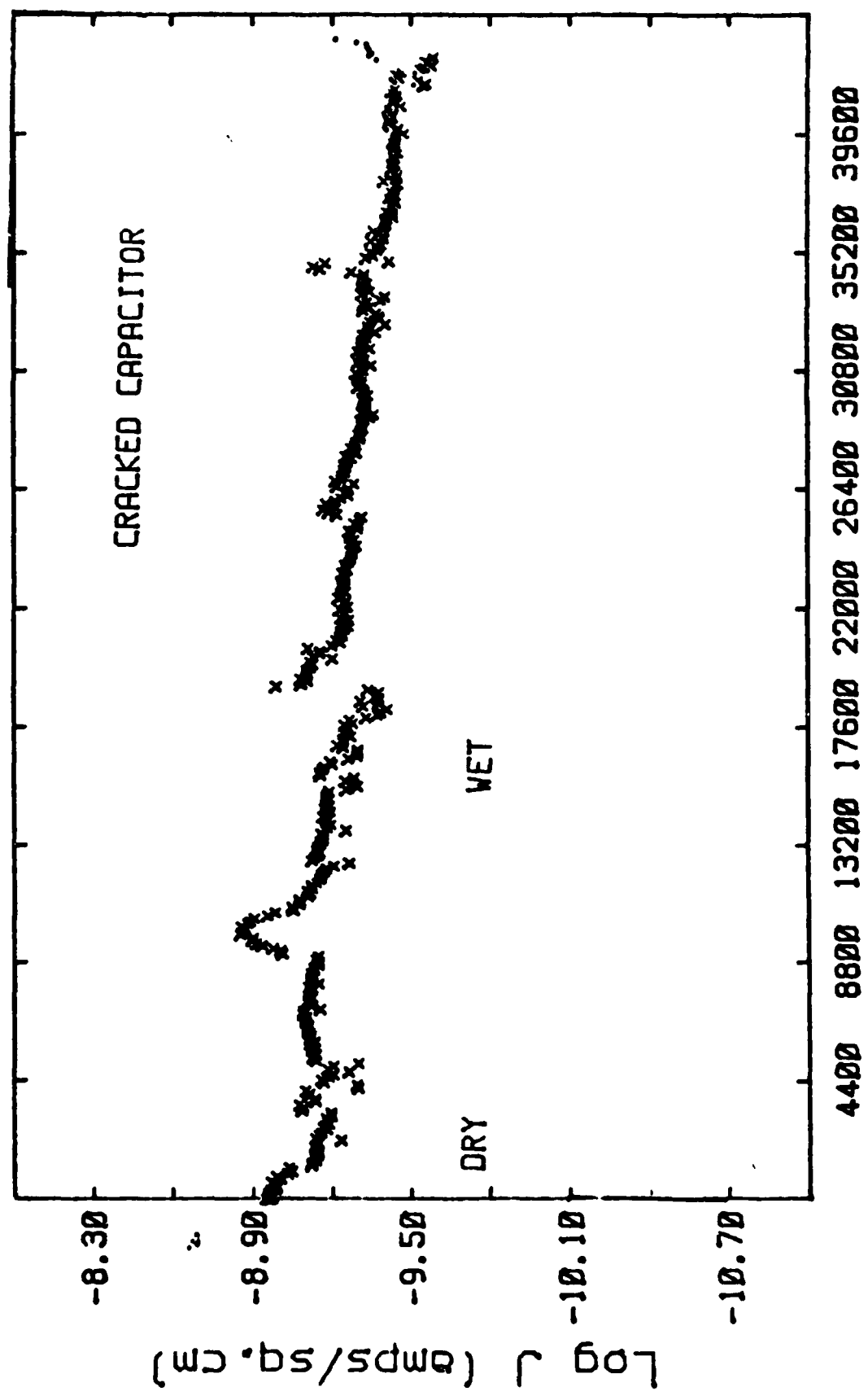
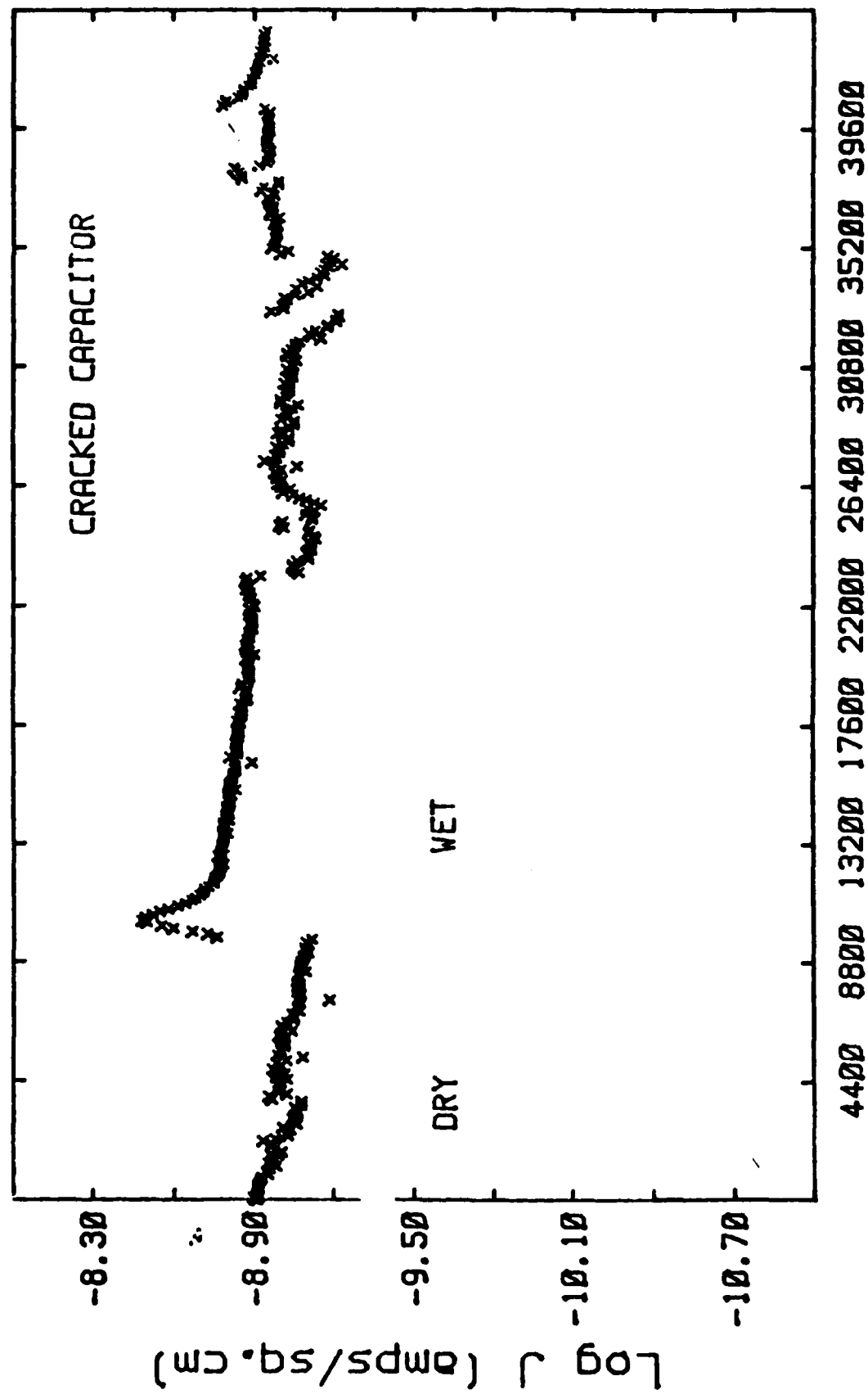


FIGURE 14



TIME (seconds)

FIGURE 15

20 VDC

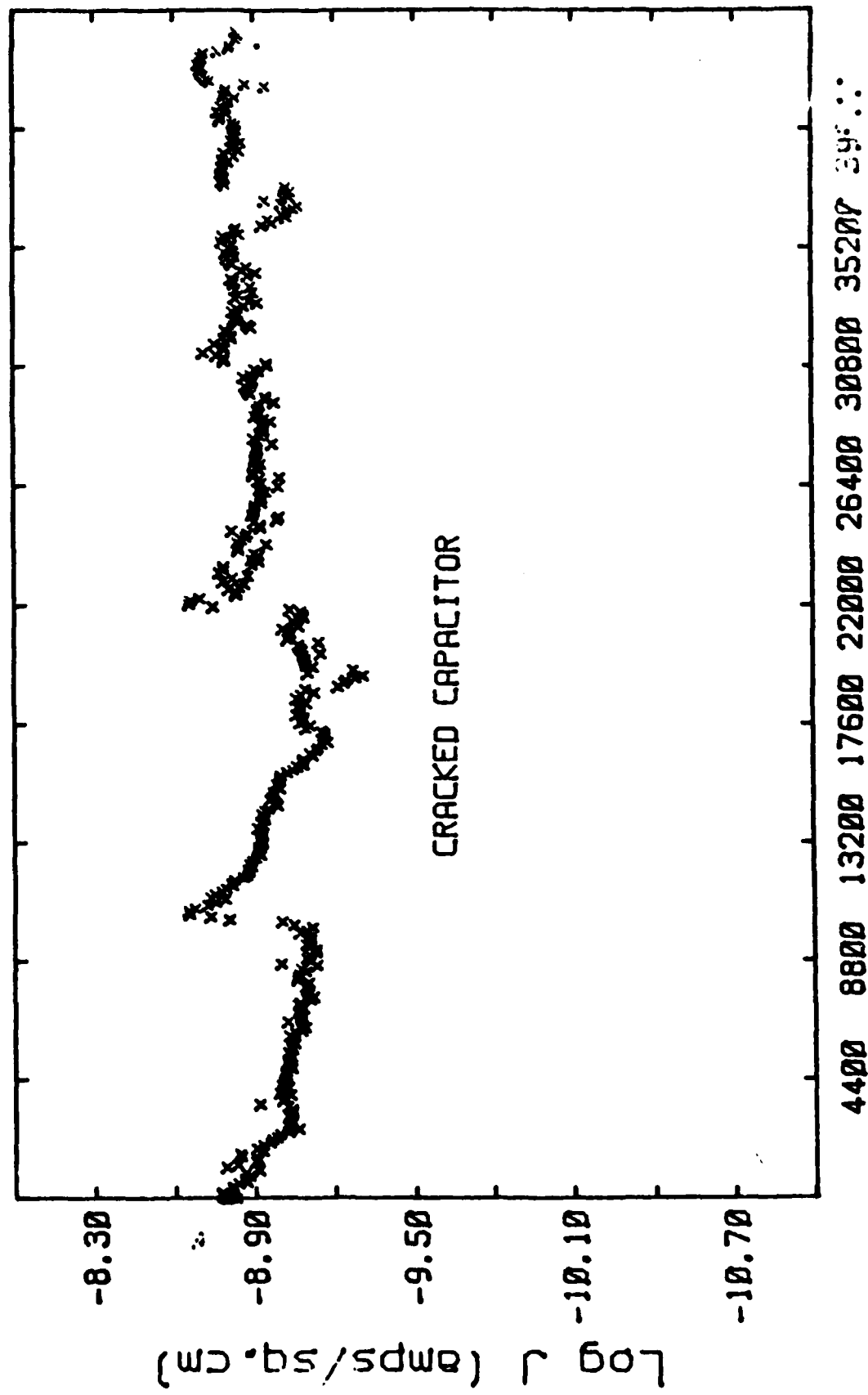


FIGURE 16

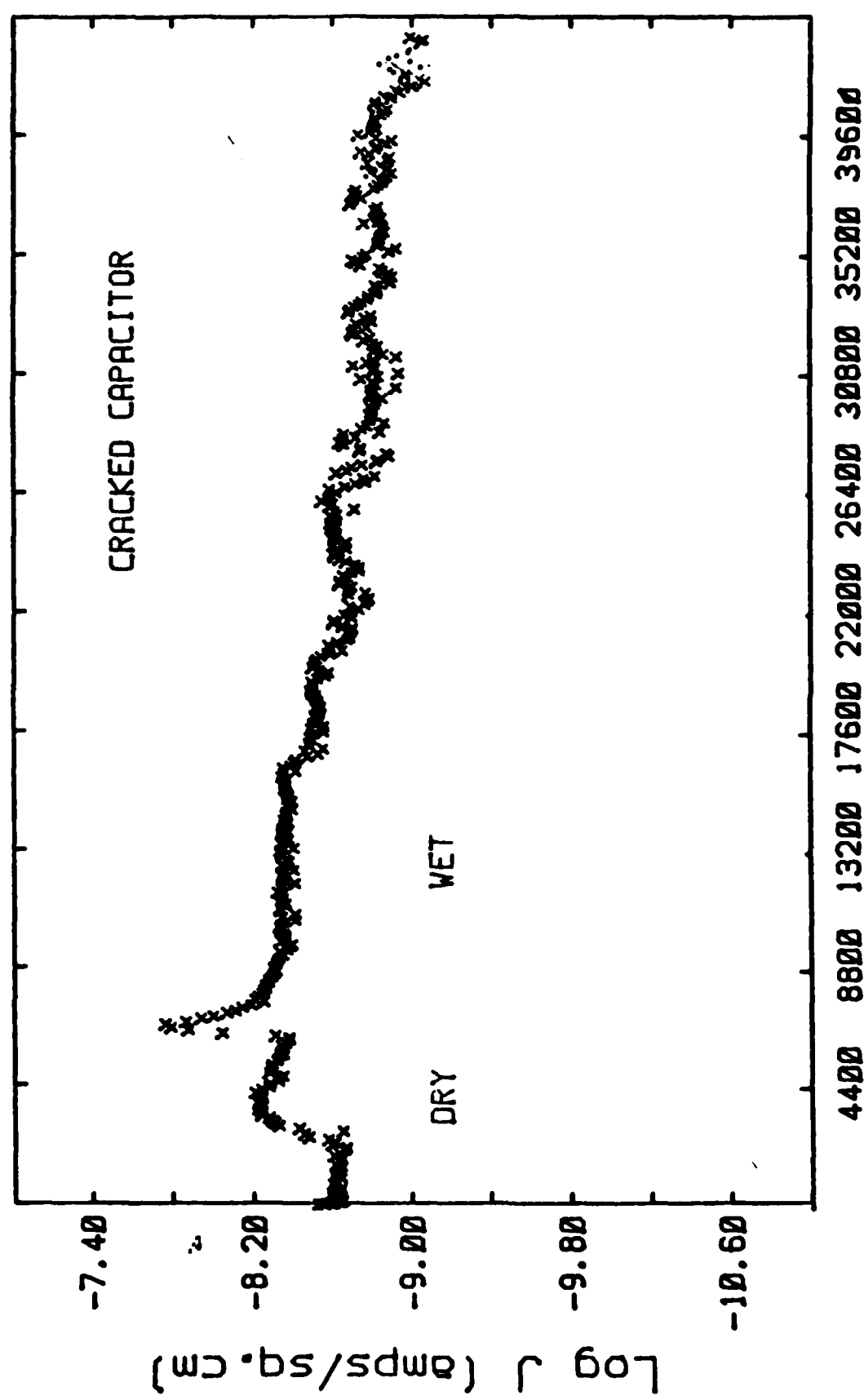


FIGURE 17

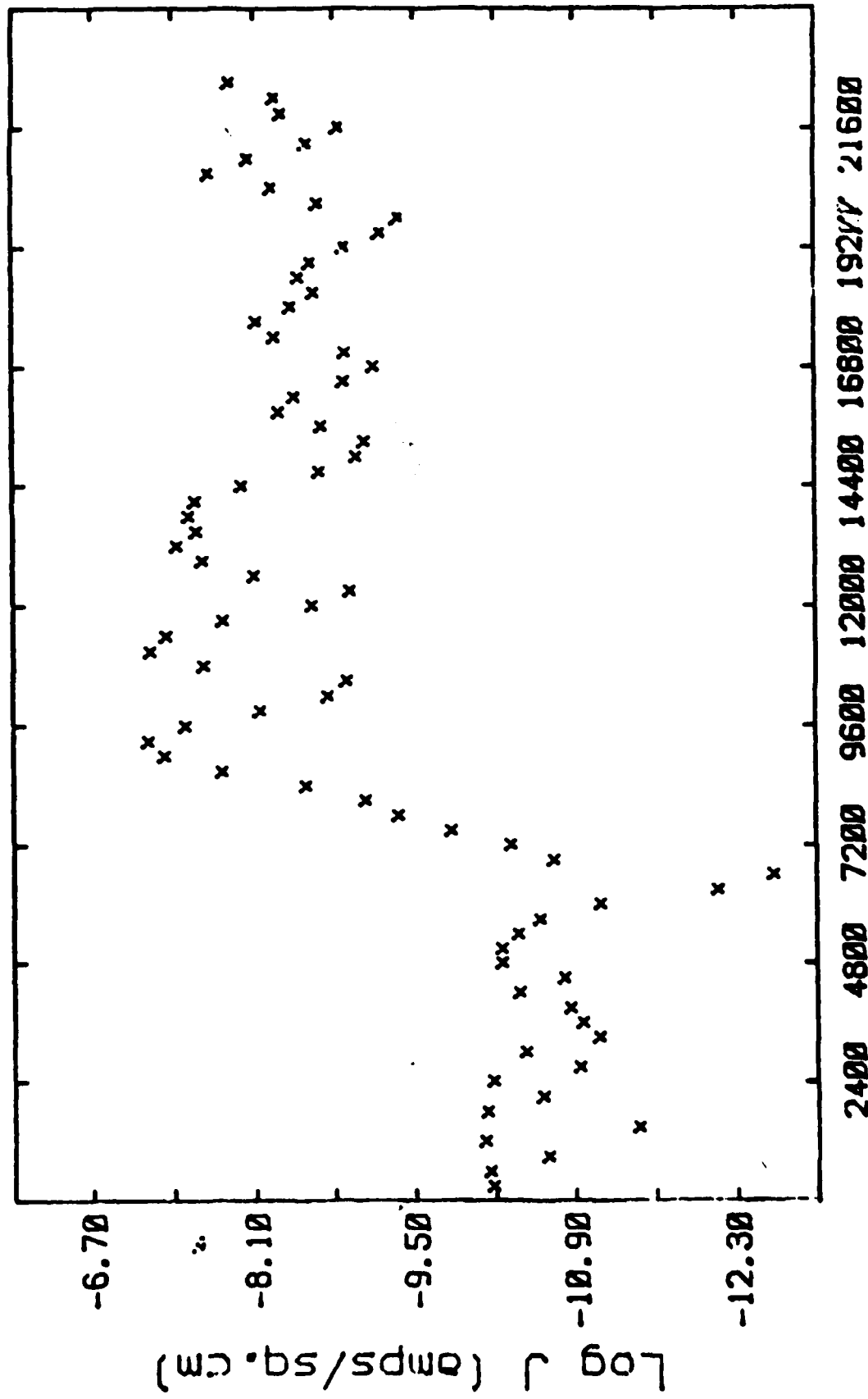


FIGURE 18

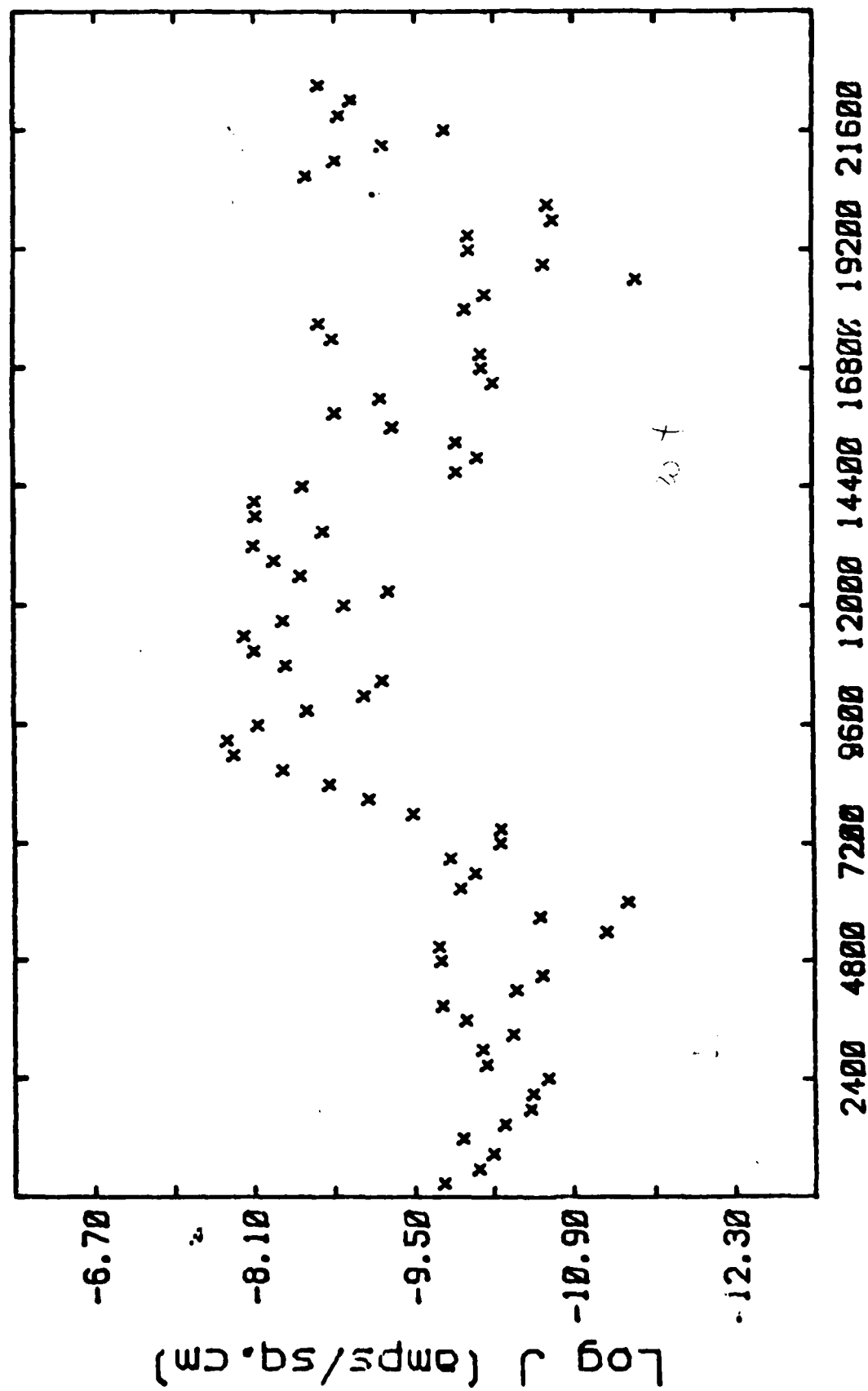
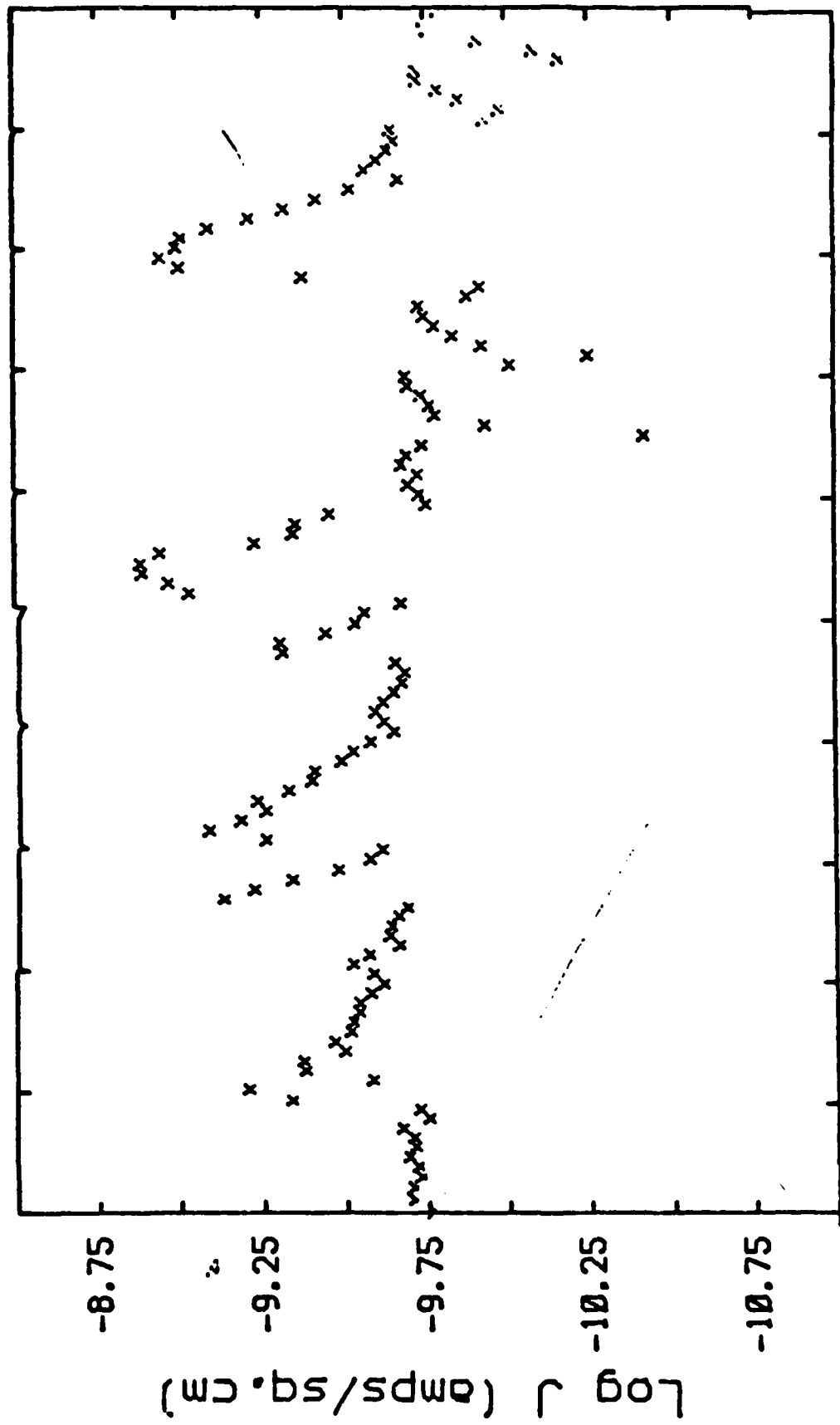


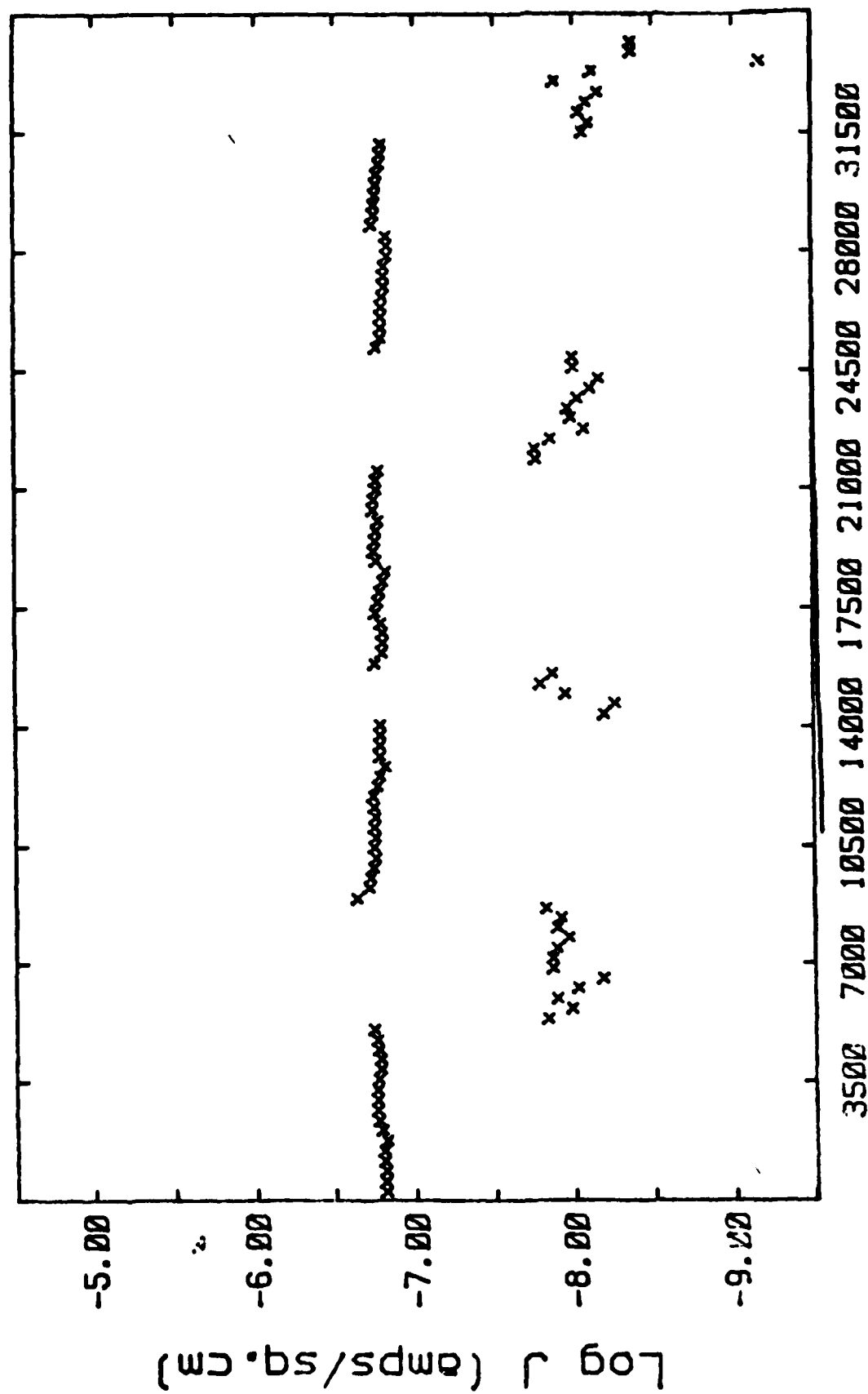
FIGURE 19



3700 7400 11100 14800 18500 22200 25900 29600 33300

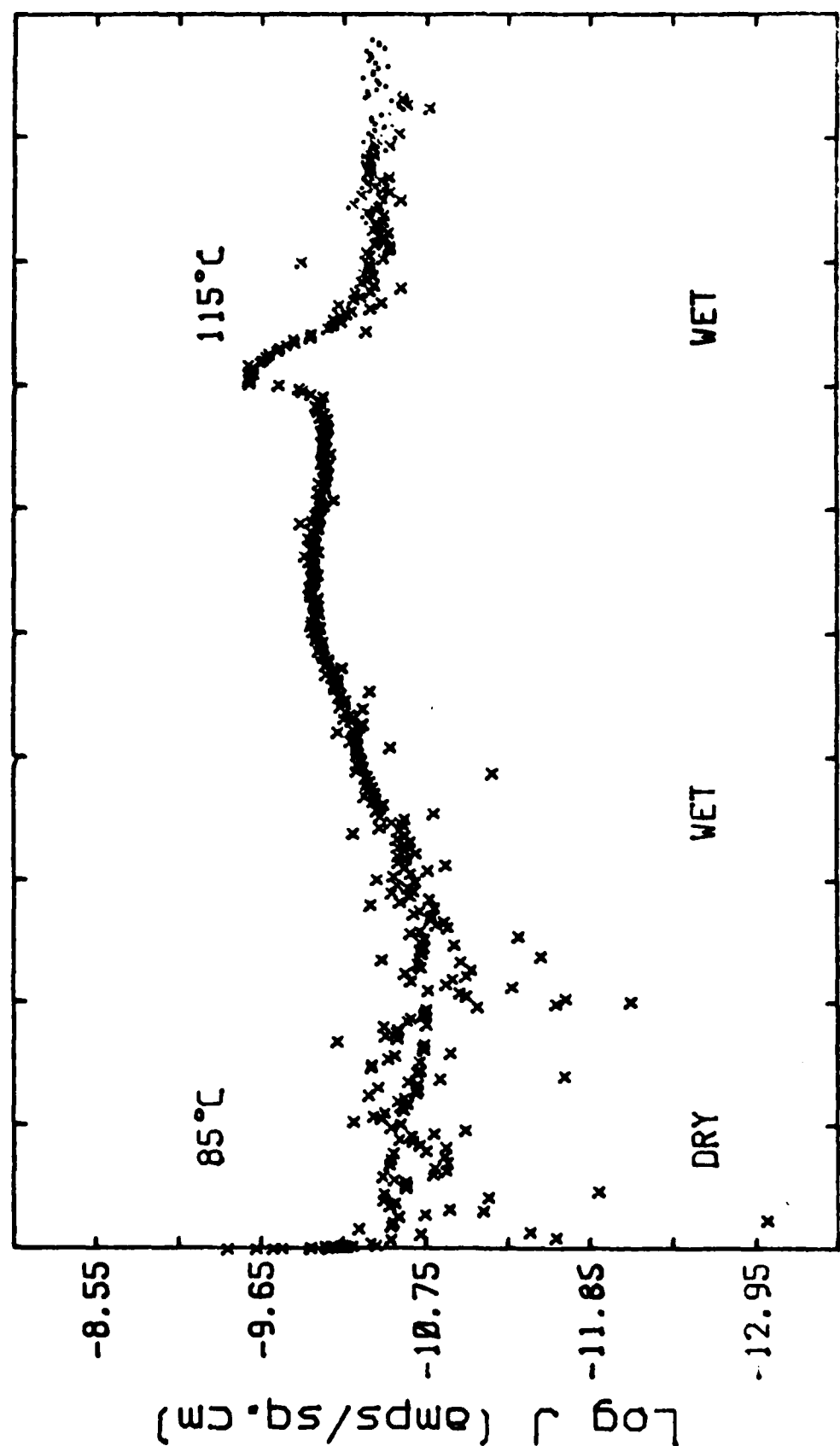
TIME (seconds)

FIGURE 20



TIME (seconds)

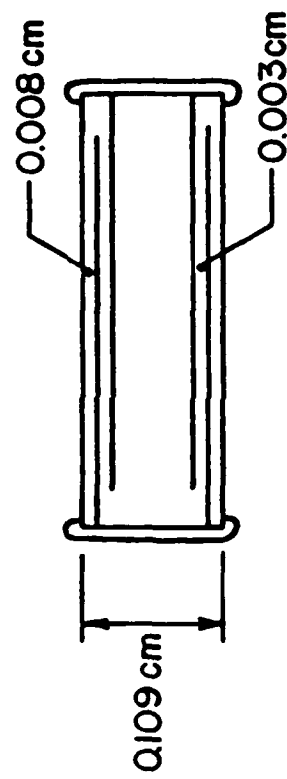
FIGURE 21



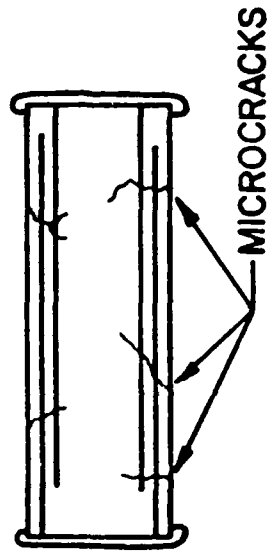
TIME (seconds)

FIGURE 22

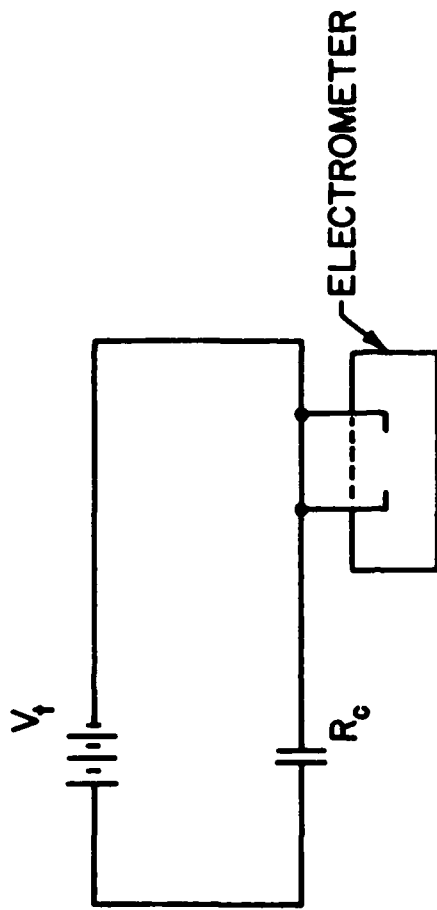
CAPACITOR BEFORE THERMAL SHOCKING



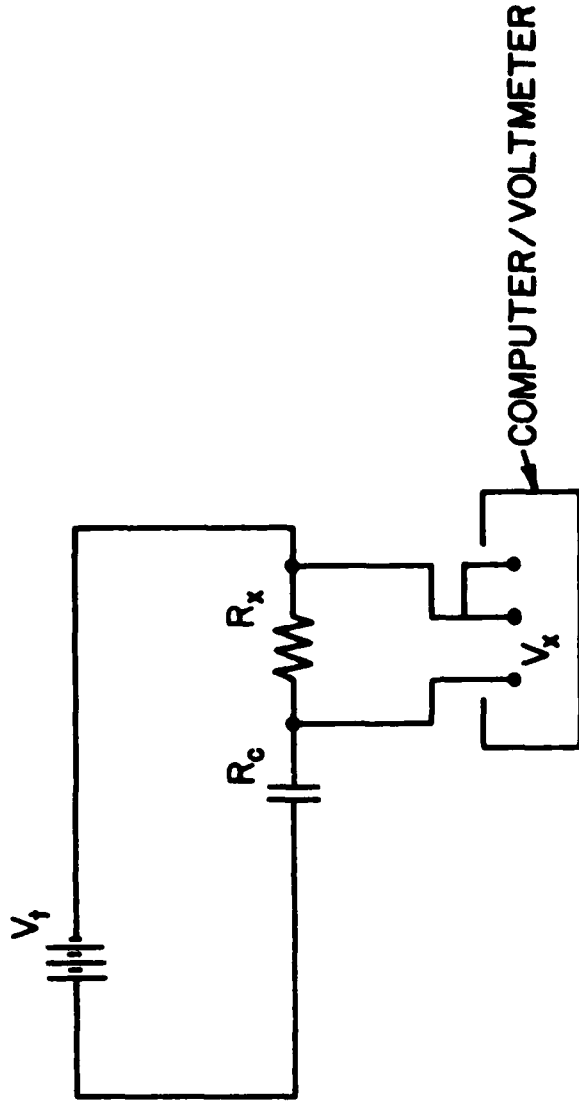
CAPACITOR AFTER THERMAL SHOCKING



SCHEMATIC OF TWO CAPACITOR TESTING APPARATUS

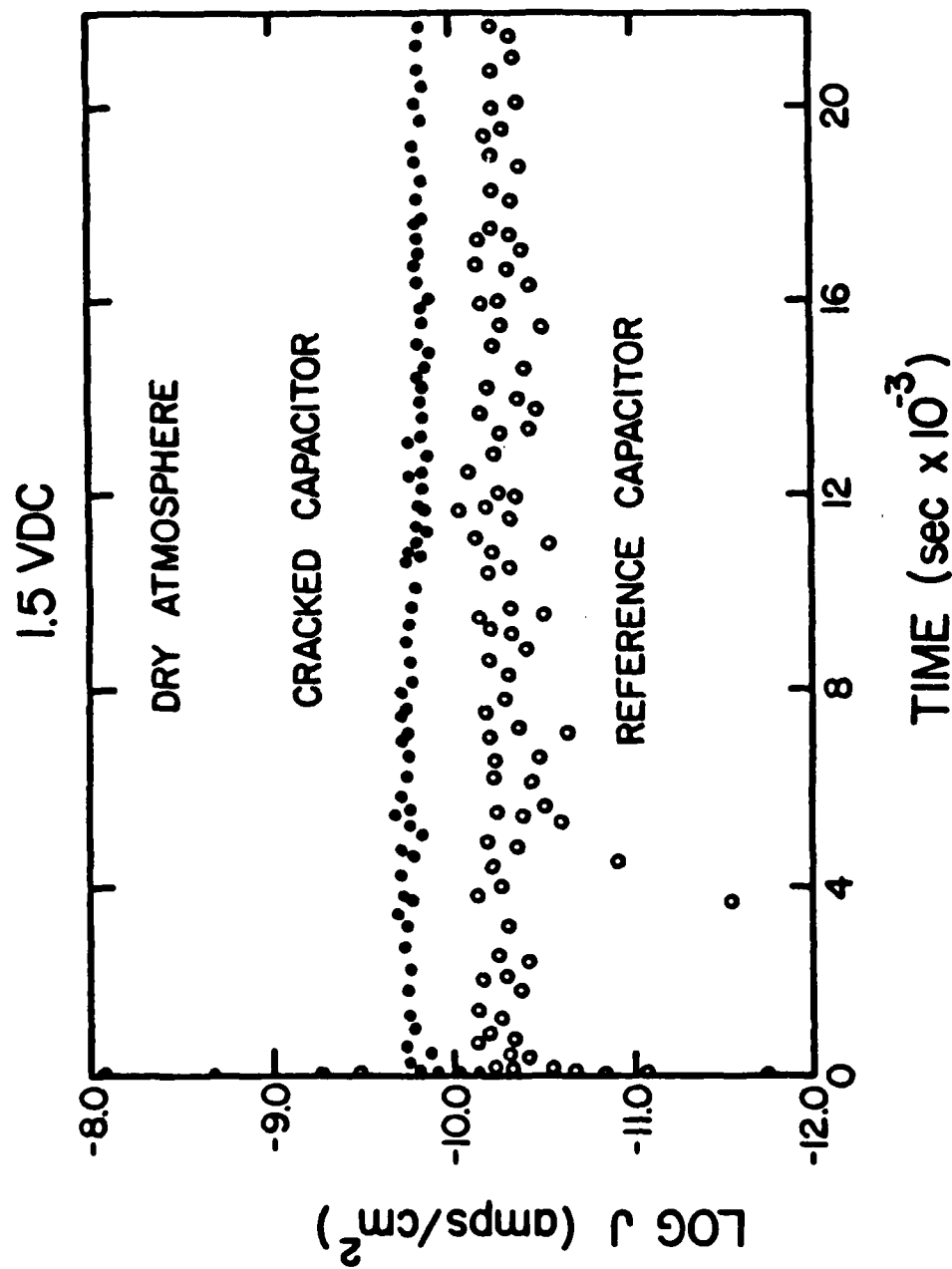


SCHEMATIC OF LIFE TESTING APPARATUS

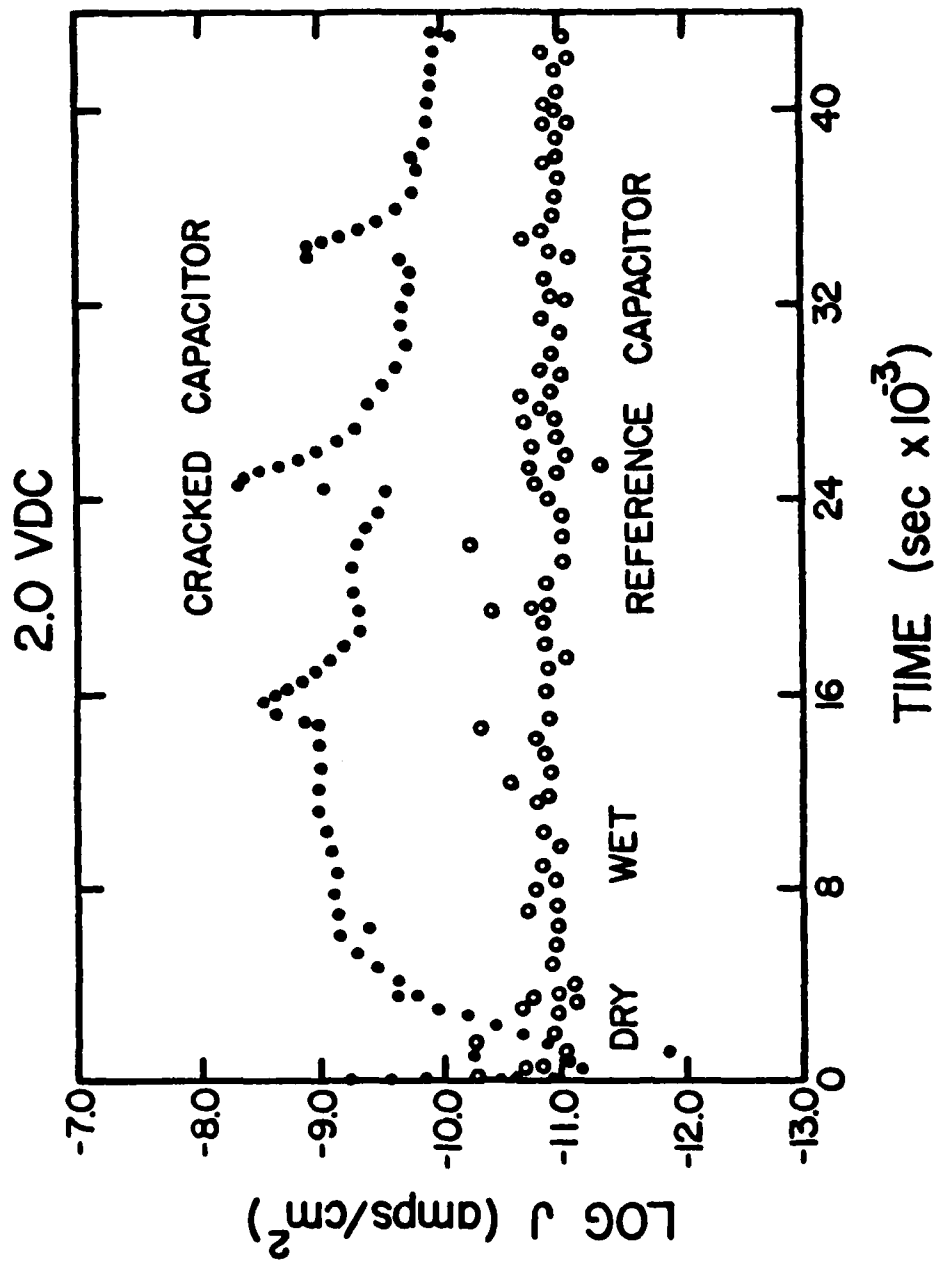


VOLTAGE READ: $V_x = V_t \frac{R_x}{R_c + R_x}$

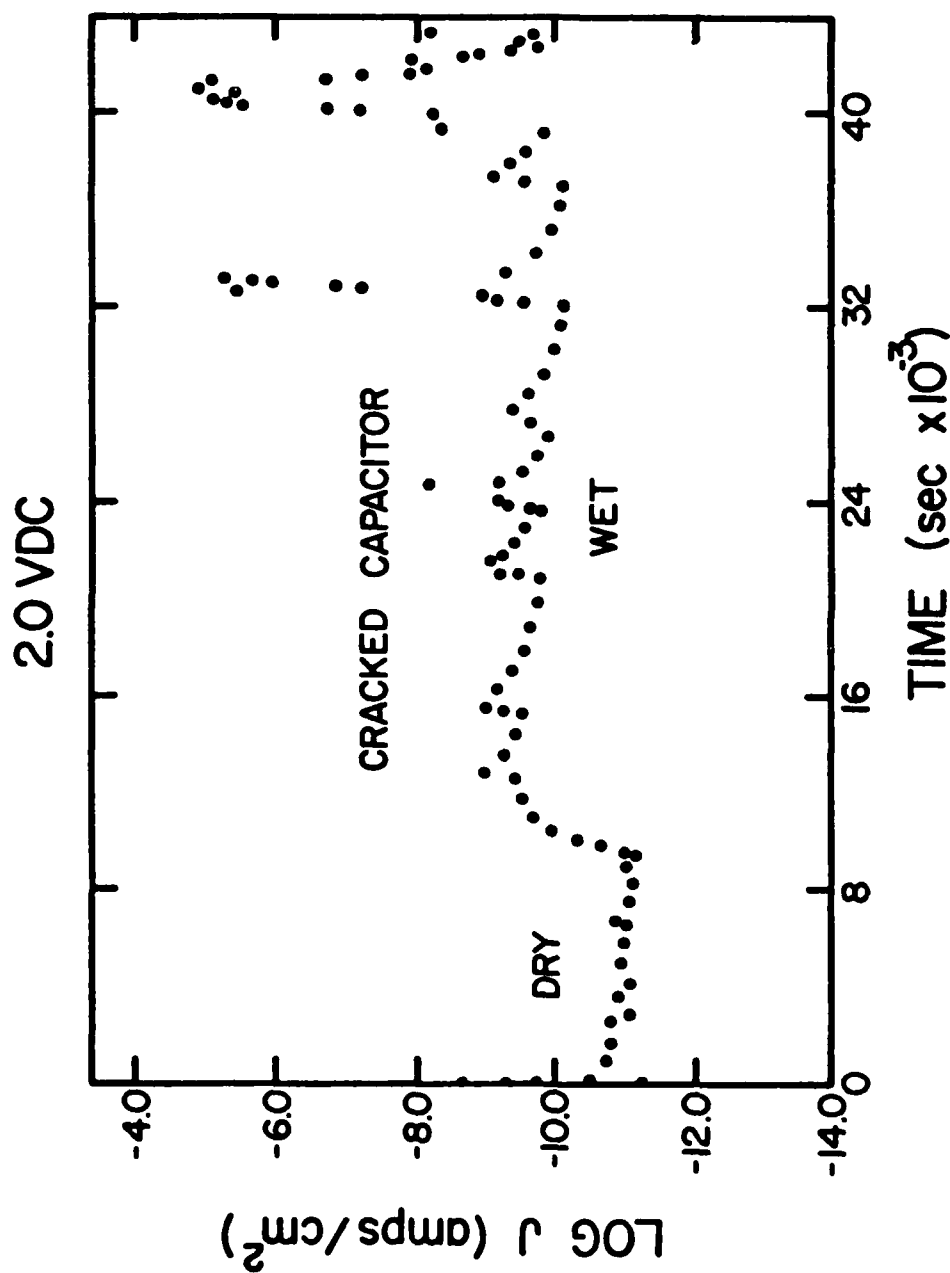
LEAKAGE CURRENT: $I_o = V_x / R_x$



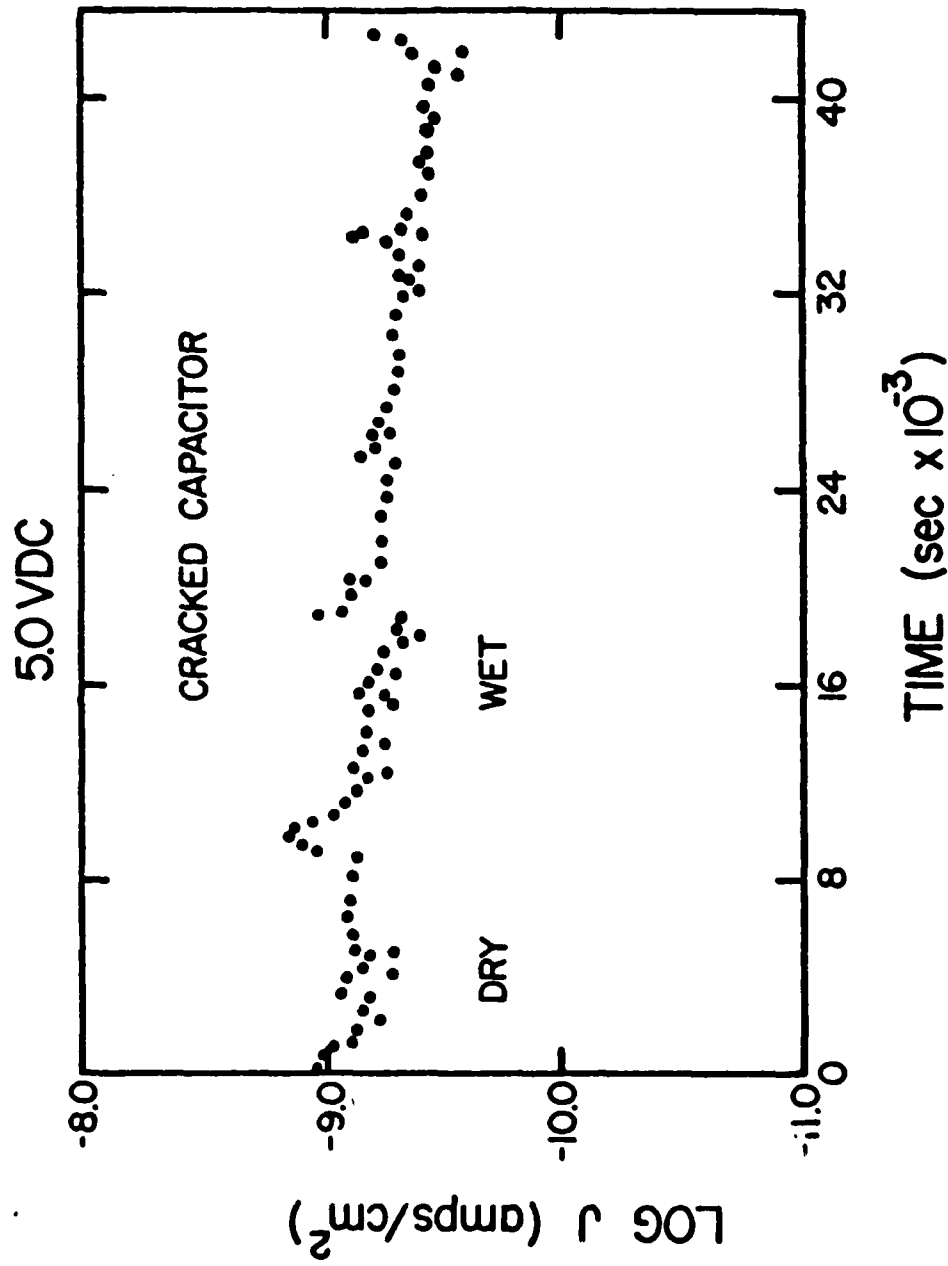
PLOT OF THE LOGARITHM OF THE LEAKAGE CURRENT DENSITY VS. TIME IN SECONDS FOR BOTH A CRACKED AND AN UNCRACKED CAPACITOR AT 85°C AND 1.5 VDC IN A DRY ATMOSPHERE.



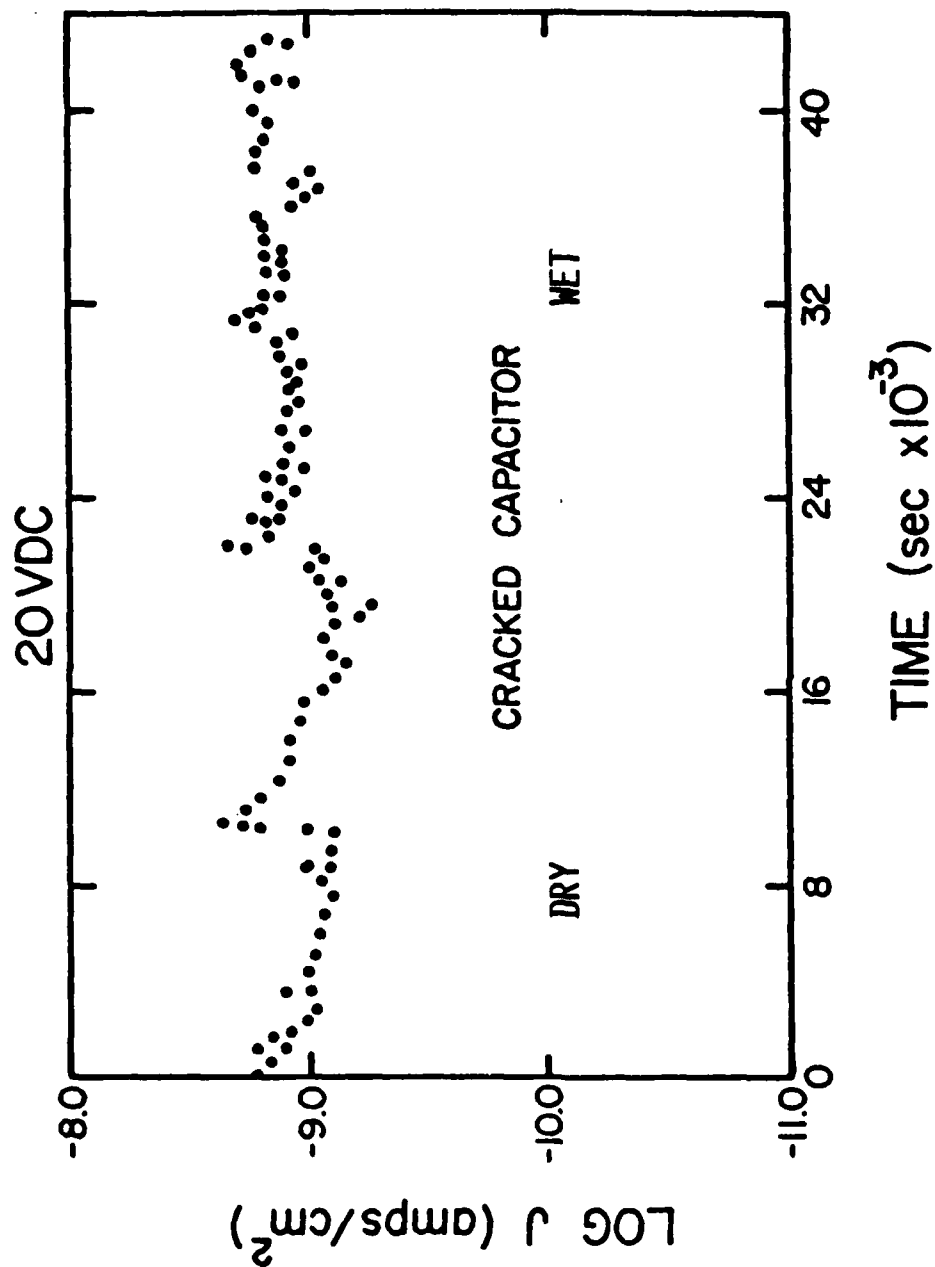
PLOT OF THE LOGARITHM OF THE LEAKAGE CURRENT DENSITY VS. TIME IN SECONDS FOR BOTH A CRACKED AND AN UNCRACKED CAPACITOR UNDERGOING THE 85/85 2.0 VDC TEST WITH VARYING ATMOSPHERE.



PLOT OF THE LOGARITHM OF THE LEAKAGE CURRENT DENSITY VS. TIME IN SECONDS FOR A CRACKED CAPACITOR UNDERGOING THE 85/85 2.0 VDC TEST WITH VARYING ATMOSPHERE.



PLOT OF THE LOGARITHM OF THE LEAKAGE CURRENT DENSITY VS. TIME IN SECONDS FOR A CRACKED CAPACITOR UNDERGOING THE 85/85 5.0 VDC TEST WITH VARYING ATMOSPHERE.

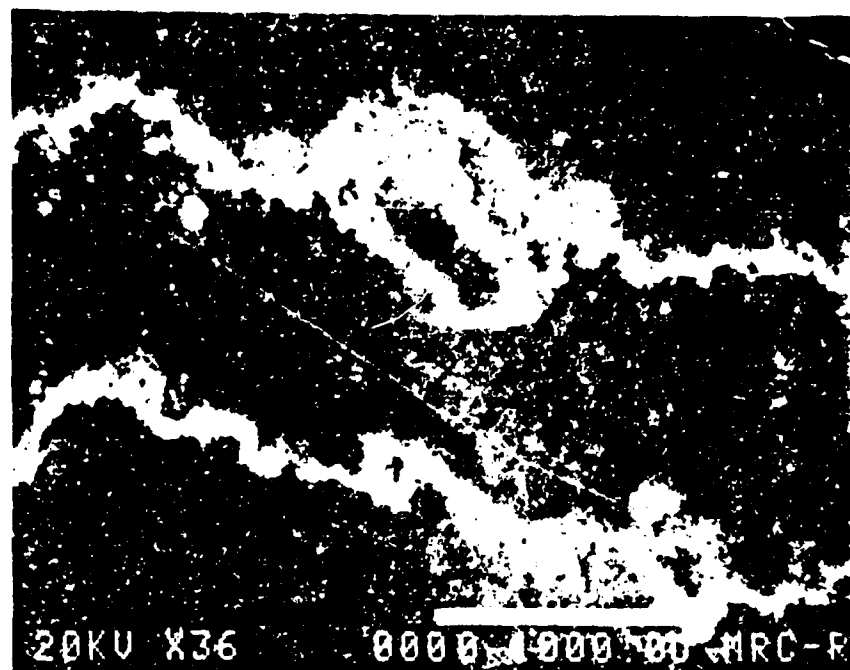


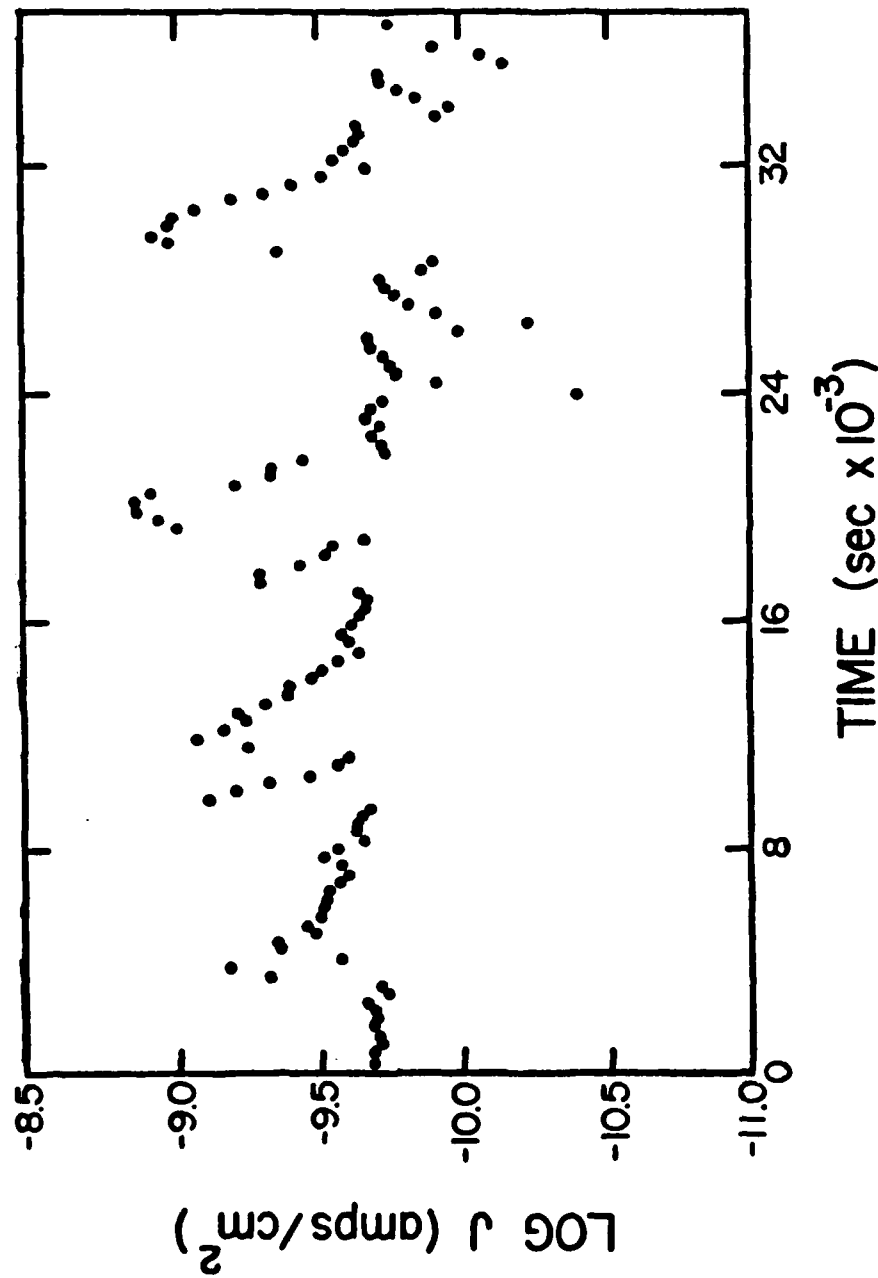
PLOT OF THE LOGARITHM OF THE LEAKAGE CURRENT DENSITY VS. TIME
IN SECONDS FOR A CRACKED CAPACITOR UNDERGOING THE 85/85 20.0 VDC
TEST WITH VARYING ATMOSPHERE.

Photomicrograph of a crack penetrating the electrode layers
magnified 1000x taken using the SEM.

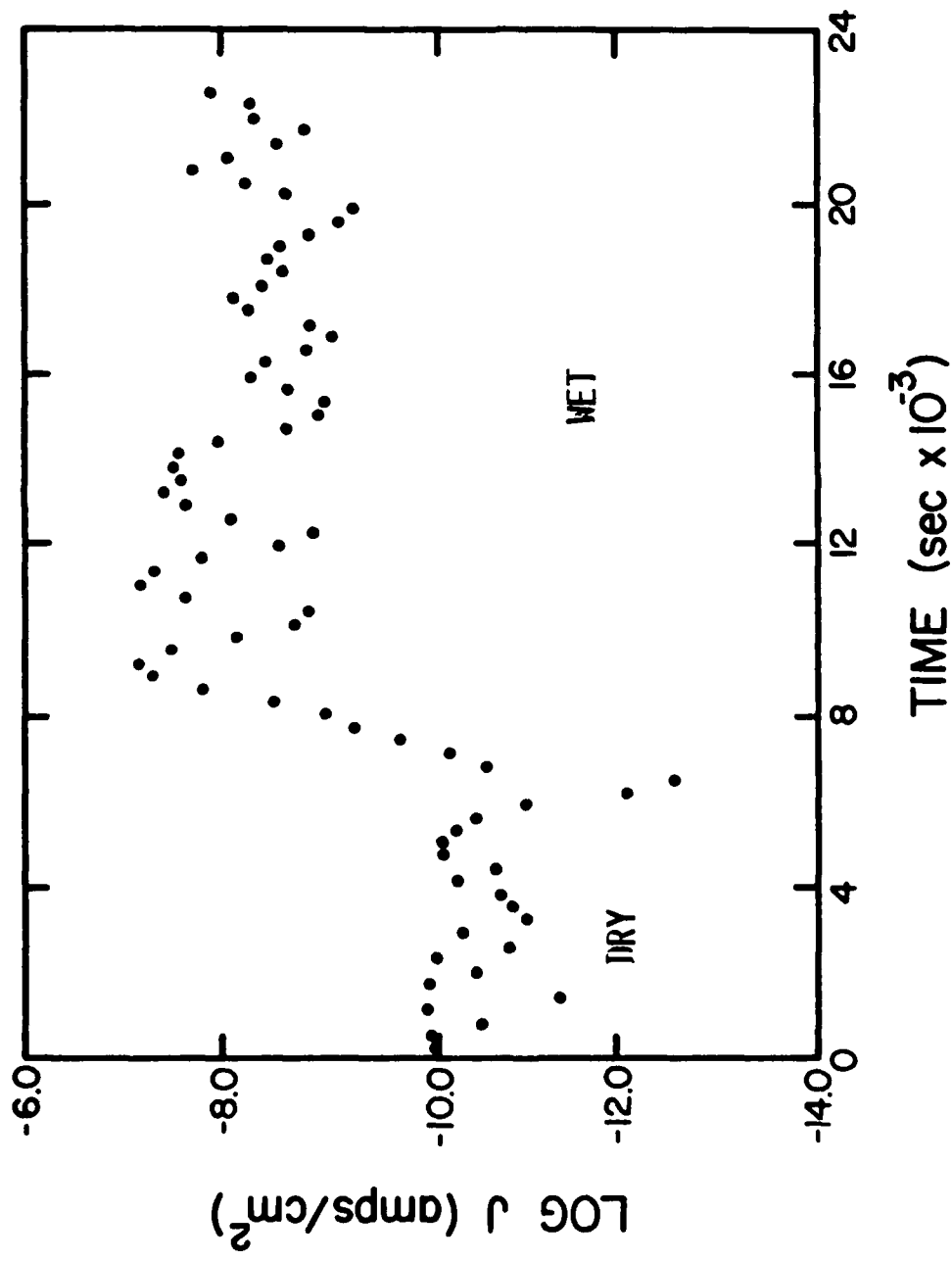


Photomicrograph of a crack parallel to the electrode layers penetrating the surface and electrode layers of a thermally shocked capacitor that exhibited low-voltage breakdown.

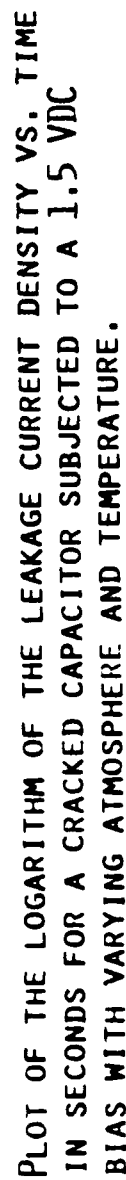




PLOT OF THE LOGARITHM OF THE LEAKAGE CURRENT DENSITY VS. TIME
IN SECONDS FOR A CRACKED CAPACITOR UNDERGOING THE 85/85 1.5 VDC
TEST WITH HUMID ATMOSPHERE (EXCERPT FROM THE LIFE TESTS).



PLOT OF THE LOGARITHM OF THE LEAKAGE CURRENT DENSITY VS. TIME IN SECONDS FOR A CRACKED CAPACITOR UNDERGOING THE 85/85 1.5 VDC TEST WITH VARYING ATMOSPHERE (EXCERPT FROM THE LIFE TESTS).



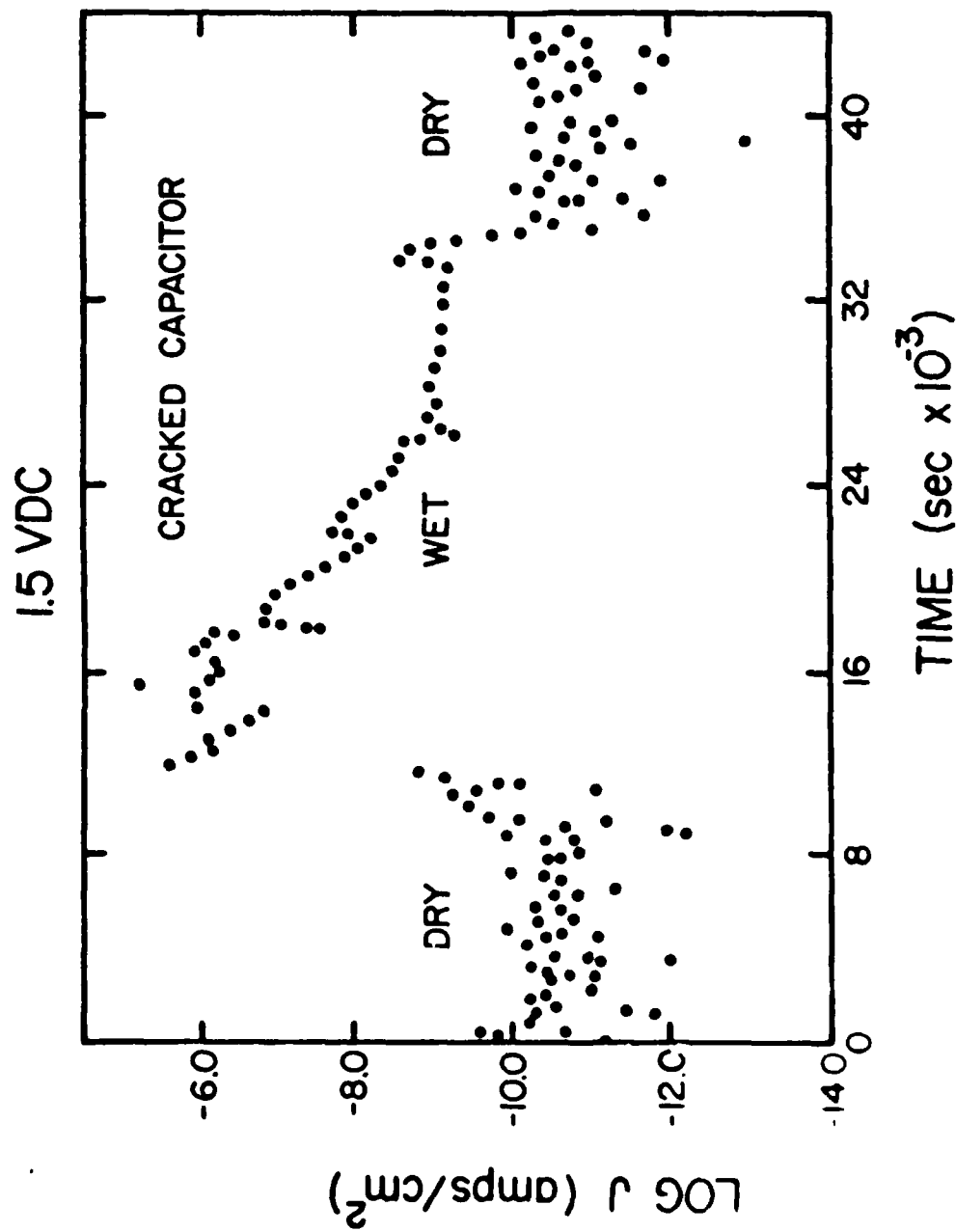


FIGURE 1. LOGARITHM OF THE LEAKAGE CURRENT DENSITY
 VS. TIME IN SECONDS FOR A CRACKED CAPACITOR UNDERGOING
 A 40/80 1.5 VDC TEST WITH VARYING ATMOSPHERE.

RELIABILITY STUDIES OF CERAMIC CAPACITORS(U) MISSOURI
UNIV-ROLLA H U ANDERSON MAR 87 N00014-82-K-0294

2/2

UNCLASSIFIED

F/G 9/1

NL

1.0
1.1
1.25
1.4
1.6
1.8
2.0
2.2
2.5
2.8
3.2
3.6
4.0
4.5
5.0
5.6
6.3
7.1
8.0
9.0
10.0
11.2
12.5
14.0
16.0
18.0
20.0
22.4
25.0
28.0
31.5
36.0
40.0
45.0
50.0
56.0
63.0
71.0
80.0
90.0
100.0

APPENDIX E

Contribution to the Electrical and Mechanical Phase Diagram
of La-Doped Lead Zirconate Titanate

D. Viehland

**Contributions to the Electrical and Mechanical
Phase Diagram of La-Doped Lead Zirconate Titanate**

D. Viehland

Introduction

The purpose of this work was to investigate the mechanical and electrical phase diagram of La doped PbZrO_3 (65%) - PbTiO_3 (35%) (PLZT 65/35) in the range from 8 to 12 at%.

The temperature and field dependent polarization/depolarization behavior of PLZT near 8 at.% La has been studied by a number of workers (1-8). Cross (1,2) proposed a model of electrical field ordering of polar microdomains immersed in a cubic paraelectric matrix. This model was put forward to account for the observed electric field dependence of the polarization vs. temperature in the ferroelectric phase.

Induced phase transformations, rather than orientation of microdomains have been proposed for PLZT based on dielectric and optical effects caused by electric fields (3-7), and by uniaxial stress (8).

The goals of this investigation were: 1) to determine the elastic softening temperature in PLZT above 8 at.% La, 2) to study the relative dielectric constant (K) and the

dissipation factor (dF) as a function of temperature and frequency, and 3) to study the polarization/depolarization behavior of PLZT using thermally stimulated current.

Measurement Techniques

Elastic Softening

In order to measure the elastic softening temperature independent of the piezoelectric constant, a long thin vibrating reed was externally driven by a magnetic gradient acting on a small permanent magnet attached to the reed. The elastic properties were studied over the temperature range from 260 to 360°K, with resonance frequencies less than 100 Hz. The resonant frequency was adjusted by using different magnet masses. The resulting asymmetric resonance curves were analyzed using the Wuttig and Suzuki theory of non-linear anelasticity (9-11) to determine the resonance frequency, the third order spring constant, and the linear damping. The apparatus used has been described previously (9-11). A schematic of the measurement system is shown in figure 1.

Dielectric Measurements

The capacitance and dissipation factor were measured as a function of frequency and temperature. The

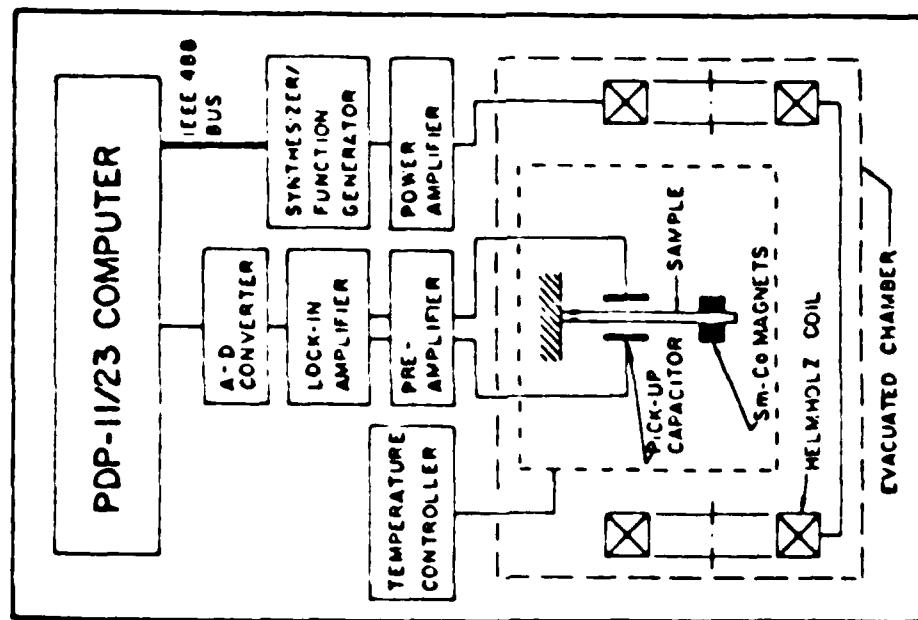


Figure 1. Schematic diagram of the apparatus used in the elasticity measurements.

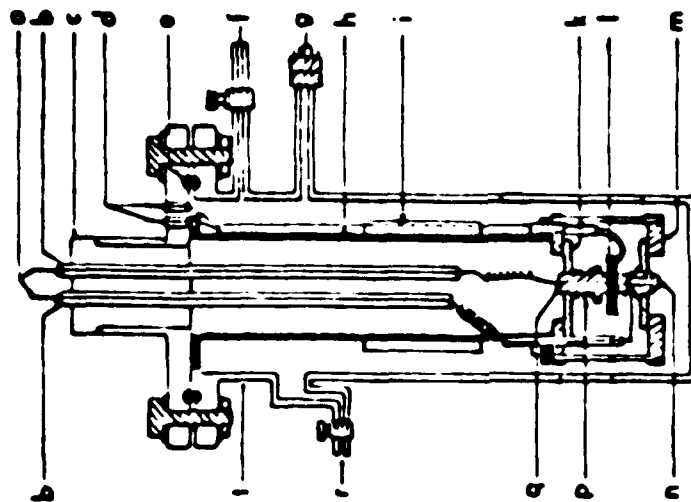


Figure 2. Thermally Stimulated Current / Dielectric test chamber. a) copper wire to contacts, b) stainless tube, c) teflon insulation, d) thermocouple, e) o-ring, f) bellon inlet, g) outlet to vacuum pump, h) stainless steel tube, i) heating tape, j) metal support insulated with teflon tape, k) test sample, l) metal support insulated with teflon tape, m) set screw, n) spring, o) set screw, p) exhaust outlet, q) stainless steel container.

frequencies used were 0.01 KHz, 1KHz and 100 KHz. The measurements were made over the temperature range 180 to 420°K, the heating rate was approximately 4°K/min. The electrode used was InGa. The test chamber and equipment used have been described in previous reports. The test chamber is shown in figure 2.

Thermally Stimulated Current

The capacitors were electroded with In-Ga and placed in the chamber. The sealed chamber was heated to about 420°K, evacuated and then filled with He. The temperature was cooled to about 180°K with liquid nitrogen and a field was applied (500v/cm). The current was measured as the temperature was increased at a rate of approximately 4°K/min to 420°K (first polarization run). The system was then quenched to near 180°K and the process was repeated (2nd polarization run). The system was then quenched again to 180°K, the field was removed, and the measurement was repeated (3rd polarization run). The test chamber and equipment used have been described in previous reports. The test chamber is shown in figure 2.

Discussion of Results

A summary of the results of this study is shown as additions to the phase diagram of Meitzler and O'Bryan (3) in figure 3. Data obtained by a common technique for the

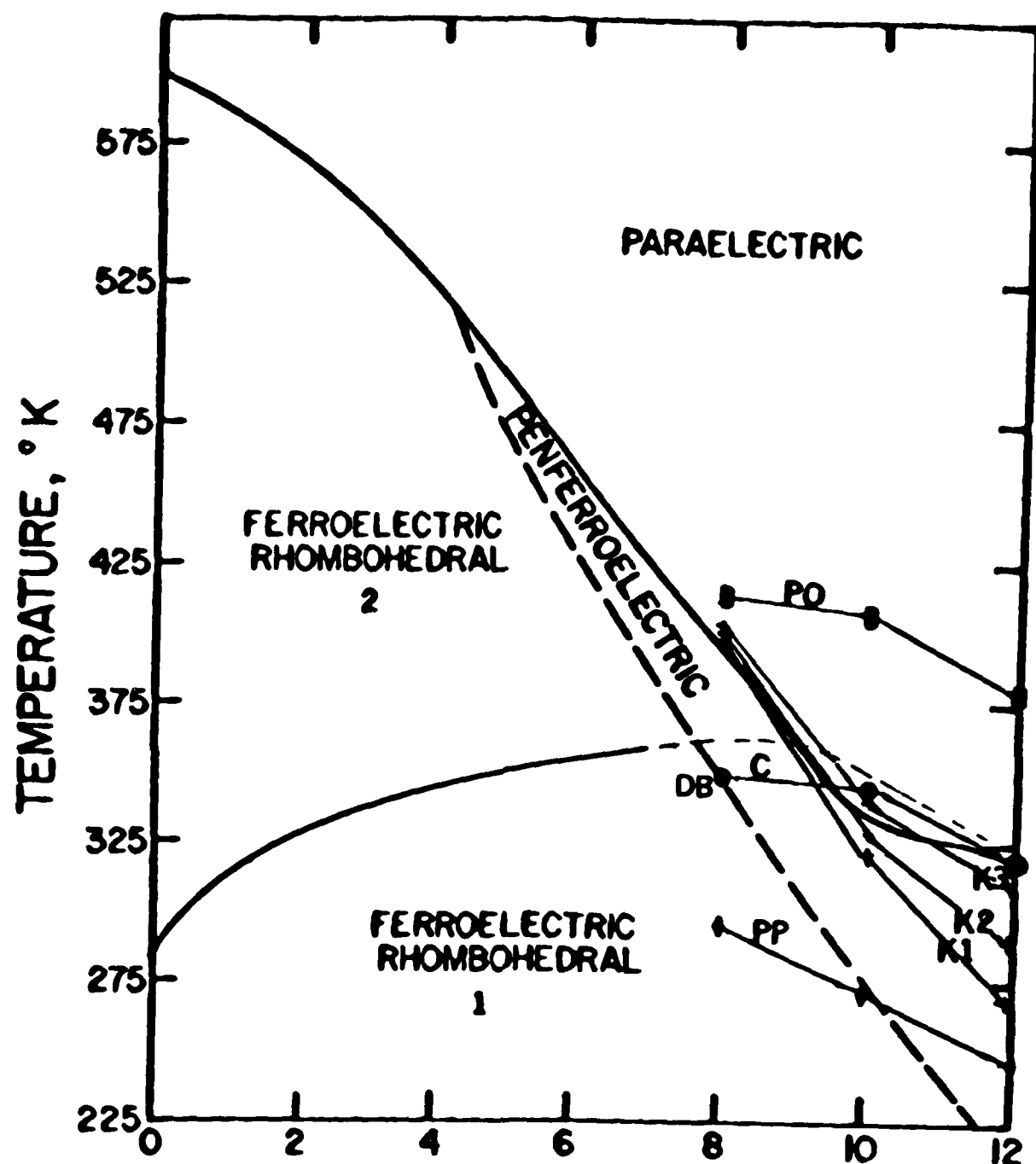


Figure 3. Modified phase diagram for PLZT (65/35) as a function of temperature and La content. New boundaries were determined by a maxima in the polarization (PP), elastic constants (C), zero polarization (PO), a "bump" in the dissipation factor (DB), dielectric maxima for 0.01 KHz (K1), dielectric maxima for 1 KHz (K2), and dielectric maxima at 100 KHz (K3).

three compositions are connected by lines to guide the eye. The major contributions are 1) the extension of the lattice softening boundary beyond 8 at% La, 2) the confirmation of the penferroelectric boundaries, and 3) the identification of the nearly linear depolarization as the sample temperature approaches the upper boundary of the penferroelectric region.

Elastic Softening

Representative data from this study are shown in figures 4-7. The third order spring constant and the resonance frequency showed a minimum near 350°K , 345°K and 320°K for PLZT-8 (PLZT with 8 at% La, same notation for other compositions), PLZT-10, and PLZT-12 (illustrated in figures 4 and 5). Near the same temperature for each composition, a sharp drop in the dissipation factor occurred (illustrated in figures 6 and 7).

The temperatures of the observed elastic softening are shown on the phase diagram in figure 3 as line C. The elastic softening occurred near the ferro/penferroelectric phase boundary for PLZT-8, and correlated with a bump in the dissipation factor. For PLZT-10 and PLZT-12, the effect was near the reported penferro/paraelectric phase boundary (3), and correlated with the maximum in the dielectric constant. A correlation which may add some insight is that the relaxor behavior does not

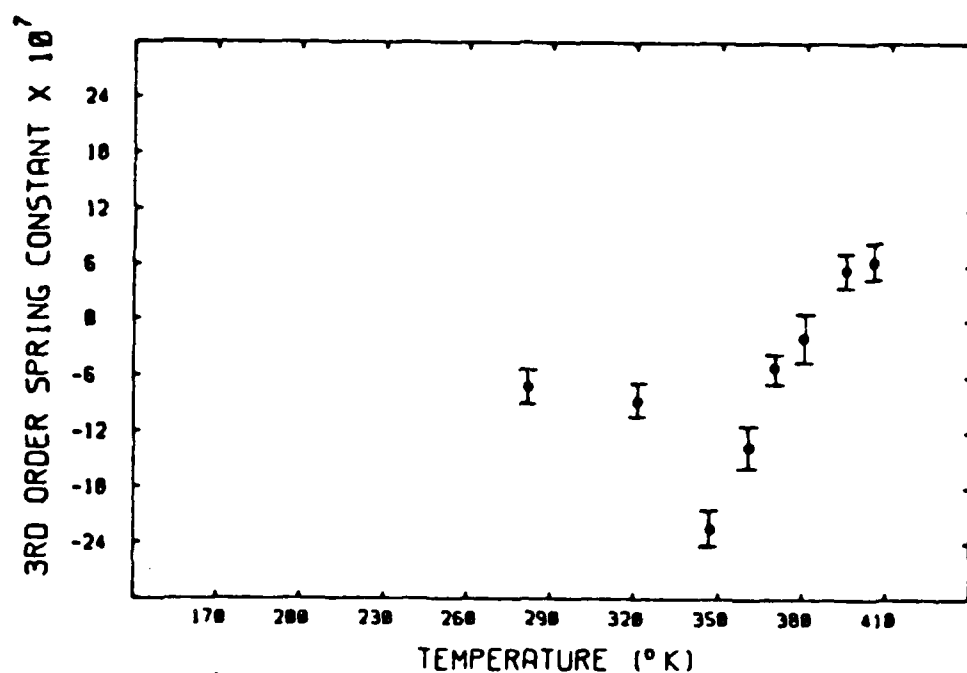


Figure 4. Third order spring constant, $w\tau(C_2/C_2^2)K$, with a 95% confidence limit as a function of temperature for PLZT-8.

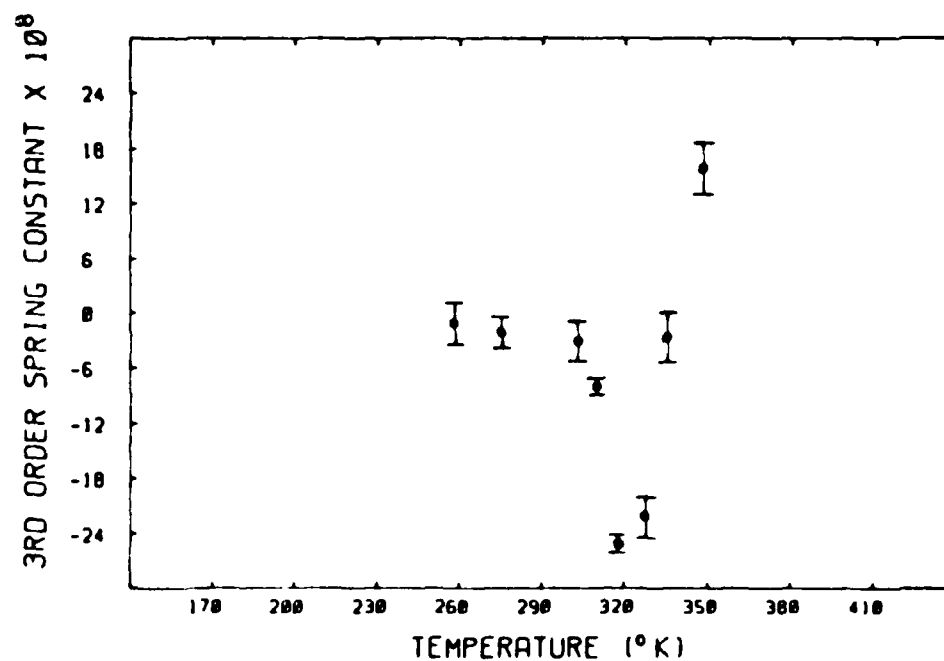


Figure 5. Third order spring constant, $w\tau(C_2/C_2^2)K$, with a 95% confidence limit as a function of temperature for PLZT-12.

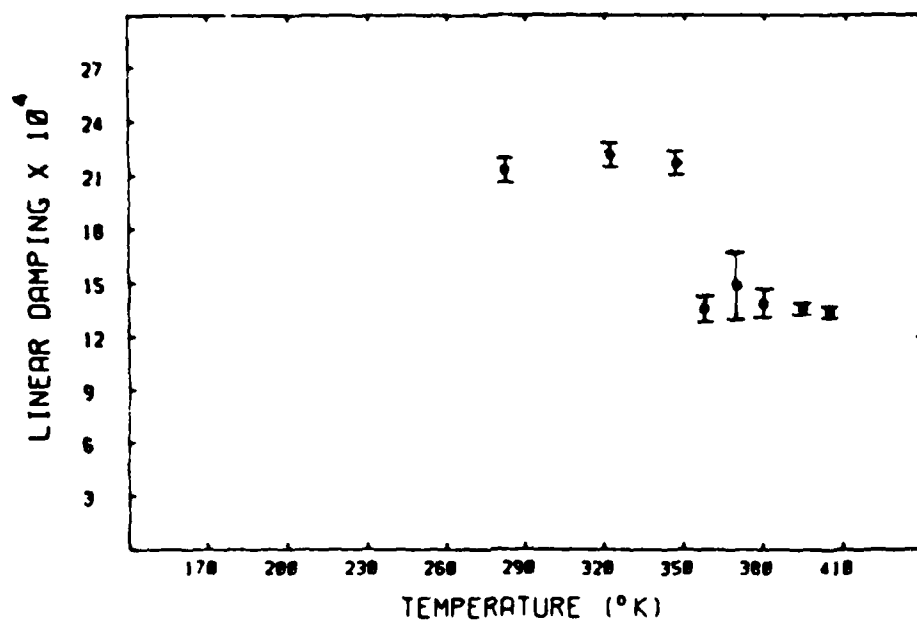


Figure 6. Linear Damping, $\omega \tau (C_p/C_s - 1)$, with a 95% confidence limit as a function of temperature for PLZT-8.

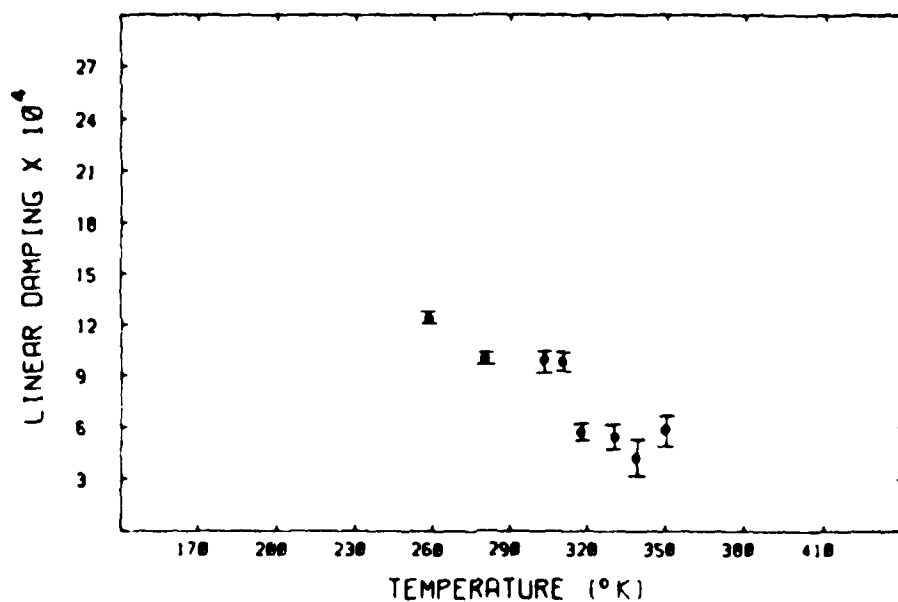


Figure 7. Linear damping, $\omega \tau (C_p/C_s - 1)$, with a 95% confidence limit as a function of temperature for PLZT-12.

occur for a La content less than 8 at%, and as the La content is increased (shown in the dielectric portion of this study) the frequency dependence of the maxima increases.

The source for the elastic softening near the ferro/penferroelectric phase boundary in PLZT-8 and near the penferro/ paraelectric phase boundary in PLZT-10 and PLZT-12 is not certain at this time. A possibility is that the lattice softening is associated with a macro to microdomain transition in PLZT-8, and associated with a polar to nonpolar transformation in PLZT-10 and PLZT-12.

Dielectric Measurements

Representative data from this study are shown in figures 8-11. With increasing La content the frequency dependence of the maximum in the dielectric constant increased, the maximum became more dispersive, and the temperature of the maximum was shifted down. The maximum in the dielectric constant at 100KHz correlated with the observed elastic softening. The dielectric constant maxima are shown on the phase diagram in figure 3. The maxima for 0.01KHz, 1KHz, and 100KHz are shown as lines K1, K2, and K3 respectively. The maxima lie below the penferro/paraelectric phase boundary, and approach this boundary as the frequency is increased.

The dissipation factor for PLZT-8 had a bump which

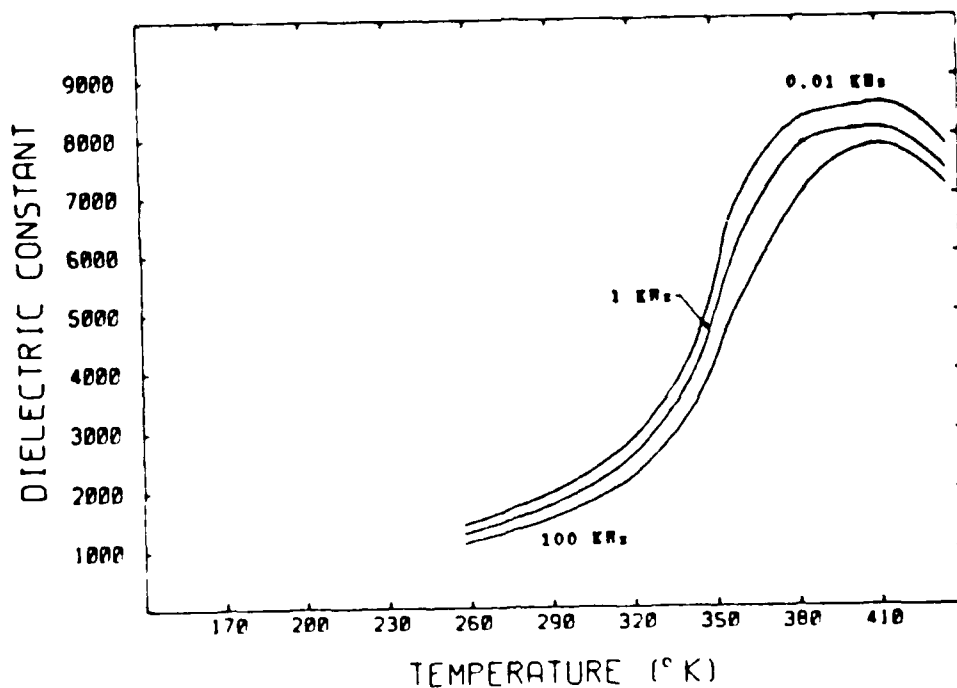


Figure 8. Dielectric constant as function of temperature at frequencies of 0.01 KHz, 1 KHz, and 100 KHz for PLZT-R.

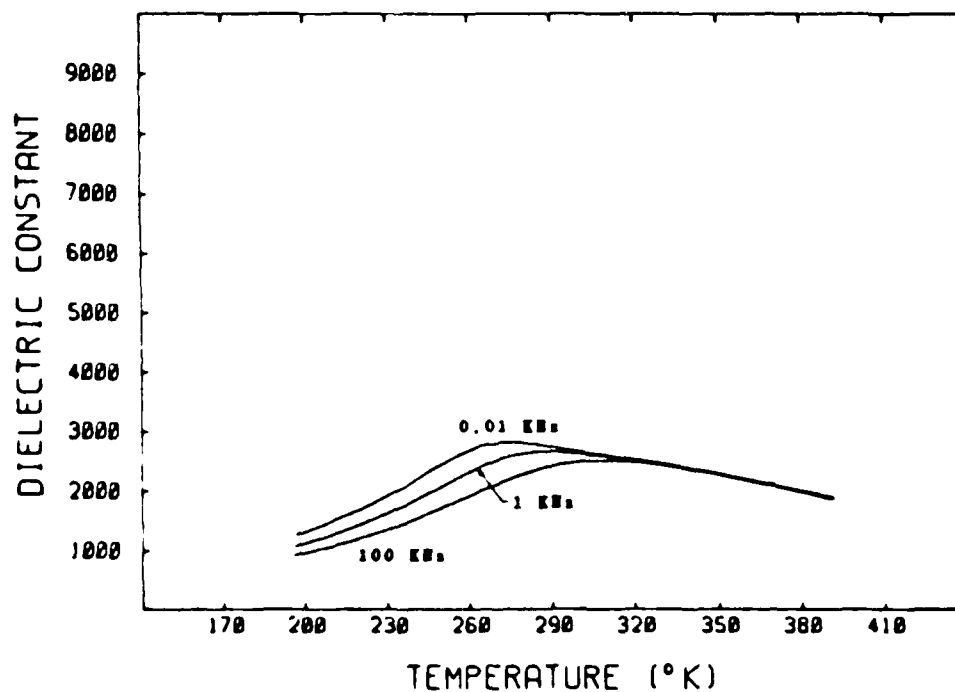


Figure 9. Dielectric constant as function of temperature at frequencies of 0.01 KHz, 1 KHz, and 100 KHz for PLZT-12.

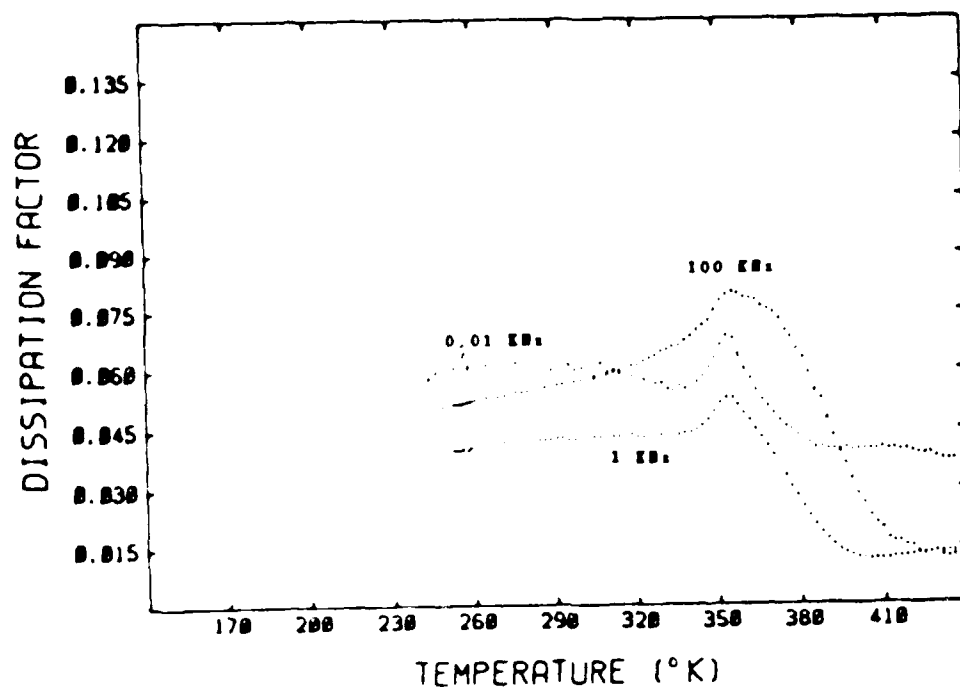


Figure 10. Dissipation factor as a function of temperature at frequencies of 0.01 KHz, 1 KHz, and 100 KHz for PLZT-R.

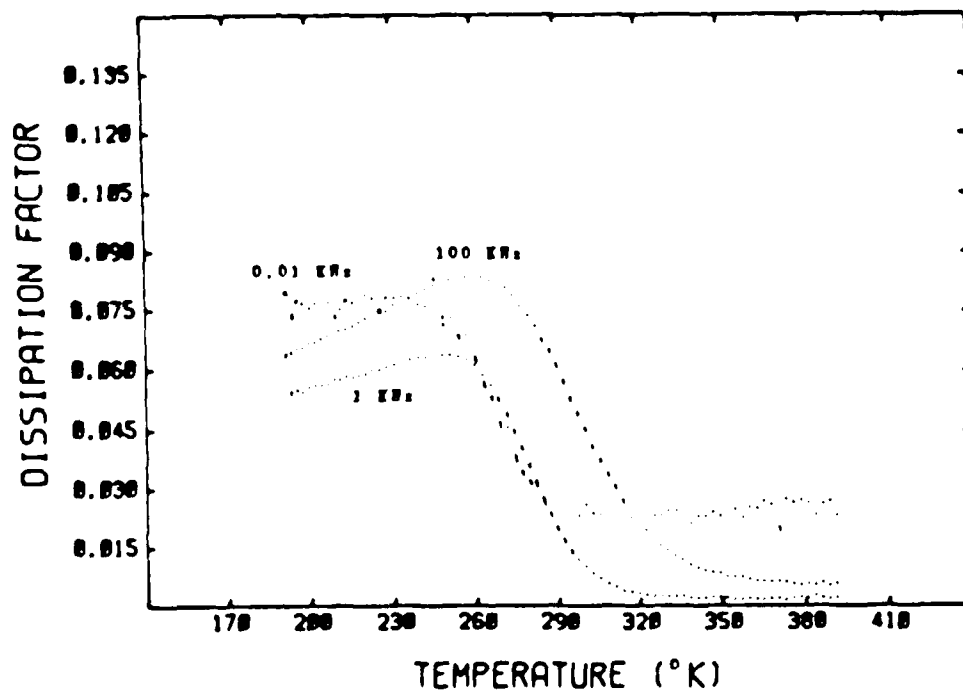


Figure 11. Dissipation factor as a function of temperature at frequencies of 0.01 KHz, 1 KHz, and 100 KHz for PLZT-12.

correlated with the elastic softening. As the La content was increased the maximum in the dissipation factor became more dispersive and frequency dependent. The bump in the dissipation factor for PLZT-8 occurred at the ferro/penferroelectric boundary, and is shown on the phase diagram in figure 3 as point DP.

Thermally Stimulated Current

Representative data from this study are shown in figures 12 and 13, and representative graphs of the polarization, calculated from the thermally stimulated current (TSC), are shown in figures 14-16.

The temperature at which the polarization maxima occurred during the first polarization run was obtained from the maximum slope in the TSC spectra at 295°K , 270°K , and 245°K for PLZT-8, PLZT-10, and PLZT-12 respectively. Above the maximum, depolarization occurred linearly with temperature as evidence from the constant negative current of the TSC spectra and the polarization curves. The temperature at which the depolarization was complete was obtained from the maximum slope in the TSC spectra at 415°K , 410°K , and 380°K for PLZT-8, PLZT-10, and PLZT-12 respectively.

During the second polarization, depolarization occurred linearly throughout the temperature region investigated as evidence from the nearly constant negative

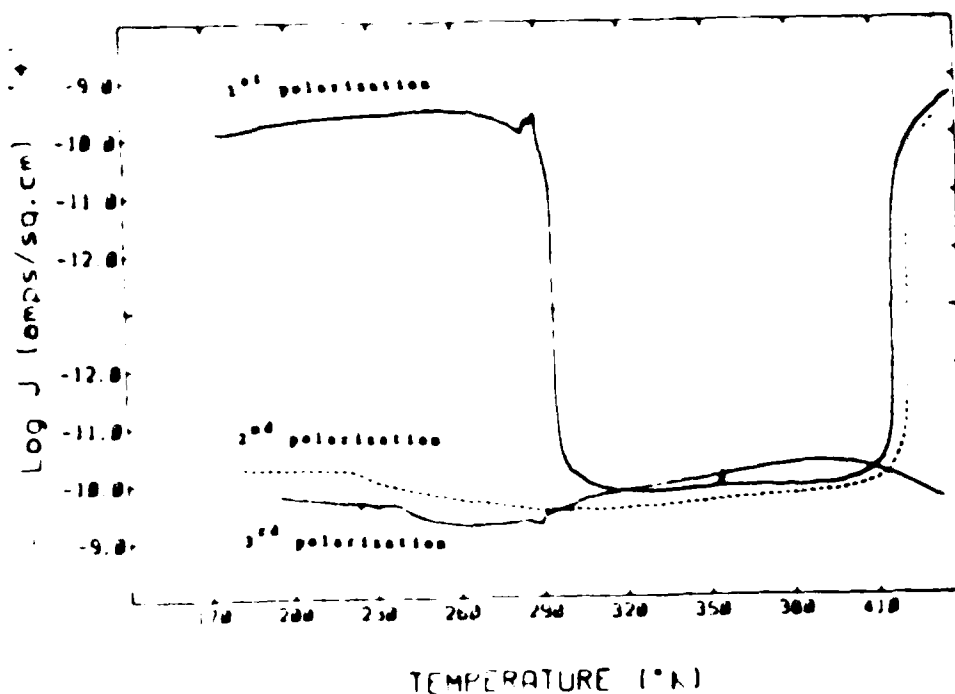


Figure 12. Thermally Stimulated Current spectra of PLZT 8.

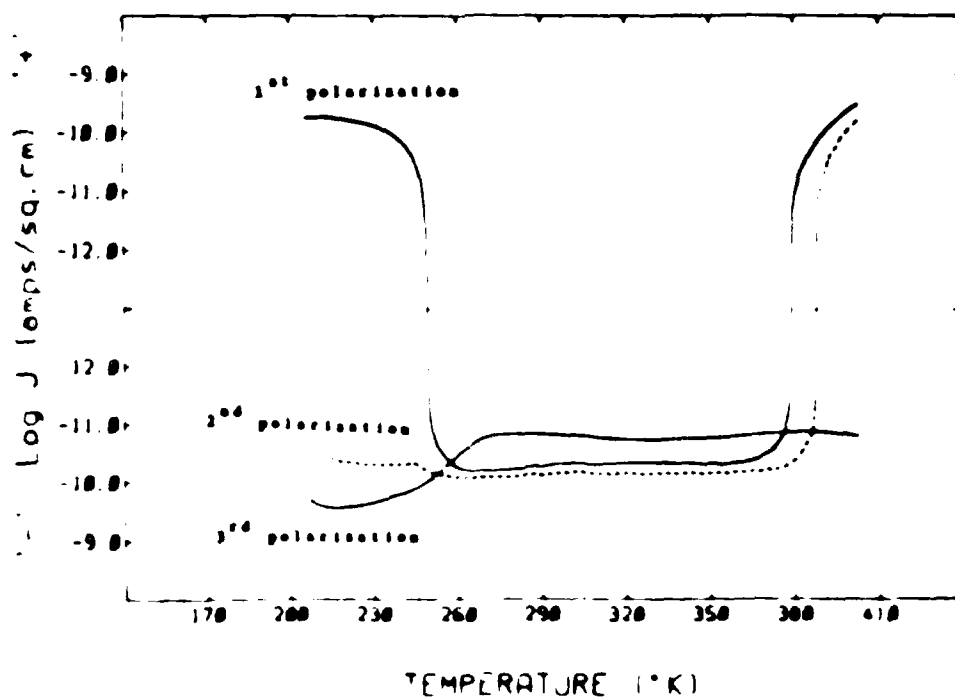


Figure 13. Thermally Stimulated Current spectra of PLZT 12.

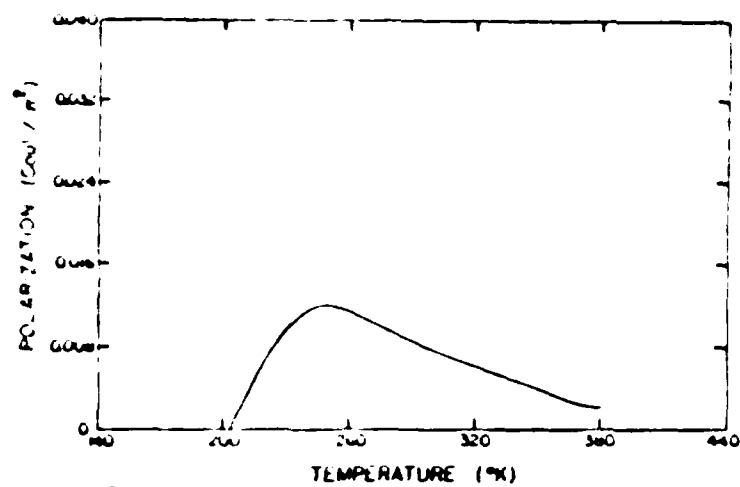


Figure 16. Polarization curve for Pt-112.

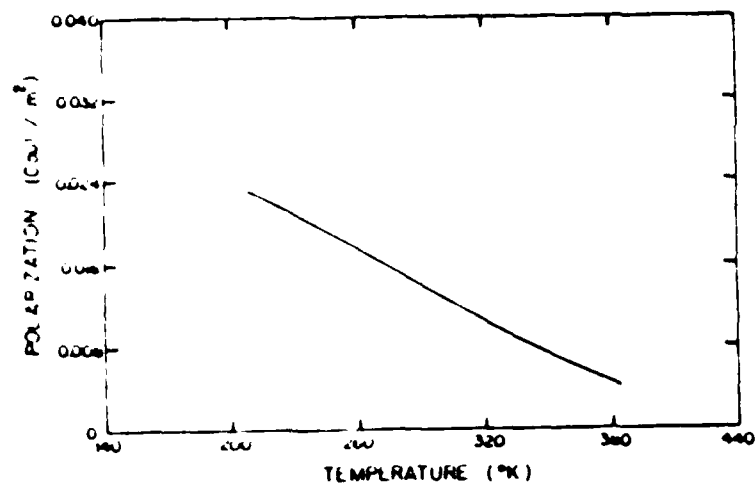


Figure 17. Polarization curve for Pt-112.

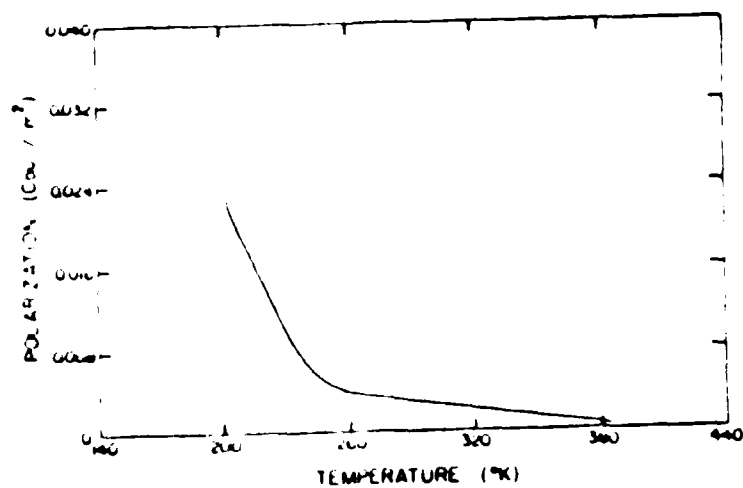


Figure 18. Polarization curve for Pt-112.

current of the TSC spectra and the polarization curves.

The third polarization curves did not show a return to a completely depoled state. From the polarization curves, it can be seen that a significant change in the rate of depolarization occurred near 290°K , 270°K and 245°K for PLZT-8, PLZT-10, and PLZT-12 respectively. The depolarization in both regions was linear with temperature.

The maximum in the polarization during the first polarization run was near the ferro/ paraferroelectric boundary for all compositions investigated. This maximum correlated with a decrease in the rate of depolarization in the third polarization curves. These data are plotted on the phase diagram in figure 3 as line PP, for Peak Polarization. The temperature of the peak polarization behavior in PLZT-8 is near the temperature for which Cross (1) has proposed a limit macrodomain stability.

The first polarization and second polarization runs support a model in which a poled material linearly dipoles over a large temperature interval into a paraelectric state. The temperatures taken to represent zero polarization are shown on the phase diagram in Figure 4 as line PO, for zero polarization. According to Cross (1), the temperature where the polarization is zero is the limit of microdomain stability with an applied field.

References

- 1) Y. Xi, C. Zhili, L. Cross, *Ferroelectrics*, **54**, 163 (1984).
- 2) Y. Xi, C. Zhili, L. Cross, *J. Appl. Phys.*, **54**, 3399 (1983).
- 3) A. Meitzler and H. O'Bryan, *Proc. of IEEE*, **61**, 959 (1973).
- 4) G. Schmidt, H. Arndt, G. Borchhardt, HJ. Bon Cieminski, T. Petzsche, K. Borman, A. Sternber, A. Zirnite, and V. Isupov, *Phys. Stat. Sol. (a)*, **63**, 501 (1981).
- 5) E. Keve and A. Annis, *Ferroelectrics*, **5**, 77 (1973).
- 6) G. Schmidt, G. Borchhardt, J. Von Cieminski, D. Grutzmann, E. Parinsch, and V. Isupov, *Ferroelectrics*, **42**, 3 (1982).
- 7) G. Schmidt, G. Borchhardt, J. Von Cieminski, D. Grutzmann, E. Parinsch and V. Isupov, *Ferroelectrics*, **42**, 3 (1982).
- 8) H. Arndt, G. Schmidt and N. Vogel, *Ferroelectrics*, **61**, 9 (1984).
- 9) A. Aning, T. Suzuki, M. Wuttig, *J. Appl. Phys.*, **53**, (10), 6797 (1982).
- 10) A. Aning and M. Wuttig, *J. Phys. Chem. Solids*, **45**, 481 (1984).
- 11) I. Hwang and M. Wuttig, To be published.

APPENDIX F

Polymeric Synthesis of Lead Magnesium Niobate Dielectrics

H.U. Anderson, M.J. Pennell and J.P. Guha

Polymeric Synthesis of Lead Magnesium Niobate Dielectrics

H. U. ANDERSON, M. J. PENNELL, and J. P. GUHA

Department of Ceramic Engineering, University
of Missouri-Rolla, Rolla, MO 65401

Abstract

This paper describes the polymeric synthesis of $\text{Pb}_3\text{MgNb}_2\text{O}_9$ based dielectric powders. The results show that single phase powders of about 50 nm crystallite size can be prepared at temperatures as low as 500°C. This preparation technique is based upon having the individual cations complexed in separate weak organic acid solutions. The individual solutions are gravimetrically analyzed for the respective cation concentration to a precision of 10-100 ppm. In this way it is possible to precisely control all of the cation concentrations, and to mix the ions on an atomic scale in the liquid state. There is no precipitation in the mixed solution as it is evaporated to the rigid polymeric states in the form of a uniformly colored transparent glass. This glass is calcined to yield powders which are both homogeneous and single phase with well controlled cation stoichiometry. The synthesis process is described and some resulting electrical, microstructural and crystallographic characteristics were obtained for sintered capacitors made with powders derived from this synthesis.

Introduction

The electrical and dielectric properties and the processing characteristics of perovskite (ABO_3) type oxides are closely related to the cation stoichiometry or A/B ratio. Therefore, for reliability and reproducibility, precise control of the cation content is of utmost importance. When one or both of the cations, A or B, are volatile under the conditions of either powder synthesis or subsequent sintering, control of cation stoichiometry becomes nearly impossible. This is particularly true for Pb containing perovskites. Most of these oxides need to be made and sintered at temperatures greater than 900°C . This temperature of 900°C is sufficiently high that substantial PbO loss occurs. At 900°C , $Pb_3MgNb_2O_9$ loses about 0.5 w%/hr or 2×10^{-5} moles PbO/hr. This is high enough that the lead content becomes rather ill defined and property reproducibility becomes a problem.

One method of minimizing PbO loss is to lower the processing temperature both for powder synthesis and device fabrication to below 900°C so that PbO loss through volatilization is minimized. This requires the starting perovskite oxide to be both homogeneous and fine crystallite-sized ($< 0.1 \mu\text{m}$). About the only methods available to obtain perovskite powders of such characteristics involve some form of organo-metallic synthesis. It is the intent of this paper to describe the preparation of $Pb_3MgNb_2O_9$ powders by one of these organo-metallic processes and to report some of the properties of the resulting dense polycrystalline capacitors.

Results and Discussion

Synthesis Process

The process described is one which was originally developed by Pechini [1] in the 1960's to prepare capacitor oxides such as titanates and niobates.

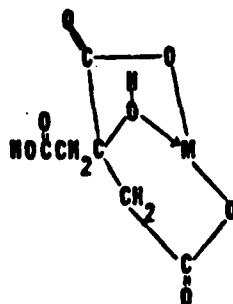
This process involves the ability of certain weak acids (alpha-pyroxycarboxylic acids) to form polybasic acid chelates with various cations from elements such as Ti, Zr, Cr, Mn, Ba, La, Pb, etc. These chelates can undergo polyesterification when heated in polyhydroxyl alcohol to form a polymeric glass which has the cations uniformly distributed throughout. Thus the glass retains homogeneity on the atomic scale and may be calcined at low temperatures to yield fine particulate oxides whose chemistry has been precisely controlled.

A typical flowsheet for the preparations from this process is shown in figure 1. The cationic sources which have been successfully used are carbonates, hydroxides, isopropoxides, and nitrates.

The general reaction sequence that occurs during the polymerization process is as follows. The metals chelate to the citrate and form a polybasic acid chelate. Addition of ethylene glycol to the mixture leads to the formation of an ester. Upon heating, polymerization takes place, thereby forming an organic matrix throughout the solution. Finally, the organics are removed by calcining the mixture at 400-500°C.

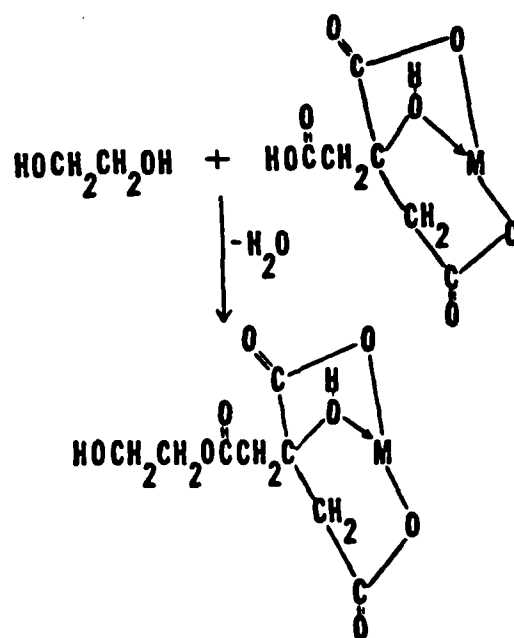
Certain hydroxycarboxylic acids, such as citric, lactic, tartaric, and glycolic acids, form polybasic acid chelates with metal ions. When compared to the majority of the acids, citric acid is more widely used in the processing of ceramic materials through the use of organic precursors. The typical citrate ion metal complexes tend to be fairly stable due to the

strong coordination of the citrate ion to a metal ion involving two carboxyl and one hydroxyl group as shown:



The desired metal ions are provided through various inorganic and organic constituents.

The presence of a polyhydroxy alcohol, such as ethylene glycol, allows for the formation of an organic ester with the acid chelate. A condensation reaction occurs with the formation of a water molecule. The hydroxyl group in the water formed arises from the carboxylic acid; the proton comes from the alcohol as shown in the following:



Upon heating, polyesterification occurs throughout the liquid medium, resulting in a homogeneous solution of metal ions attached to an organic matrix. The solution is gradually heated to remove excess solvent leaving a solid resin intermediate. The resin is then calcined to remove the organic material while the remaining inorganic metals are chemically combined to form the desired stoichiometrically controlled compound.

For the preparation of $\text{Pb}_3\text{MgNb}_2\text{O}_9$ the amounts of lead carbonate, magnesium carbonate and niobium ethoxide were calculated and then weighed out and mixed with a solution containing a ratio of 1 gm of anhydrous citric acid to 1.5 ml ethylene glycol.

The solution was heated to 90°C until the lead carbonate, magnesium carbonate and niobium ethoxide had gone into solution. This is the most important step of the process, as complete dissolution of the cations is necessary to insure homogeneity and composition. The resulting clear solution was evaporated until an amorphous, organic polymer formed. This solid was heated to 400°C to eliminate as much of the organics as possible. The solid turned into a black brittle mass which was then ground, screened, and transferred to a crucible, and calcined in the temperature range 500 to 800°C for 3 hours.

The relative weight loss and differential thermal analysis of the polymeric precursor are shown in figure 2. As can be seen, heat begins to evolve at about 400°C which corresponds to the region of maximum weight loss. Essentially all of the weight loss occurs at temperatures below 600°C. Above this temperature, no further exotherms were observed. This suggests that $\text{Pb}_3\text{MgNb}_2\text{O}_9$ can be synthesized at temperatures as low as 400 to 600°C.

In agreement with the DTA/TG results, figure 3 shows that the initially amorphous X-ray diffraction pattern changes to patterns which are typical of the crystalline perovskite and pyrochlore phases. However, from figure 4 it appears that lower calcination temperatures favor the pyrochlore phase. Also, it appears that it is difficult to obtain 100% perovskite $\text{Pb}_3\text{MgNb}_2\text{O}_9$, however, as has been reported by other investigators,²⁻⁴ the additions of excess MgO favor formation of the perovskite structure. Thus, it appears that 100% perovskite can be obtained at temperatures as low as 700 to 800°C if excess MgO is present.

The influence of calcination temperature on crystallite size is shown in figure 5. It is evident that powders with the average crystallite size of less than 500nm can be formed in the 500 to 800°C temperature range.

Properties of Resulting Oxides

Formulations of the composition $0.63 \text{ Pb}_3\text{MgNb}_2\text{O}_9 - 0.2 \text{ PbTiO}_3 - 0.17 \text{ MgO}$ were prepared to evaluate sintering and dielectric properties. The resulting powders were pressed into discs and placed into closed crucibles to minimize PbO loss and sintered in the temperature range 1000 to 1250°C. Best densification occurred in the 1200 to 1250°C temperature range. Table I lists some of the properties that have been obtained. The results are very preliminary and do not represent optimization. Typical microstructures of fractured surfaces are shown in figure 6.

These properties and microstructures are essentially the same as those obtained from formulations of mixed oxides. However, improvements of properties and reduction in sintering temperature are expected to occur as the processing and formulations become optimized. For example,

some recent results show that densification temperatures can be decreased to about 900°C without any appreciable loss of electrical and dielectrical properties by introducing excess PbO. Alterations of composition and processing parameters are the subject of our current studies.

Conclusion

It is evident that $\text{Pb}_3\text{MgNb}_2\text{O}_9$ can be synthesized by the polymeric precursor process of Pechini's. Results show that the perovskite phase can be obtained if excess MgO is present in the formulation at temperatures as low as 700°C. Densification of compositions that are either stoichiometric $\text{Pb}_3\text{MgNb}_2\text{O}_9$ or contain excess MgO cannot be sintered at temperatures below 1200°C. Compositions containing excess PbO can be sintered at about 900°C.

References

- 1) M. Pechini, U.S. Patent No. 3,330,697, July 11, 1967.
- 2) U. Furukawa, S. Fujiwara and T. Ogasawara, "Dielectric Properties of $\text{Pb}(\text{Mg}_{1/3}\text{Nb}_{2/3})\text{O}_3$ - PbTiO_3 Ceramics for Capacitor Materials", Proceedings of the Japan - U.S. Study Seminar on Dielectric and Piezoelectric Ceramics, P.T-4 (1982).
- 3) S.L. Swartz, T.R. Shrout, W.A. Schultze and L.E. Cross, "Dielectric Properties of Lead-Magnesium-Niobate Ceramics", Journal of the American Ceramic Society, 67(5) 311 - 315 (1984).
- 4) J.P. Guha and H.U. Anderson, "Preparation of Perovskite $\text{Pb}(\text{Mg}_{1/3}\text{Nb}_{2/3})\text{O}_3$ Using $\text{Pb}_3\text{Nb}_2\text{O}_8$ and MgO ", Communications of the American Ceramic Society (in press).

Acknowledgments

The authors would like to express their appreciation to the Office of Naval Research for the financial support.

Captions for Figures

Figure 1. Flowsheet for Preparation of Oxides

Figure 2. Differential Thermal Analysis (DTA) and Relative Weight Loss of Polymeric Precursor for $\text{Pb}_3\text{MgNb}_2\text{O}_9$ Preparation Which Had Been Heated to 150°C to Polymerize.

Figure 3. X-ray Diffraction Pattern of $\text{Pb}_3\text{MgNb}_2\text{O}_9 + 4\text{m}\%$ MgO Preparation:

A) Calcined 500°C , 3 hours

B) Calcined 700°C , 3 hours

C) Calcined 900°C , 3 hours

Figure 4. Percent Perovskite Formed in $\text{Pb}_3\text{MgNb}_2\text{O}_9$ and $\text{Pb}_3\text{MgNb}_2\text{O}_9 + 4\text{m}\%$ MgO Preparation as a Function of Calcination Temperature. (Time = 3 hours)

Figure 5. Scanning Electron Micrographs of $\text{Pb}_3\text{MgNb}_2\text{O}_9$ from Polymer Process

A) Calcined 500°C , 3 hours

B) Calcined 800°C , 3 hours

Figure 6. Scanning Electron Micrographs of $0.63 \text{ Pb}_3\text{MgNb}_2\text{O}_9 - 0.2 \text{ PbTiO}_3 - 0.17 \text{ MgO}$ Sintered at 1250°C .

A) Polished Surface

B) Fracture Surface

TABLE I

INITIAL RESULTS ON $\text{Pb}_3\text{MgNb}_2\text{O}_9$ SYNTHESIS

COMPOSITION

0.63 $\text{Pb}_3\text{MgNb}_2\text{O}_9$ - 0.2 PbTiO_3 - 0.17 MgO

SINTERING CONDITIONS

DISKS: 1200 - 1250°C 1-3 HOURS

DENSITY

7.4 - 7.6 g/cc (95 - 97% T.D.)

ELECTRICAL PROPERTIES

K_{MAX}: 15,000 - 20,000 (@ 32 - 35°C)

D_{F320}: 3 - 5%

R₃₂₀: 1 - 5 x 10¹² OHMS

RC₃₂₀: 10,000 - 15,000 OHM-FARAD

FIGURE 1

TYPICAL FLOW SHEET FOR PREPARATION OF OXIDES

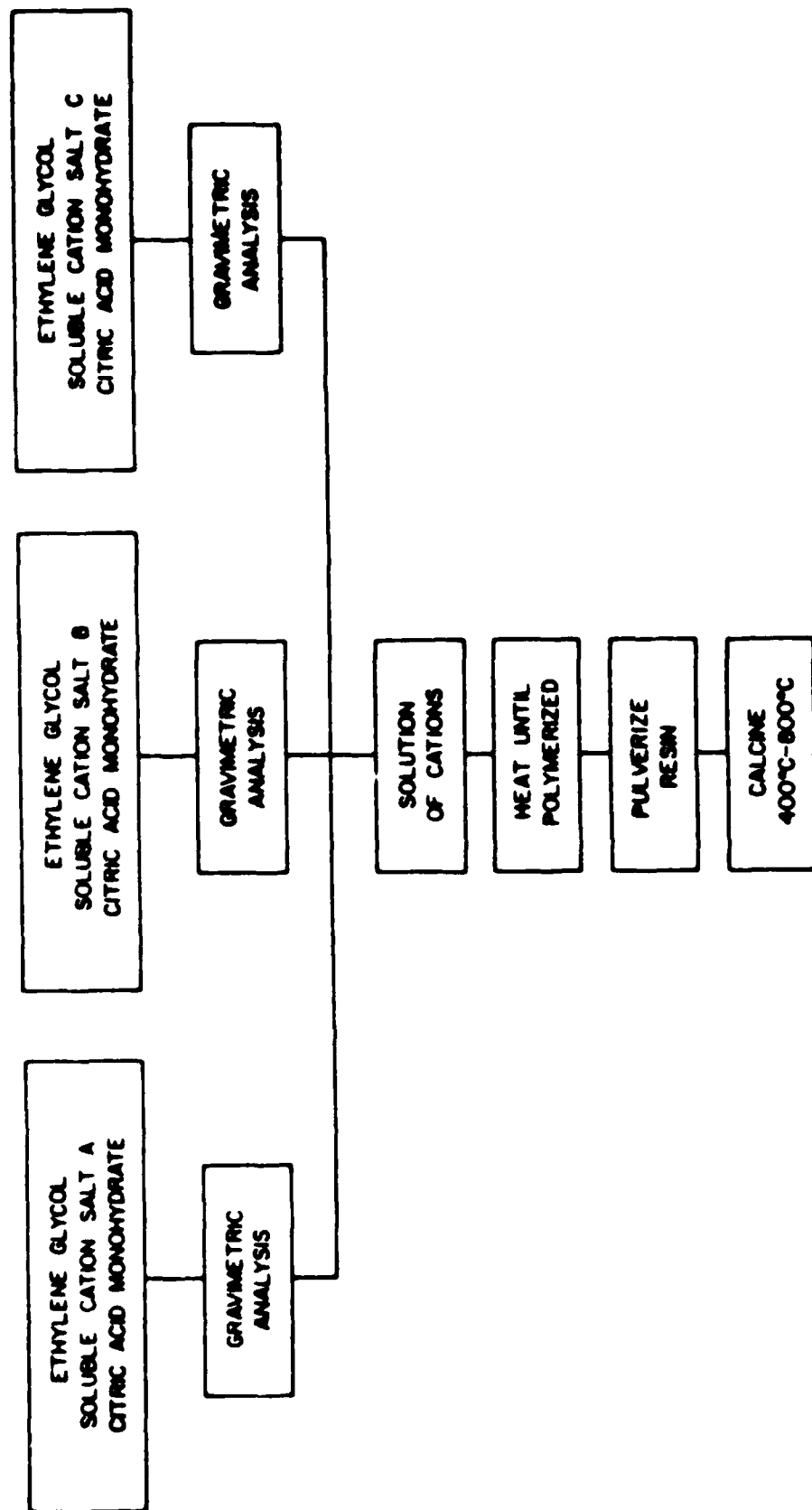


FIGURE 2

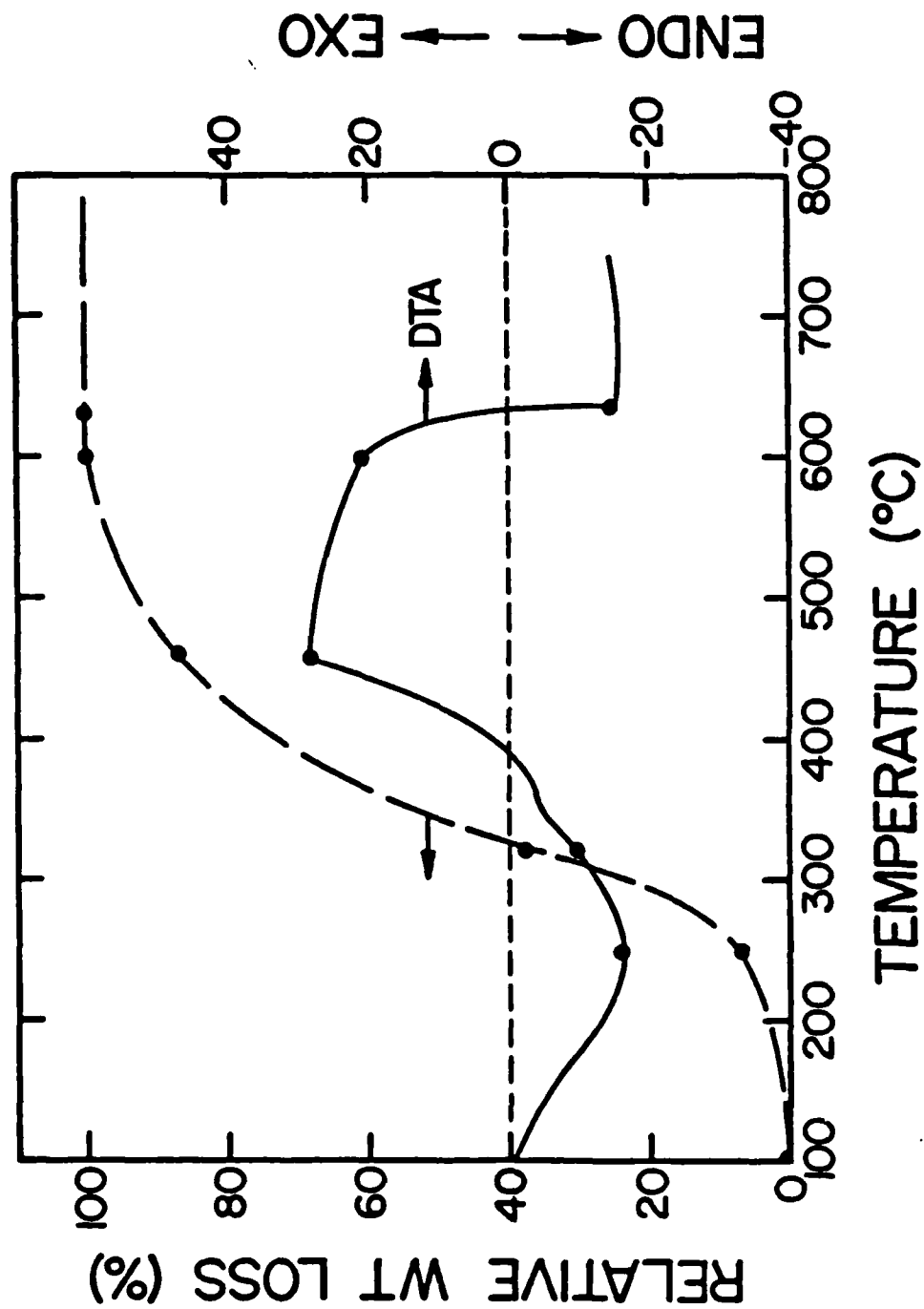


FIGURE 3

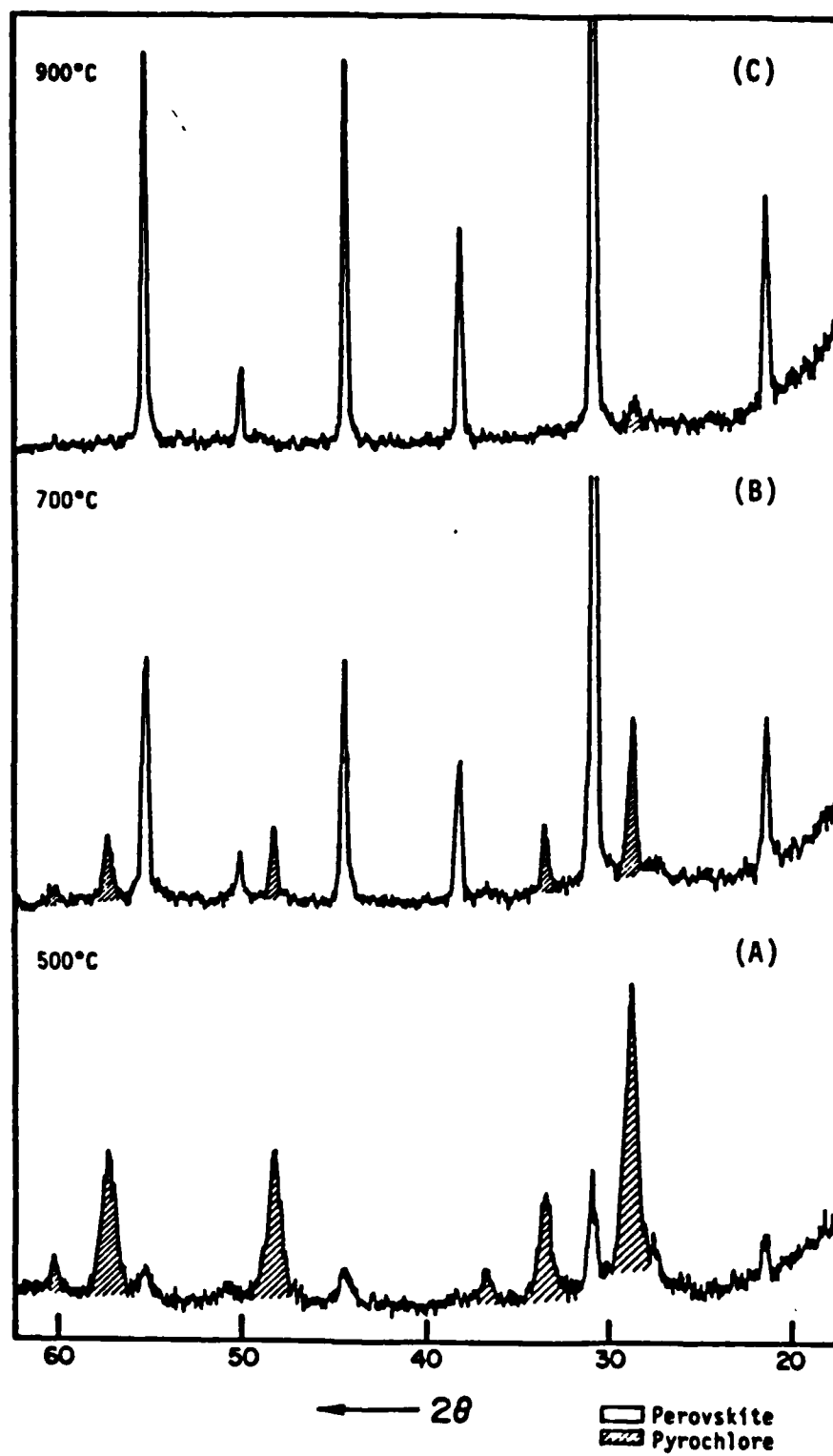


FIGURE 4

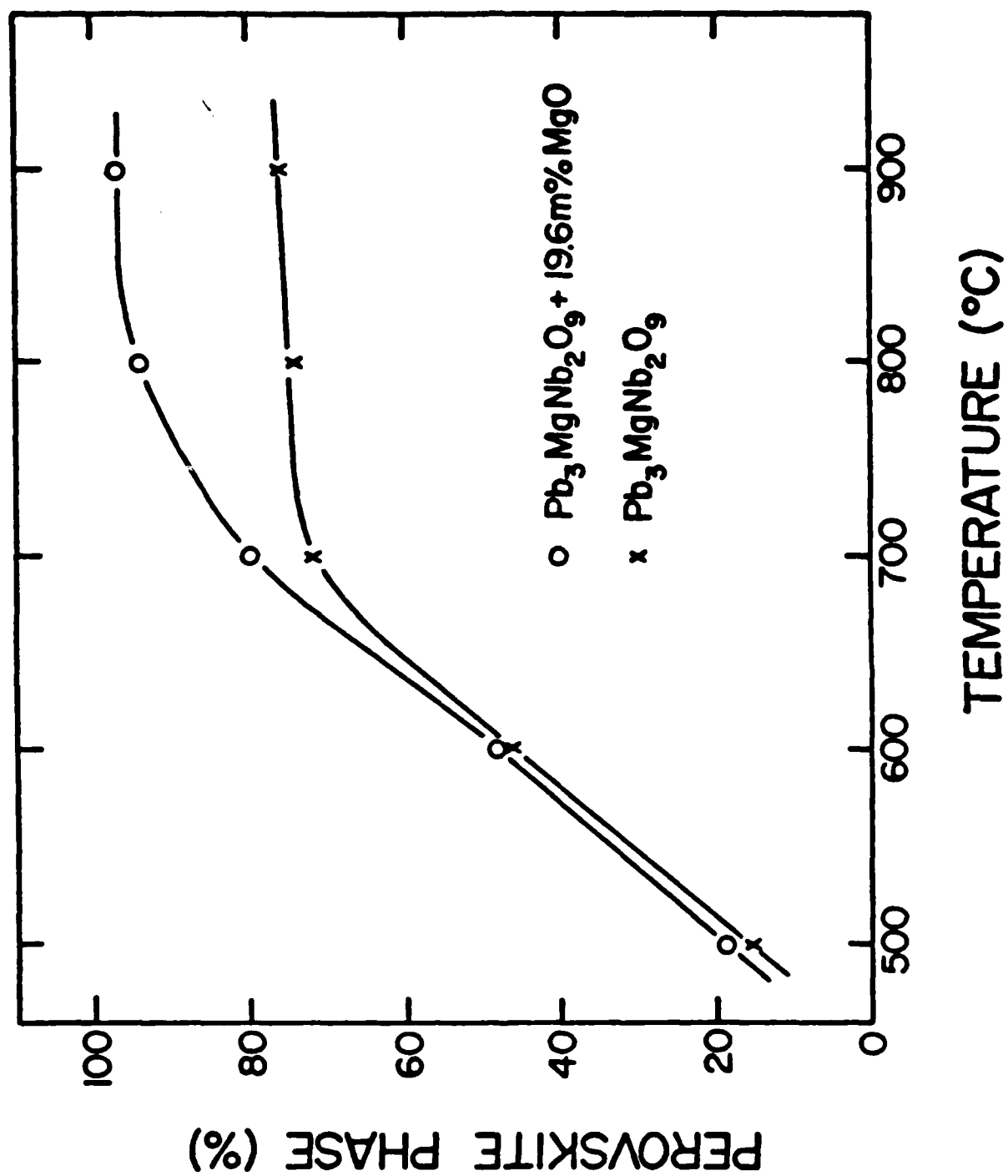


FIGURE 5

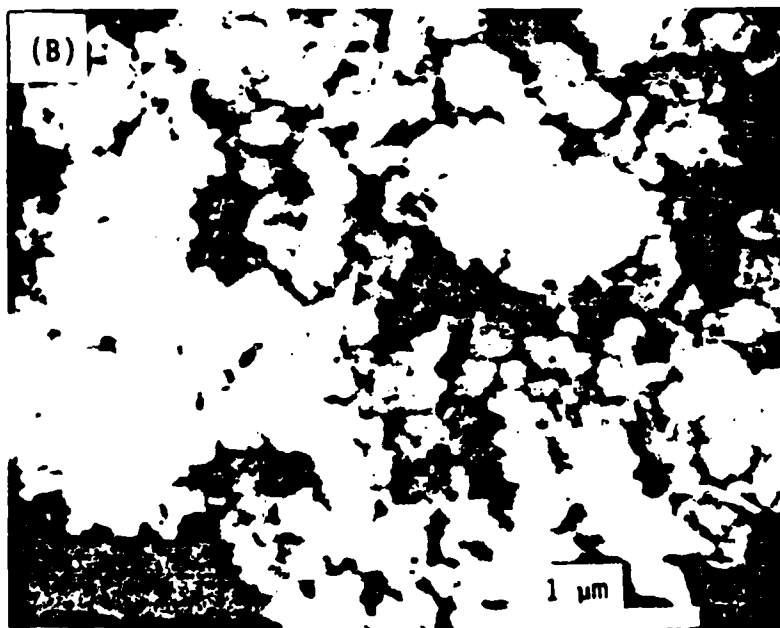
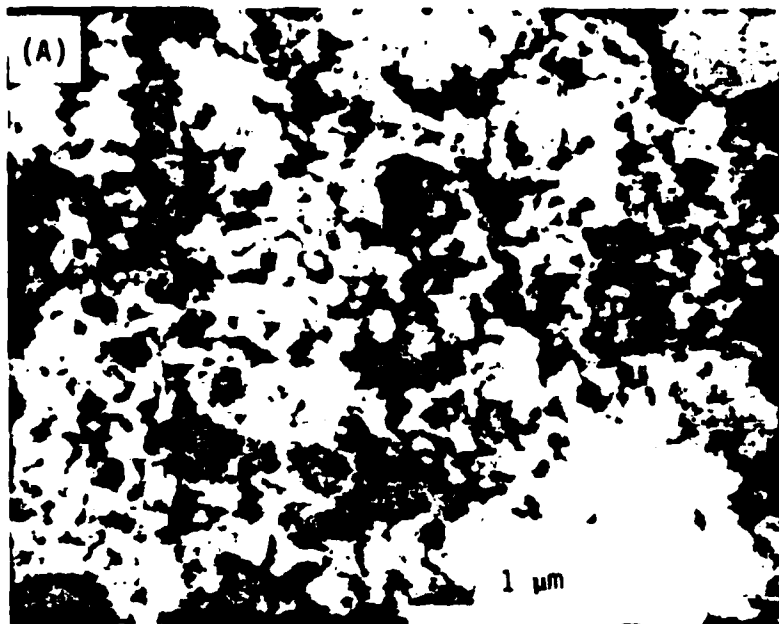
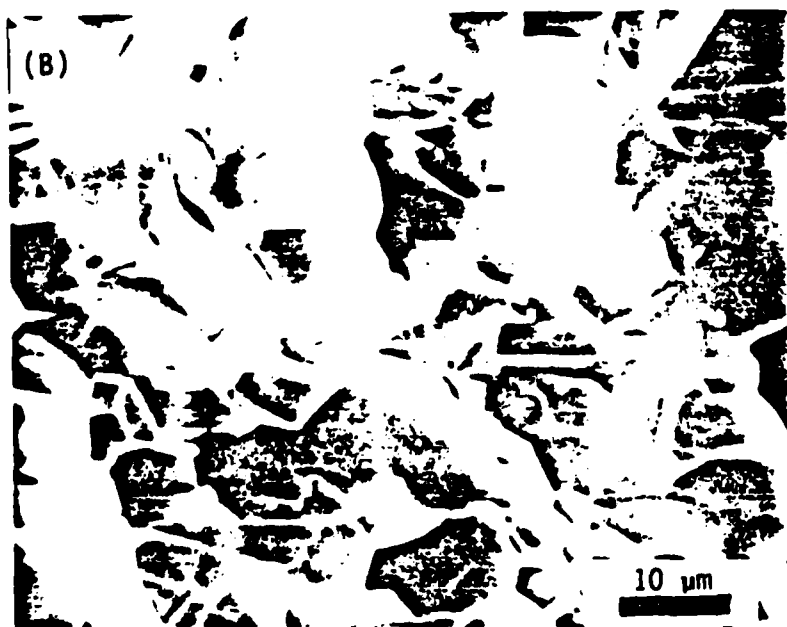
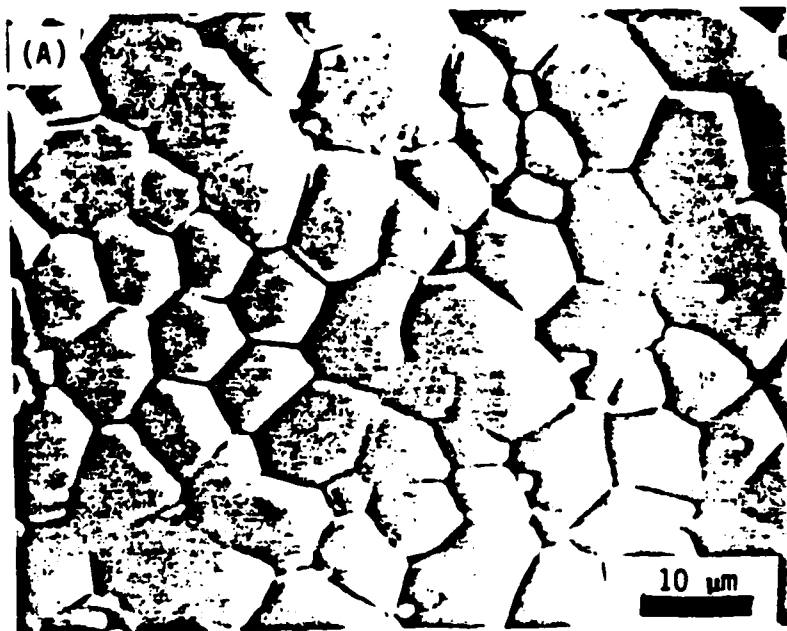


FIGURE 6



APPENDIX G

Reactions in the System $\text{PbO-MgO-Nb}_2\text{O}_5$

J.P. Guha

(iv) Reactions in the system $\text{PbO}-\text{MgO}-\text{Nb}_2\text{O}_5$

The reaction between PbO , MgO and Nb_2O_5 to form perovskite $\text{Pb}(\text{Mg}_{1-x}\text{Nb}_{2x})\text{O}_3$ were studied by the conventional solid state reaction techniques. Mixtures containing appropriate proportions of the oxides were pressed into pellets and fired at temperatures between 900°C and 1000°C for periods ranging from 2 to 5 h with intermittent cooling, crushing, pressing and firing until equilibrium was reached. The phases present in the equilibrated specimens were identified by x-ray powder diffraction using CuK_α radiation. The compositions studied, firing conditions and the phases present are given in Table I.

An x-ray diffraction pattern of a specimen which was subjected to repeated firing at 900°C for prolonged periods is shown in Fig. 1b. As evident from the XRD pattern, the major phase is the perovskite $\text{Pb}(\text{Mg}_{1-x}\text{Nb}_{2x})\text{O}_3$ which coexists with the pyrochlore phase and free PbO . It is apparent that the perovskite $\text{Pb}(\text{Mg}_{1-x}\text{Nb}_{2x})\text{O}_3$ is difficult to form at this temperature without the formation of a small amount of the pyrochlore phase. Further increase in the firing temperature resulted in an appreciable weight loss due mainly to the volatilization of PbO from the specimens which initiated a compositional change with a corresponding increase in the amount of the pyrochlore phase. However, a small amount of excess PbO (5 mol%) added to the initial mixture was found to enhance the reaction rate and greatly facilitate the formation of the perovskite phase, which is consistent with the previous findings.^{1,2} The x-ray diffraction pattern of a composition with an

excess PbO ~~exposed to similar firing conditions~~ is shown in Fig. 1B, which shows the increase in the amount of perovskite phase with a corresponding decrease in the pyrochlore phase.

The x-ray data obtained in this study are summarized below:

(1) Reactions between the precursor oxides at 800°C result in the formation of the perovskite $\text{Pb}(\text{Mg}_{1/3}\text{Nb}_{2/3})\text{O}_3$ with a small amount of pyrochlore phase. An increase in firing temperature increases the amount of the perovskite phase and decreases the amount of the pyrochlore phase. The pyrochlore phase can not be eliminated completely even on prolonged firing at elevated temperatures.

(2) The addition of excess MoO (5 mol%) enhances the formation of the perovskite phase by suppressing the formation of the pyrochlore phase.

(3) PbO, PbO and PbO_2 are compatible with $\text{Pb}(\text{Mg}_{1/3}\text{Nb}_{2/3})\text{O}_3$ and form perovskite phase in the ternary system $\text{PbO}-\text{MgO}-\text{Nb}_2\text{O}_5$.

(4) Nb_2O_5 is not compatible with $\text{Pb}(\text{Mg}_{1/3}\text{Nb}_{2/3})\text{O}_3$ and the reactions between these oxides result in the formation of the pyrochlore phase.

(5) Volatilization of PbO during firing, particularly, above the melting temperature of PbO (889°C) causes compositional variations and promotes the formation of the pyrochlore phase.

The formation of the ternary pyrochlore phase was examined by x-ray diffraction analysis of several mixtures containing variable amounts of PbO , MgO and Nb_2O_5 . The mixtures were pressed into pellets and equilibrated at temperatures between 800°C and 1000°C for periods ranging from 2 to 6 h. The compositions, firing temperatures and time, and the phases identified are given in Table II. The composition of the pyrochlore phase which has a cubic symmetry can be represented by the general formula $\text{Pb}_{2-2x}\text{Mg}_{1-x}\text{Nb}_{2+2y}\text{O}_{12}$ \checkmark ($0 < x < 0.3$ and $0.4 < y < 0.7$). X-ray diffraction data indicated that the pyrochlore phase is compatible with the perovskite $\text{Pb}(\text{Mg}_{1/3}\text{Nb}_{2/3})\text{O}_3$ and PbO .

Synthesis of $\text{Pb}(\text{Mg}_{1/3}\text{Nb}_{2/3})\text{O}_3$

The starting materials used were prefabricated $\text{Pb}_3\text{Nb}_2\text{O}_9$ and MgO . The lead niobate, $\text{Pb}_3\text{Nb}_2\text{O}_9$, was prepared by the solid state reactions between appropriate amounts of PbO and Nb_2O_5 at 820°C for 6 h with intermittent cooling, crushing, pressing and re-firing to yield a homogeneous end product. $\text{Pb}_3\text{Nb}_2\text{O}_9$ thus obtained was mixed with an equimolar proportion of MgO to give the composition $\text{Pb}(\text{Mg}_{1/3}\text{Nb}_{2/3})\text{O}_3$. The mixture was pressed into a pellet and then fired in two calcination steps at 900°C for a total period of 6 h. The calcined pellet was crushed into powder, pressed and re-fired to 900°C for 4 h to yield $\text{Pb}(\text{Mg}_{1/3}\text{Nb}_{2/3})\text{O}_3$. The x-ray powder diffraction pattern of the product indicated the presence of a small amount of pyrochlore phase. However, the pyrochlore phase was eliminated by the addition of a small amount of excess MgO of 60% to the starting mixture. It seems likely that a

minor addition of excess PbO is necessary to obtain pyrochlore-free $\text{Pb}(\text{Nb}_{1/2}\text{Nb}_{1/2}\text{O}_3)_2$.

The advantage of this process over the existing processes in which the starting materials used are either the precursor oxides or carbonates containing appropriate proportions of HfO_2 and PbO lies in the fact that no free PbO is involved in the synthesis and, therefore, the sintering temperature in excess of the melting point of PbO (889°C) can be avoided to enhance the formation of the compound. Furthermore, the loss due to the volatilization of PbO during firing is completely eliminated and, thus, any compositional variation resulting from the evaporation can be controlled effectively.

The present work is a study on the sintering characteristics, microstructure, development and dielectric properties of $\text{Pb}(\text{Nb}_{1/2}\text{Nb}_{1/2}\text{O}_3)_2$.

Some work has been done on perovskite type $\text{Pb}(\text{Nb}_{1/2}\text{Nb}_{1/2}\text{O}_3)_2$ - PbTiO_3 solid solutions, mainly for their dielectric properties and have been reported as ferroelectrics.¹⁻³ The solid solutions are readily formed at temperatures below 1000°C but require prolonged sintering at temperatures above 1500°C to obtain high densities. However, it has been reported⁴ that sintering of $\text{Pb}(\text{Nb}_{1/2}\text{Nb}_{1/2}\text{O}_3)_2$ based ceramics at elevated temperatures is not controlled by solid state diffusion in which the sintering mechanism of pores and conversion into dense ceramics are not different to each other. Furthermore, prolonged sintering at elevated temperatures may cause an appreciable PbO loss which causes a compositional variation and leads to an inhomogeneous microstructure.^{5,6}

addition of PbO to the sintering and firing mixtures of $\text{BaO} \cdot 2\text{SiO}_2 \cdot 2\text{SO}_3$ have been found to be attractive by earlier workers². Such additions expedite the formation of a homogeneous liquid phase and enhance the densification rate at higher sintering temperatures. In the present investigation, the effect of various levels of the sintering and firing additives and the properties of $\text{Pb} \cdot \text{BaO} \cdot 2\text{SiO}_2 \cdot 2\text{SO}_3$ (PBBS) based solid solutions was examined. The processing methods and the results obtained are summarized below.

1.1. Materials

The solid solution used in this study has a composition of $\text{Pb} \cdot \text{BaO} \cdot 2\text{SiO}_2 \cdot 2\text{SO}_3$. Various compositions of this system were used to yield several batches with variable PbO contents. Pastes containing the desired composition in various amounts of excess PbO were prepared by weighing, preheating of BaHCO₃ and PbCO₃ with appropriate proportions of SiO_2 . The powders were pressed into pellets and calcined in air at 950°C for 24 hr. The calcined pellets were reground and processed into 10 mm \times 10 mm \times 2 mm thick using a polyvinyl alcohol water solution as binder. The disks were placed on pre-sintered alumina SiO_2 free plates and fired in alumina crucible with a furnace atmosphere of reduced oxygen. The firing schedule at 1250°C for 24 hr and 1300°C for period ranging from 1 to 5 hr as a heating rate of 100°C/min and sintering composition was sintered at 1250°C for 24 hr, followed immediately by the end of the firing periods. The samples were cooled to room temperature and the plates present on

identified by powder x-ray diffraction (XRD) using $\text{CuK}\alpha$ radiation. The bulk densities of the sintered samples were determined by the liquid displacement method in m-cresol as the medium. The sintered samples were cooled and then reground to a fine powder after the sintering process. The sintered powder was heated and cooled at a rate of $10^\circ\text{C}/\text{min}$. The structures of the sintered samples were examined by scanning electron microscopy (SEM) equipped with an energy-dispersive X-ray analyzer (EDX) to determine the grain size and distribution. The grain size was measured as a function of temperature by dilatometry. The dilatometer bridge at 1, 10 and 100 Hz was used to monitor the position of the sample rods with an inductance coil which is at the free end of the rods.

Results

The XRD patterns of the sintered specimens revealed that the compositions were essentially $\text{La}_{0.9}\text{Sr}_{0.1}\text{FeO}_{3-\delta}$ and $\text{La}_{0.8}\text{Sr}_{0.2}\text{FeO}_{3-\delta}$ corresponding to the two samples. In addition, the $\text{La}_{0.9}\text{Sr}_{0.1}\text{FeO}_{3-\delta}$ sample showed additional phase obtained with higher sintering temperature. The phase of the additional phase was identified by XRD as La_2O_3 in the present work.

In order to observe the presence of the phase transition during the heating cycle, the corresponding pressure was applied during the cooling cycle appeared at a slightly lower temperature and pressure than the supercooling of the liquid. The phase transition appeared during both the heating and cooling cycles and the transition was reversible. Corresponding to the existence of the supercooling, the phase transition was observed at a lower temperature during the cooling cycle than during the heating cycle. The phase transition temperature during the heating cycle was about 1000°C for the $\text{La}_{0.9}\text{Sr}_{0.1}\text{FeO}_{3-\delta}$ sample and about 1050°C for the $\text{La}_{0.8}\text{Sr}_{0.2}\text{FeO}_{3-\delta}$ sample.

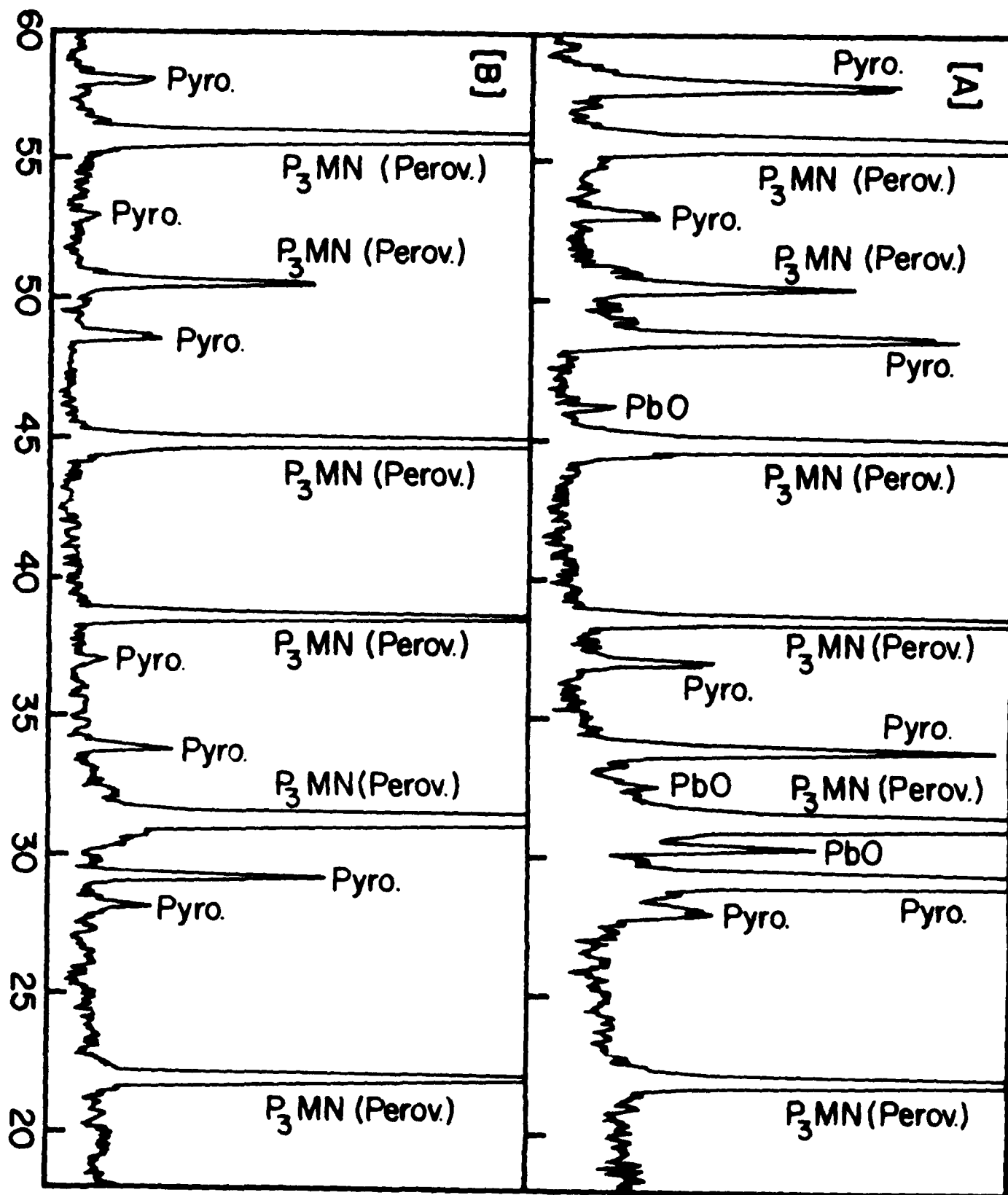
[illegible]

Table I: Compositions, firing conditions and phase identification for the perovskite phase in the system $\text{PbO-MgO-Nb}_2\text{O}_5$.

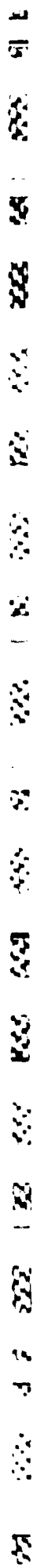
Compositions (mol%)			Tempr. (°C)	Time (Hr.)	Phases present
PbO	MgO	Nb_2O_5			
60.0	20.0	20.0	800	6	Perov. + Pyro.
			900	3	- do -
			950	3	- do -
			1000	2	Perov. + little Pyro.
65.0	15.0	20.0	800	6	Perov. + PbO (little)
			900	3	- do -
70.0	15.0	15.0	800	6	Perov. + PbO (little)
			900	3	- do -
68.0	22.0	10.0	800	6	Perov. + little Pyro.
			900	3	Perov. (single phase)
75.0	22.0	3.0	800	6	Perov. + MgO
			900	3	- do -
75.0	0.0	25.0	800	6	Perov. + Pyro (little)
			900	3	- do -
50.0	10.0	40.0	800	6	Perov. + Pyro.
			900	3	- do -

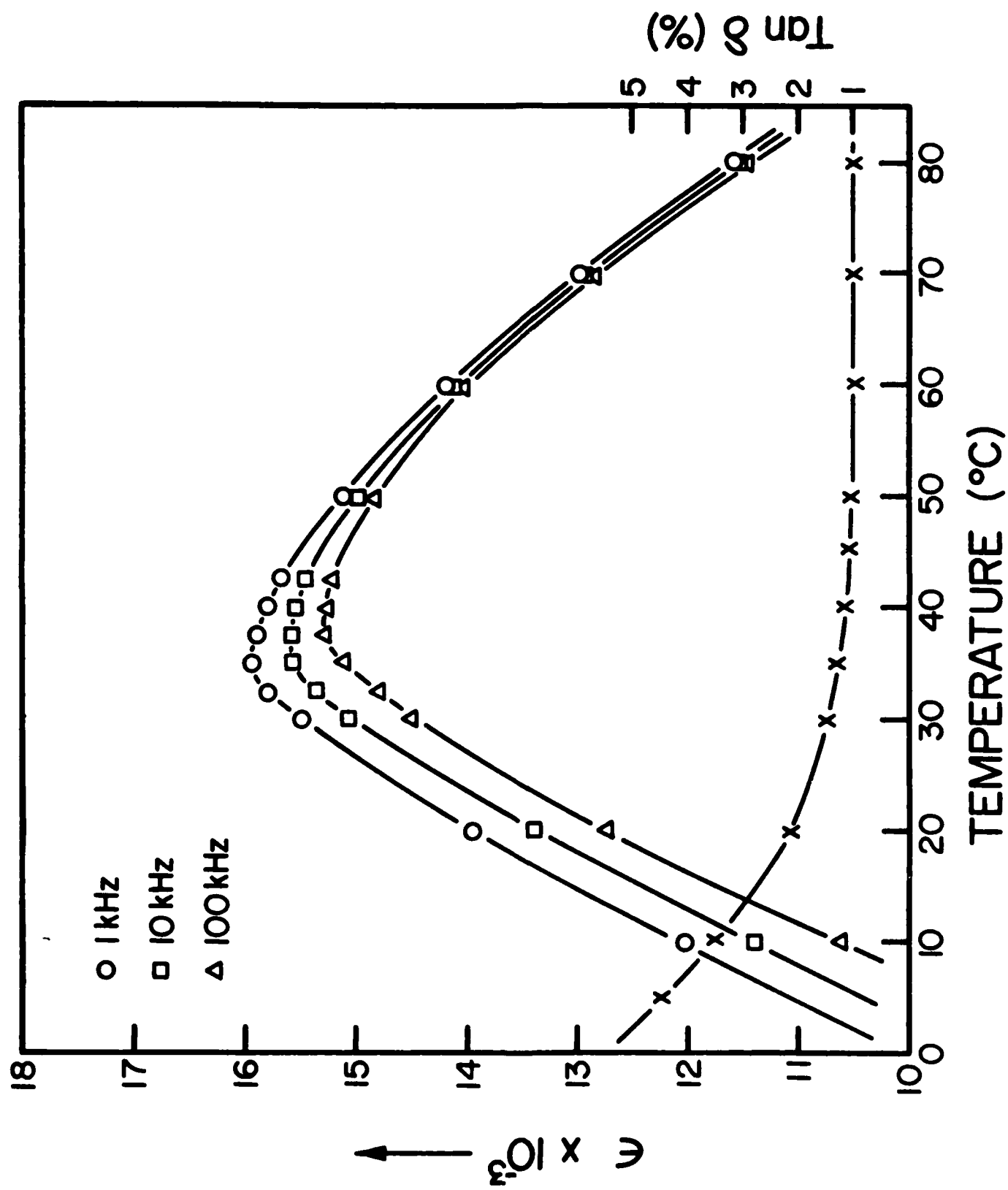
Table II: Compositions, firing conditions and phase identification for the pyrochlore phase in the system $\text{PbO}-\text{MgO}-\text{Nb}_2\text{O}_5$.

Compositions (mol%)			Tempr. (°C)	Time (hr.)	Phases present
PbO	MgO	Nb ₂ O ₅			
50.0	10.0	20.0	800	6	Pyro. (single phase)
			900	3	- do -
			1000	2	- do -
51.9	9.52	28.57	800	6	Pyro. (single phase)
			900	3	- do -
			1000	2	- do -
53.64	9.09	37.27	800	6	Pyro. (single phase)
			900	3	- do -
			1000	2	- do -
55.6	8.57	45.8	800	6	Pyro. + PbO (little)
			900	3	- do -
			1000	2	- do -
57.77	7.67	24.56	800	6	Pyro. + PbO (little)
			900	3	- do -
			1000	2	- do -
59.7	12.0	28.3	800	6	pyro. + Perov.
			900	3	- do -
61.8	13.0	25.2	800	6	pyro. + Perov.
			900	3	- do -









APPENDIX H

Preparation of Perovskite $\text{Pb}(\text{Mg}_{1/3}\text{Nb}_{2/3})\text{O}_3$
Using $\text{Pb}_3\text{Nb}_2\text{O}_8$ and MgO

J.P. Guha and H.U. Anderson

Reprinted from the Journal of the American Ceramic Society, Vol. 69, No. 11, November 1986
Copyright 1986 by The American Ceramic Society

Preparation of Perovskite $\text{Pb}(\text{Mg}_{1/3}\text{Nb}_{2/3})\text{O}_3$ Using $\text{Pb}_3\text{Nb}_2\text{O}_8$ and MgO

J. P. GUHA* AND H. U. ANDERSON*

Department of Ceramic Engineering, University of Missouri-Rolla, Rolla, Missouri 65401

The synthesis of perovskite $\text{Pb}(\text{Mg}_{1/3}\text{Nb}_{2/3})\text{O}_3$ from an equimolar mixture of $\text{Pb}_3\text{Nb}_2\text{O}_8$ and MgO was studied by solid-state reaction techniques. An addition of 1 wt% excess MgO to the stoichiometric composition enhances the formation of the cubic perovskite phase. The absence of free PbO in the initial starting materials minimizes the volatilization loss during firing, thereby reducing the possibility of any compositional change and resulting in a substantial improvement of the perovskite phase purity over the conventional mixed-oxide processing.

THE perovskite compound $\text{Pb}(\text{Mg}_{1/3}\text{Nb}_{2/3})\text{O}_3$ has recently received considerable attention in the area of electronic ceramics because of its excellent dielectric and ferroelectric properties.¹⁻⁴ Although the existence of $\text{Pb}(\text{Mg}_{1/3}\text{Nb}_{2/3})\text{O}_3$ and its stability at elevated temperatures have been established beyond doubt, the synthesis of the compound from the precursor oxides remains difficult. This is due mainly to the inevitable formation of an unwanted pyrochlore phase during the initial stages of

the reaction between the precursor oxides. The kinetics for the conversion of the pyrochlore phase to perovskite are very slow and necessitate repeated firing for prolonged periods at elevated temperatures. Since the presence of the pyrochlore phase even in small quantities in the final product is detrimental to the dielectric properties of $\text{Pb}(\text{Mg}_{1/3}\text{Nb}_{2/3})\text{O}_3$, its formation during the reaction process must be eliminated. Furukawa *et al.*⁵ were first to recognize the beneficial effect of excess MgO on the formation of the pyrochlore-free perovskite $\text{Pb}(\text{Mg}_{1/3}\text{Nb}_{2/3})\text{O}_3$ and observed a significant improvement of the dielectric properties of $\text{Pb}(\text{Mg}_{1/3}\text{Nb}_{2/3})\text{O}_3\text{-PbTiO}_3$ ceramics with the addition of ≈ 1 wt% excess MgO . Swartz *et al.*⁶ have proposed an alternative

method in which prefabricated MgNb_2O_6 and PbO were reacted at 800°C to form $\text{Pb}(\text{Mg}_{1/3}\text{Nb}_{2/3})\text{O}_3$. These workers have confirmed that the pyrochlore phase was eliminated by the addition of an excess MgO . The present communication is intended to show that the compound $\text{Pb}(\text{Mg}_{1/3}\text{Nb}_{2/3})\text{O}_3$ can be prepared by the solid-state reaction between $\text{Pb}_3\text{Nb}_2\text{O}_8$ and MgO at 900°C . Since there is no free PbO involved in this synthesis, the volatilization loss that occurs during the synthesis of the compound from the precursor oxides can be completely eliminated.

EXPERIMENTAL PROCEDURE

Lead niobate ($\text{Pb}_3\text{Nb}_2\text{O}_8$) used in this study was prepared by the solid-state reaction of appropriate proportions of high-purity reagent-grade PbO and Nb_2O_5 . Since $\text{Pb}_3\text{Nb}_2\text{O}_8$ and PbO form a eutectic at 830°C in the system $\text{PbO-Nb}_2\text{O}_5$,⁷ the reaction temperature for the preparation of $\text{Pb}_3\text{Nb}_2\text{O}_8$ used was 820°C . $\text{Pb}_3\text{Nb}_2\text{O}_8$ thus prepared was mixed with an equimolar amount of MgO , pressed into a pellet, and then fired in two calcination steps at 800°C for a combined period of 6 h with intermittent cooling, crushing, and mixing which were followed by a final heat treatment at 900°C for 4 h. Compositions containing an excess of MgO (1 to 2 wt%) were subjected to identical firing conditions. At the end of the firing period, the products were analyzed by X-ray powder diffraction (XRD) using Ni-filtered $\text{CuK}\alpha$ radiation and scanning electron microscopy (SEM) equipped with EDX attachments.

CONTRIBUTING EDITOR: G. LEWIS

Received May 19, 1986; revised copy received July 10, 1986; approved July 10, 1986

*Member, the American Ceramic Society

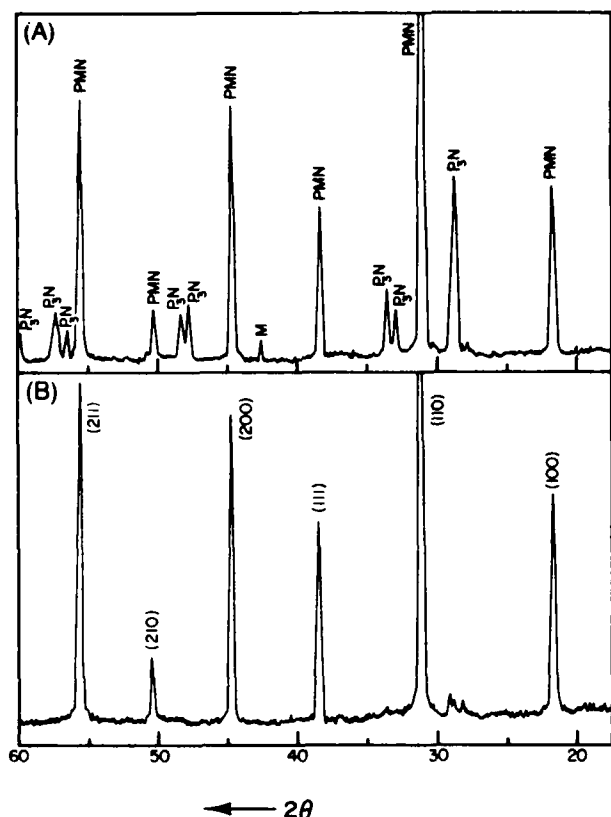
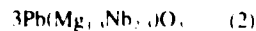
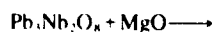
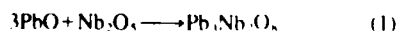


Fig. 1. X-ray powder diffraction pattern of an equimolar mixture of $\text{Pb(Nb}_2\text{O}_6)$ and MgO (A) calcined at 800°C for 6 h and (B) fired with 1 wt% excess MgO at 900°C for 4 h (PMN = cubic $\text{Pb(Mg}_{1/3}\text{Nb}_{2/3})\text{O}_3$, P.N. = $\text{Pb(Nb}_2\text{O}_6)$, and M = MgO).

RESULTS AND DISCUSSION

X-ray diffraction analyses performed on the fired mixtures indicated that, in the temperature range used, $\text{Pb(Nb}_2\text{O}_6)$ reacts with MgO to form the cubic perovskite $\text{Pb(Mg}_{1/3}\text{Nb}_{2/3})\text{O}_3$ phase.⁸ Figure 1(A) shows the XRD pattern of an equimolar mixture after repeated calcination at 800°C indicating the presence of mainly the cubic $\text{Pb(Mg}_{1/3}\text{Nb}_{2/3})\text{O}_3$ with some unreacted $\text{Pb(Nb}_2\text{O}_6)$ and MgO . As can be seen, the presence of the pyrochlore phase could not be detected accurately because of overlapping of the major reflections of this phase and $\text{Pb(Nb}_2\text{O}_6)$. As the temperature was increased to 900°C , the amount of the cubic perovskite phase increased with corresponding decrease in both $\text{Pb(Nb}_2\text{O}_6)$ and MgO . However, a complete conversion to the cubic $\text{Pb(Mg}_{1/3}\text{Nb}_{2/3})\text{O}_3$ was made with an addition of 1 wt% excess MgO to the stoichiometric mixture. Figure 1(B) shows the XRD pattern of a mixture containing excess MgO that had been subjected to identical heat-treatment conditions indicating the formation of the cubic $\text{Pb(Mg}_{1/3}\text{Nb}_{2/3})\text{O}_3$ with very little pyro-

chlore present. It is evident, therefore, that an addition of excess MgO enhances the reaction rate and allows the formation of the cubic perovskite phase. Thus, the overall reaction sequence observed by the XRD analysis can be represented by the following equations:



It can be seen from Eq. (2) that no free PbO is involved in the preparation of $\text{Pb(Mg}_{1/3}\text{Nb}_{2/3})\text{O}_3$ and hence a firing temperature in excess of the melting point of PbO (889°C) can be used in the synthesis of the compound. Likewise, the loss due to volatilization of PbO is completely eliminated in this process and, consequently, the composition of the compound can be effectively controlled during the firing process.

The scanning electron micrograph of a fracture surface of the compact obtained on



Fig. 2. Scanning electron micrograph of the fracture surface of $\text{Pb(Mg}_{1/3}\text{Nb}_{2/3})\text{O}_3$ sample fired at 900°C for 4 h (bar = $1\text{ }\mu\text{m}$).

firing at 900°C is shown in Fig. 2. As can be seen the morphology of the powder compact essentially reveals cubic grains with grain size varying within the range 0.5 to $2.0\text{ }\mu\text{m}$. The EDX analysis of the grains indicated the presence of lead, magnesium, and niobium in the sample.

The reaction sequence described herein provides yet another method of preparing $\text{Pb(Mg}_{1/3}\text{Nb}_{2/3})\text{O}_3$ and appears to be a substantial improvement over the conventional mixed-oxide process. The ease with which the pyrochlore-free perovskite $\text{Pb(Mg}_{1/3}\text{Nb}_{2/3})\text{O}_3$ phase is formed largely depends on the amount of excess MgO added to the starting stoichiometric mixture and also on the firing temperature used for the synthesis of the compound.

REFERENCES

- G. I. Smolenskii and A. I. Agranovskaya, "Dielectric Polarization of a Number of Complex Compounds," *Sov. Phys. Solid State (Engl. Transl.)*, **1** [10] 1429-37 (1960).
- V. A. Bokov and I. E. Myl'nikova, "Electrical and Optical Properties of Single Crystals of Ferroelectrics with a Diffused Phase Transition," *Sov. Phys. Solid State (Engl. Transl.)*, **3** [3] 613-23 (1961).
- M. Lejeune and J. P. Boilot, "Formation Mechanism and Ceramic Process of the Ferroelectric Perovskite $\text{Pb(Mg}_{1/3}\text{Nb}_{2/3})\text{O}_3$ and $\text{Pb(Fe}_{1/3}\text{Nb}_{2/3})\text{O}_3$," *Ceram. Int.*, **8** [3] 99-104 (1982).
- S. L. Swartz and T. R. Shrout, "Fabrication of Perovskite Lead-Magnesium-Niobate," *Mater. Res. Bull.*, **17**, 1245-50 (1982).
- K. Furukawa, S. Fujiwara, and T. Ogasawara, "Dielectric Properties of $\text{Pb(Mg}_{1/3}\text{Nb}_{2/3})\text{O}_3$ - PbTiO_3 Ceramics for Capacitor Materials," p. 74 in Proceedings of the Japan-US Study Seminar on Dielectric and Piezoelectric Ceramics, 1982.
- S. L. Swartz, T. R. Shrout, W. A. Schultze, and I. E. Cross, "Dielectric Properties of Lead-Magnesium-Niobate Ceramics," *J. Am. Ceram. Soc.*, **67** [5] 311-15 (1984).
- R. S. Roth, "Phase Equilibrium Relations in the Binary System Lead Oxide-Niobium Pentoxide," *J. Res. Natl. Bur. Stand. (U.S.)*, **62** [1] 27-38 (1959).
- JSPCD Card No. 27-1199.

APPENDIX I

Microstructural Inhomogeneity in Sintered $\text{Pb}(\text{Mg}_{1/3}\text{Nb}_{2/3})\text{O}_3\text{-PbTiO}_3$ Based Dielectrics

J.P. Guha and H.U. Anderson

BEACON GRAPHICS CORP.
MASTER PROOF

DEC 30 1986

J. Am. Ceram. Soc., 70 [0] C-000-C-000 (1987)

Microstructural Inhomogeneity in Sintered $\text{Pb}(\text{Mg}_{1/3}\text{Nb}_{2/3})\text{O}_3$ - PbTiO_3 Based Dielectrics

J. P. GUHA* AND H. U. ANDERSON*

Department of Ceramics Engineering, University of Missouri-Rolla, Rolla, Missouri 65401

The sintering behavior and microstructural development of dielectric ceramics based on $\text{Pb}(\text{Mg}_{1/3}\text{Nb}_{2/3})\text{O}_3$ - PbTiO_3 solid solutions are greatly affected by the formation of a liquid phase at $\approx 1290^\circ\text{C}$. Prolonged sintering at and above this temperature gives rise to an excessive PbO loss and the resultant variation in composition leads to an inhomogeneous microstructure. The inhomogeneity is characterized by the formation of a dense, localized region containing a PbO -rich liquid near the surface with a porous interior region in the bulk of the sample.

THE sintering characteristics and dielectric properties of ceramics based on the solid solutions of $\text{Pb}(\text{Mg}_{1/3}\text{Nb}_{2/3})\text{O}_3$ - PbTiO_3 have been reported by several workers.^{1,2} In these studies, it has been shown that the presence of excess MgO in the stoichiometric composition and increased sintering temperatures resulted in an increase in grain size with a corresponding increase in dielectric constant of the ceramics. It has been further reported³ that prolonged sintering at 1300°C leads to a compositional variation that affects the dielectric properties.

Although the dielectric properties of the solid solutions have been reported extensively in the literature, very little is known about the sintering characteristics and microstructural development at elevated temperatures. The present communication is intended to show that prolonged sintering of $\text{Pb}(\text{Mg}_{1/3}\text{Nb}_{2/3})\text{O}_3$ - PbTiO_3 solid solutions gives rise to excessive PbO loss, causing a change in the composition. The resultant inhomogeneity of microstructure and the sintering conditions under which such inhomogeneity occurs are discussed.

EXPERIMENTAL PROCEDURE

Solid solutions of the general composition $\text{Pb}(\text{Mg}_{1-x}\text{Nb}_{2x})_{1-x}\text{Ti}_x\text{O}_3$ (where $x=0.09$ to 0.04) were prepared from appropriate amounts of prefabricated MgNb_2O_6 and reagent-grade PbO and TiO_2 powders. An excess of MgO (5 mol%) was added to all compositions to facilitate the formation of a pyrochlore-free perovskite phase. The mixtures were pressed into pellets and calcined in air for 3 h. The calcined pellets were crushed to powder, mixed with a 4% poly(vinyl alcohol) water solution, and pressed into disks 14 mm diameter and 2 mm thick. The disks were supported on presintered $\text{Pb}(\text{Mg}_{1-x}\text{Nb}_{2x})\text{O}_3$ setters and stacked inside a covered alumina crucible to minimize PbO loss during sintering. The disks were then sintered in air at temperatures between 1250° and 1300°C for periods ranging from 2 to 10 h at a heating rate of $300^\circ\text{C}/\text{h}$. At the end of the firing period, the crucible was cooled inside the furnace and the phases present in the samples were identified by powder X-ray diffraction (XRD) using $\text{CuK}\alpha$ radiation. The weight losses at various sintering temperatures were ascertained by the change in weight of the samples before and after the firing. The fracture surfaces were examined by scanning electron microscopy (SEM), and elemental analysis of the phases present in the sintered samples was conducted by an X-ray energy dispersive spectrometer (EDS) attached to the SEM.

RESULTS AND DISCUSSION

The XRD analysis of the sintered samples revealed a single-phase cubic perovskite pattern that essentially corresponded to the $\text{Pb}(\text{Mg}_{1-x}\text{Nb}_{2x})\text{O}_3$ - PbTiO_3 solid solution. It was observed that increasing additions of PbTiO_3 in the solid solutions did not cause any appreciable shift in the characteristic reflections of the perovskite pattern. This result was probably due to the similarity of the radii of Nb^{5+} (0.69) and Ti^{4+} (0.68) ions.

CR 57 _____

poly(vinyl

alcohol)- C

mm in

The sintering characteristics of various compositions indicated similar trends in density variations and weight losses at different firing temperatures irrespective of the PbTiO_3 content in the solid solutions. In general, the densities increased with increasing sintering temperature. However, a rapid increase of density values was observed for the sintered samples at 1290°C followed by a small decrease at 1300°C for the same sintering time. A maximum density of 96% of the theoretical was achieved by sintering at 1290°C for 3 h. Further increase in the sintering time at this temperature did not show any significant increase in the density values. The corresponding weight loss data indicated that the rate of loss was considerably higher at temperatures at and above 1290°C . Most of the losses occurring at this temperature appeared to take place during the initial period of the sintering; thereafter, the rate became linear with time.

The sequence of microstructural changes observed during the sintering of the solid-solution compositions clearly demonstrated that a liquid phase was formed at $\sim 1290^\circ\text{C}$. With increasing sintering time and temperature, the rapid increase in the densification rate appeared to be consistent with sintering in the presence of a liquid phase. The microstructures of the sintered samples showed a significant increase in the grain size with a corresponding decrease in porosity. However, the slight decrease in density at 1300°C can be accounted for by the loss of PbO from the samples as observed by the weight-loss experiments. Seemingly, the PbO loss, which increases rapidly at the onset of the liquid formation at 1290°C , appeared to have caused some variations in the composition and led to an inhomogeneous microstructure. This behavior was evident from the morphology of the fracture surfaces which revealed the presence of a highly dense localized region near the surface with a porous yet rigid interior forming the bulk of the sample. The SEM micrograph of the localized region showing the distribution of various phases is exhibited in Fig. 1(A). This distribution is typical of the microstructures resulting from prolonged sintering at elevated temperatures which revealed the presence of many rectangular solid particles evenly distributed in a liquid matrix. The EDS analysis indicated that the solid phase contained Mg^{2+} and Nb^{5+} with very little Ti^{4+} , and no Pb^{2+} was present. The surrounding liquid layer, the morphology of which is shown in Fig. 1(B), was found to be mostly homogeneous and contained, predominantly, Pb^{2+} . By contrast, the less-dense interior region, as shown in Fig. 2, was found to be essentially unchanged and consisted of coarsened grains of the solid solution with some residual porosity evenly distributed in the bulk.

The concentration of a PbO -rich liquid phase near the surface during sintering is believed to be the result of the simultaneous volatilization of PbO from the surface and liquid migration within the samples. As is evident from this study, a significant weight loss occurs mainly because of the volatilization of PbO at the liquid formation temperature (1290°C). Seemingly, prolonged sintering at and above this temperature gives rise to extensive PbO loss from the surface and leads to a compositional variation. With the progressive loss of PbO from the surface, the PbO content of the liquid phase must have decreased to a sufficient extent to allow the formation of MgNb_2O_6 solid particles in the PbO -rich liquid matrix. It seems likely that liquid migration within the bulk of the sample during sintering is a necessary condition for allowing the change in the composition near the surface, leaving a rigid yet porous structure in the interior. It is apparent that further study is required to understand the nature of the liquid phase and its behavior inside the samples throughout the sintering process.

REFERENCES

- (1) K. Furukawa, S. Furumura, and T. Ogasawara, Dielectric Properties of $(\text{PbMg}_{1-x}\text{Nb}_x)_2(\text{PO}_4)_2$ Ceramics for Capacitor Materials, p. 74 in Proceedings of the Japan-US Study Seminar on Dielectric and Piezoelectric Ceramics (1986).
- (2) S. L. Swartz, J. R. Stinson, W. A. Schulte, and J. E. Uhlir, Dielectric Properties of Lead Magnesium Niobate Ceramics, *J. Am. Ceram. Soc.*, **67**(5), 111-15 (1984).
- (3) J. P. Guthrie, Dielectric Properties of Lead Magnesium Niobate Ceramics, *J. Am. Ceram. Soc.*, **68**(3), C-86-C-87 (1985).

Author: Please give publisher and city of publication.

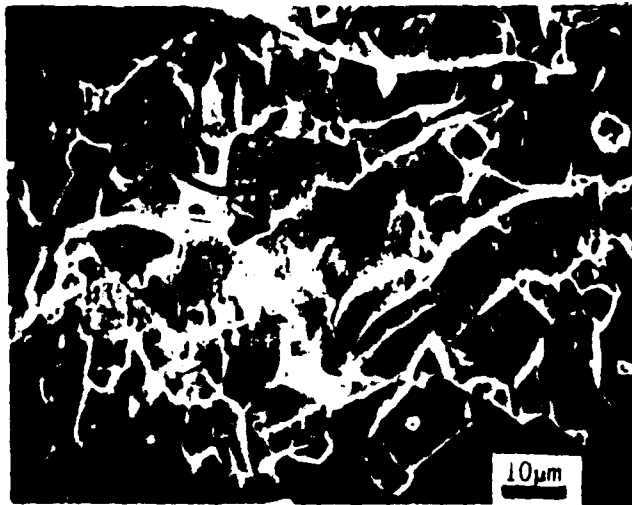
Fig. 1. SEM showing inhomogeneity in composition (0.92 $\text{PbMg}_{0.08}\text{Nb}_2\text{O}_{10}$), after sintering at 1290°C for 8 h: (A) distribution of MgNb_2O_6 in a liquid matrix and (B) morphology of the PbO rich liquid phase.

Fig. 2. SEM of the fracture surface showing large and coarsened grains of the solid solution with residual porosity at the interior of the sintered sample.

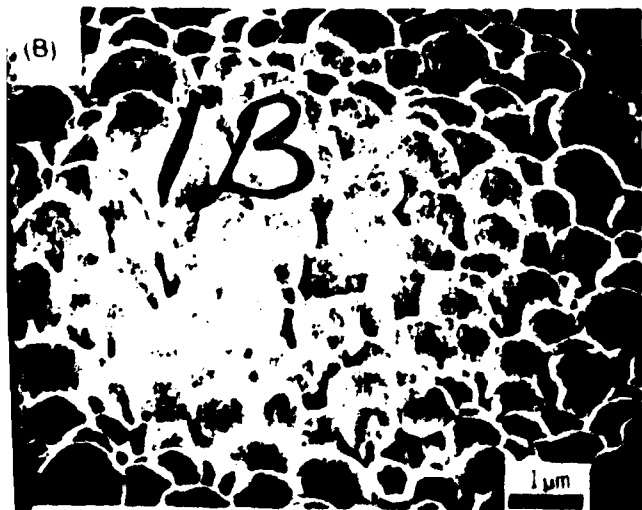
Copyright © 1986 by J. M. Smith

Received August 22, 1986; revised and accepted
September 12, 1986; approved September 26, 1986.
Member, the American Ceramic Society.

(A)



(B)



APPENDIX J

Effects of Additions on the Physical and Dielectric
Properties of Lead Magnesium Niobate

D. Beck, M.S. Thesis, 1986

The effect of additives on ferroelectric lead magnesium niobate based disc capacitors was studied. The basic capacitor composition was 55.4 m% $\text{Pb}_3\text{MgNb}_2\text{O}_9$, 15.5 m% PbTiO_3 , and 29.1 m% MgO . The additives used were $\text{PbBi}_2\text{Nb}_2\text{O}_9$, Pb_2MgWO_6 , and PbO in concentrations of 0.5, 1.0, and 2.0 m%. The compositions were formed by solid state reaction and the capacitors sintered at 1225, 1250, and 1260°C.

The effect of composition on the capacitor properties was determined by measurement of density, porosity, weight loss during sintering, dielectric constant, dissipation factor and room temperature resistivities. Microstructure was examined by x-ray diffraction and scanning electron microscopy.

The additives either lowered the density of the capacitors or left it unaffected. Porosity was unaffected by $\text{PbBi}_2\text{Nb}_2\text{O}_9$ and Pb_2MgWO_6 additions but it was increased by PbO addition. Weight loss during firing was also higher with the addition of PbO . The dielectric constant was either lowered or unaffected by the addition, but the dissipation factor was generally lowered at temperatures above the phase transition. The electrical resistivities were generally greater than 10^{11} ohm-cm. According to x-ray diffraction and microstructure, the additives were found not to form second phases.

APPENDIX K

The Effect of Excess Lead Oxide on the Sintering Characteristics and Dielectric Properties of Lead Magnesium Niobate Ceramics

D. Hong, M.S. Thesis, 1987

In this investigation the effect of lead oxide additions on sintering characteristics and dielectric properties of ferroelectric $\text{Pb}_3\text{MgNb}_2\text{O}_9$ based capacitors was studied. The basic dielectric compositions were formed by solid state reaction. Densification was studied as a function of PbO content over the temperature range 900°C to 1000°C for sintering times one to six hours depending on the amount of additive and sintering temperature.

The weight loss, density and shrinkage measurements of each composition were made in order to relate the effects of the excess PbO additions on the densification. The dielectric and electrical properties were then correlated to the microstructure and density.

The compositions sintered at low temperatures were densified by the formation of liquid phase during sintering, however, an increase of the amount of liquid phase does not necessarily yield optimum dielectric properties. A proper control of the sintering temperature, time and the amount of excess PbO is required for optimization of the dielectric properties.

The results show:

1) The reaction between MgNb_2O_6 and PbO at 750°C yielded nearly pure P_3MN phase.

2) The addition of excess PbO to P_3MN - PT based composition resulted in densities greater than 96 % of theoretical density at temperatures as low as 900°C .

3) The densities of the specimens with excess PbO sintered in the 900 to 1000°C temperature range depends upon the loss of PbO . Excessive PbO losses deteriorate the densification at 1000°C for sintering times greater than 1 hour.

4) The solid solution P_3MN - PT with 3.3 m% excess PbO which was sintered at 1000°C for 1 hour yielded capacitors with maximum dielectric constant of 17,000 at 1 Khz.

END

5-87

DTic